INVESTIGATION OF PLANAR TERAHERTZ PASSIVE DEVICES AND COUPLING METHODS FOR ON-WAFER APPLICATIONS

By

Joshua Carl Myers

A DISSERTATION

Submitted to
Michigan State University
in partial fulfillment of the requirements
for the degree of

Electrical Engineering – Doctor of Philosophy

2015

ABSTRACT

INVESTIGATION OF PLANAR TERAHERTZ PASSIVE DEVICES AND COUPLING METHODS FOR ON-WAFER APPLICATIONS

By

Joshua Carl Myers

In recent years, developments have pushed the cut-off frequencies of transistors near 1 THz, enabling for the first time the design of large bandwidth transmit/receive modules. While there has been a significant interest in the research community to implement these devices, many challenges have slowed such progress. Primarily, these challenges stem from the high dielectric and metal losses many materials display in the THz spectrum. However, to implement wafer-level integrated circuits in the THz spectrum, efficient passive devices that are integration compatible must be developed. For any integrated system, many of the most important passive building blocks of the system are reduced to efficient waveguiding, filtering, and coupling between any active components, necessary measurement systems, and input sources. In this dissertation, efficient passive terahertz components, including waveguides, filters, and input couplers, are developed.

First, a method of efficiently coupling THz radiation between commercial quasi-optical THz systems and integration compatible THz components is introduced. The primary method developed is the use of high-density polyethylene focusing probes which can be easily fabricated so that they are compatible with commercial THz systems. The efficiency of the probes are then investigated when used with a simple silicon-based dielectric waveguide.

Next, dielectric ridge waveguides made of silicon are investigated for low loss THz wave propagation. A theoretical effective index method is applied to determine the modal propagation properties of the waveguides as well as the attenuation of the structures. FEM simulation is also carried out to verify these results. Various ridge waveguides made on silicon wafers are investigated through measurement and determined to provide low-loss waveguiding properties in the THz spectrum. The focus is then shifted to the design of

thin-film integration compatible THz filters. These filters are designed with multi-objective evolutionary algorithms coupled with FEM modeling. Bandwidth, stopband characteristics, multi-resonance, and other properties of the filters are developed and improved through optimization. The filters are measured using a commercial THz system, and shown to match well with the optimized expectations.

Finally, another waveguiding structure is introduced which is built with thin-metal periodic structures on thin-film substrates. These structures efficiently guide THz waves along the surface of the textured metal structures. With these structures, other passive THz circuits, such as power splitters and sensors, are also developed. The waveguiding structures, as well as power splitter, are measured in conjunction with the dielectric focusing probes developed previously, and show to provide high transmission properties at specific design frequencies.

Throughout this dissertation efficient waveguides, filters, and coupling methods are introduced. These methods are compatible with current semiconductor fabrication techniques, enabling device realization directly on-wafer. In addition, all of the passive devices that are developed are simple to fabricate, as well as low-cost. Through the work presented in this dissertation, the realization of passive building blocks for on-wafer active THz circuits are developed, which in turn provides the possible realization of active on-wafer THz circuits.

ACKNOWLEDGMENTS

I would like to first thank my advisor Dr. Premjeet Chahal. Since first meeting him in ECE 405 as an undergraduate, I have learned more than I thought possible about electromagnetics. Although at times he may be a taskmaster, his creative and unique visions have inspired me with numerous research ideas that neither I nor anyone else could have envisioned. Without his research guidance and assistance I can truly say that I do not know what I would be doing with my life. In addition to all of this, I would like to thank him greatly for giving me the opportunity to complete my graduate degree and welcome me into the Electromagnetics Research Group at Michigan State University.

Second, I would like to thank Dr. Edward Rothwell for all of the meaningful and insightful conversations we have had not only about this research, but also about many other areas in electromagnetics and life. While his sarcasm is sometimes thick, I have had nothing but positive experiences working with him. Although he is not my advisor, he has treated me with the same respect and helpfulness that he typically reserves only for his students. I would also like to thank Dr. Nelson Sepulveda, not only for his excellent softball playing, but also his assistance in my research and for serving on my committee. In addition, I would like to also thank Dr. Alejandro Diaz for taking the time from his busy schedule to be on my committee, as well as sit through our "marathon EM sessions".

I would like to also acknowledge all of my excellent co-workers and friends in the EM group. In particular, I would like to thank Xianbo Yang not only for his friendship, but also for his knowledge and helpfulness in the cleanroom. Without him, I highly doubt this thesis would have been possible. In addition, I would like to sincerely thank Dr. Raoul Ouedraogo for the use of his GA optimization code that is the basis of the optimizer used in this work. Further, I would like to thank Benjamin Crowgey for his friendship and our frequent talks about sports that successfully distracted me from completing this thesis at an earlier date. I would also like to thank Junyan Tang for his help in soldering connectors, as well as his

many tang-isms. Last but not least, I would like to thank my former co-worker Dr. Jose Hejase for not only his help with my research, but also his endearing friendship. Without Jose I would never have came to work with Dr. Chahal. I don't think I could have ever found a better mentor and friend.

Most importantly, I would like to thank my wife Melissa Myers for all her support and love throughout this process. Without her I would have never known my beautiful daughter Sunshine and my amazing son Shane. For this I will be eternally grateful to her. Additionally, I would like to thank her parents and brothers for putting up with me all these years. I would also like to thank my parents Barbara and Darryl Myers. Without them I would obviously not be here. Their love and support has helped mold me into the person I am, and I am extremely lucky to be their son.

TABLE OF CONTENTS

LIST OF TABLES

LIST OF FIGURES

CHAPTER 1

Introduction and Background

1.1 Terahertz Overview and Background

The terahertz (THz) frequency spectrum has long been one of the least explored sections of the electromagnetic spectrum. Typically defined from .1 to 30 THz, the THz spectrum lies in the frequency gap between traditional microwave devices and optics, as shown in Figure 1.1. Although some researchers consider the low-THz spectrum (100-300 GHz) as mm-wave, in this dissertation, 100 GHz and up will be considered the start of the THz spectrum. While there are many reasons for a lack of scientific advancement in this area, the absence of efficient, cost-effective THz technologies has been a major detractor for many years [1].

Recently, there has been a significant increase in the research community towards developing THz devices [2] - [4]. This has primarily been caused by the advances in commercially available THz systems and sources over the last decade. While a few different types of design topologies have been developed, these systems are primarily made possible through the development of femtosecond laser devices. By exciting photoconductive semiconductor switches which act as gate and pump lasers, mode-locked femtosecond lasers can be used to generate THz signals [5] - [6].

To generate time-domain THz signals, the laser is first incident on a beam splitter which

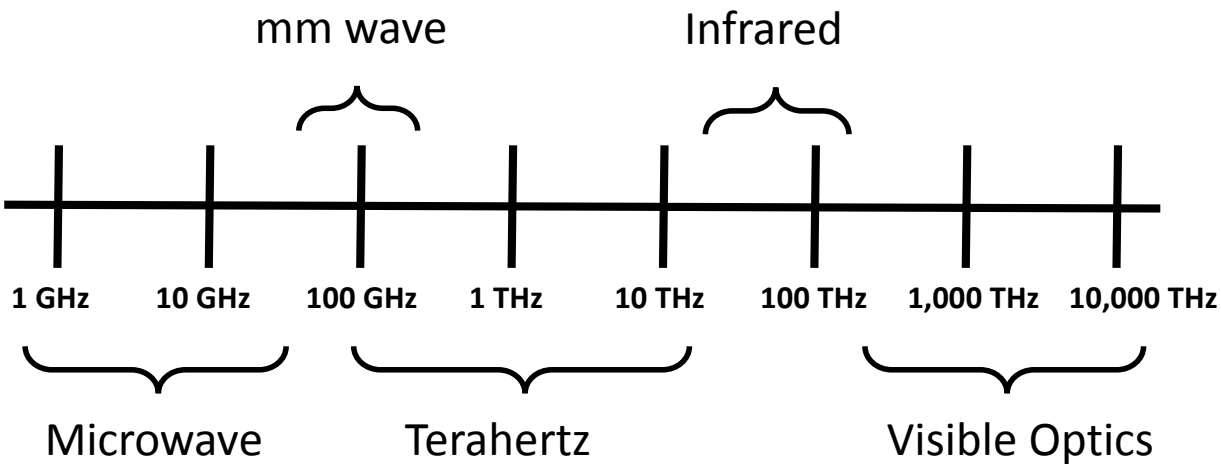

Figure 1.1 Microwave to visible optics frequency spectrum.

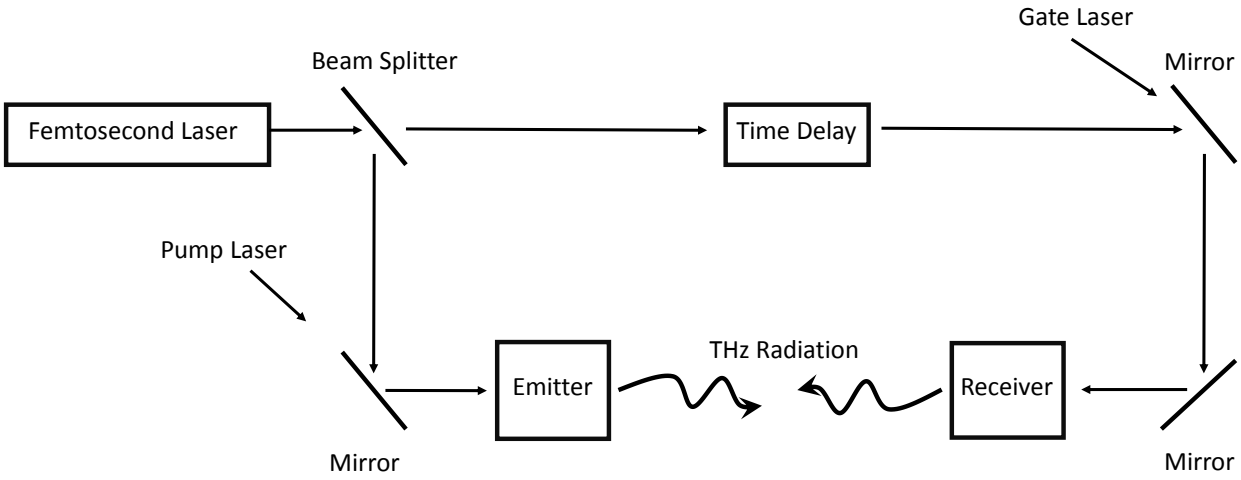

Figure 1.2 Diagram of femtosecond laser-based THz system.

splits the signal between a mirror (this acts as the pump laser) and a delay fixture, the output of which acts as the gate laser. The pump laser is used to excite a switch at the emitter of the system, which in-turn generates THz radiation when the pump laser is on. Conversely, the gate laser is used to trigger the receiver switch so that the radiation can be detected. A variety of optics and lensing can be used at the emitter and receiver to generate focused, collimated beam. The block diagram of a typical time-domain THz system in transmission mode is shown in Figure 1.2. Similarly, the same system can be used for reflection measurements with a metal plane placed at the correct angle between the emitter and receiver. Typically, most commercial THz systems can measure between 100 GHZ and 2.5 THz. Both frequency and time-domain commercial THz systems are shown in Figure 1.3.

Thanks to these improvements in THz systems, the frequency spectrum has developed many current and potential applications in a wide variety of areas. This spectrum is often rich with unique material spectral fingerprints, making it particularly advantageous for spectroscopy [7] and sensing [8]. THz radiation is also non-ionizing, making it safer than current X-ray imaging technologies for use in medical applications [9]. Additional areas of interest include high bandwidth communications [10], nondestructive evaluation [11], and hidden object detection for security applications [12].

Spectroscopy has historically been a prominent application of the THz regime [13]. THz spectroscopy has been used for years in astronomy to discover the compositional makeup of stars and other solar systems [14]. THz spectroscopy has also been used to investigate proteins, DNA, and other bio-molecules by studying their frequency vibrational modes [15]. THz spectroscopy has been used heavily in the pharmaceutical industry. In particular, [16] THz spectroscopy is used for polymorphic identification of drug tablets. In [17], the crystalline structure of pharmaceutical materials is also studied using a similar technique. The temperature dependance of carbamazepine (a common anticonvulsant) is also investigated with pulsed spectroscopy in [18].

THz sensing has also been used in many applications. Due to the small wavelength of

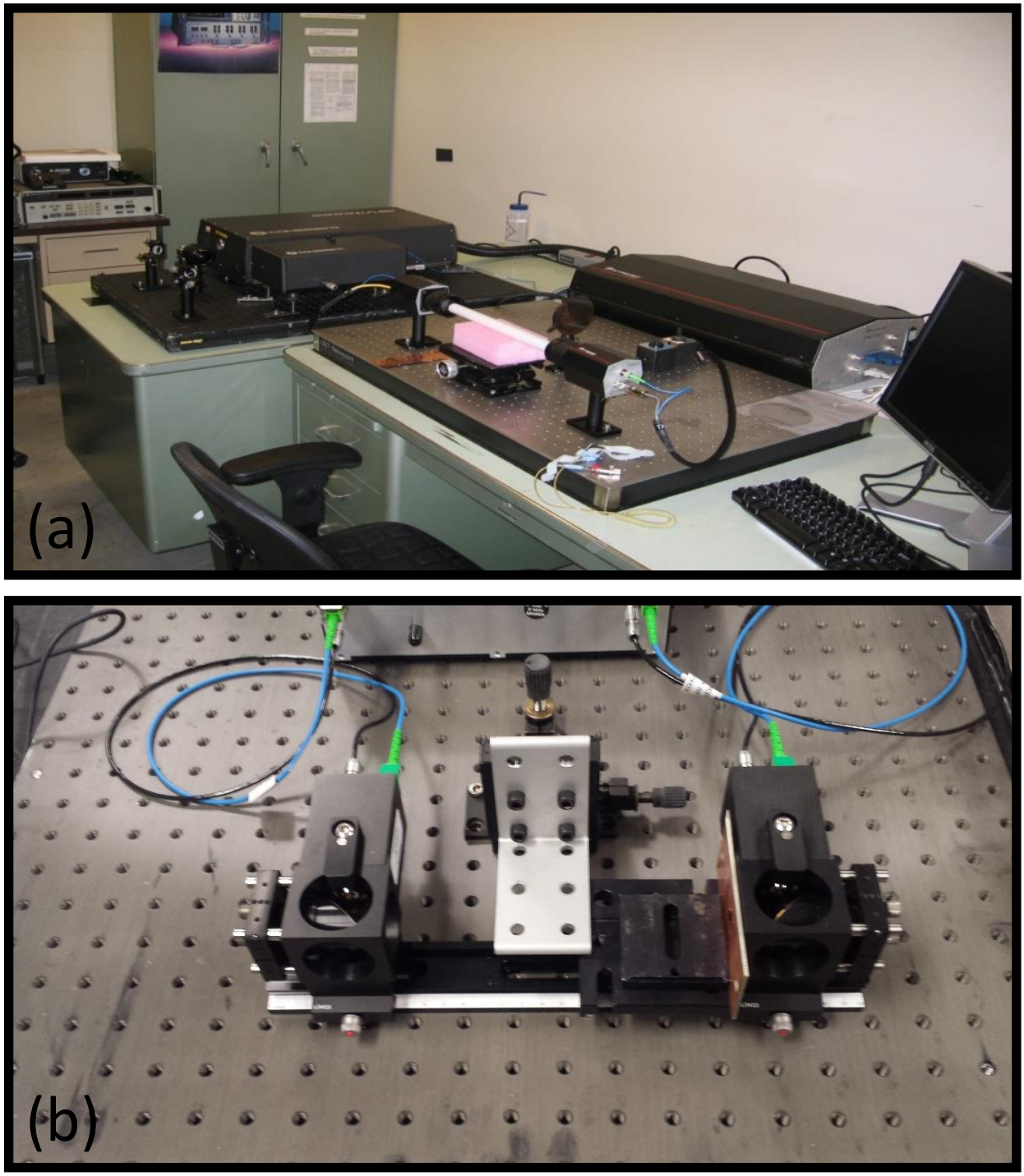

Figure 1.3 Commercial THz systems for the (a) time-domain (b) frequency domain.

THz signals, extremely small samples are able to be sensed accurately. In [19], metamaterials operating in the THz frequency range are used to detect thin-film samples. Additionally, THz sensing has again been used in many biomedical applications, such as detection of skin hydration [20], sensing in corneal tissues [21], and marker-free DNA analysis [22].

In addition to the biomedical applications of THz sensing, THz imaging has been widely adopted in tissue characterization and cancer detection. Due to the non-ionizing nature of THz waves, these methods are safer in comparison to X-rays and can therefore be repeated as necessary [23]. In particular, due to the low penetration depth of THz radiation, THz imaging is easily applicable to the skin and teeth. In [24], THz pulsed imaging is used to detect cancerous growth in breast tissue. Further, [25] uses THz pulse imaging reflections to determine skin cancer growth in the upper layer of skin tissue. In addition, [26] uses 3D imaging on dental tissue to determine attributes of teeth, such as enamel thickness and erosion.

Another huge area of interest in the THz research community is the use of THz devices for hidden object detection and security applications. The most popular of these applications in current production is the mm-wave imaging booths used by the TSA. mm-wave and THz imaging is attractive for these applications due to the abundance of materials that are transparent to THz radiation, such as paper, plastics, and many other dielectric composites [27] - [29]. This allows THz radiation to essential 'see through' concealing barriers. For example, many explosives [30], firearms [31], and illegal drugs [32] have detectable characteristics when exposed to THz radiation.

In addition to hidden object detection, THz imaging has been widely investigated in the non-destructive evaluation (NDE) community. In [33], THz is used for NDE of metallic surfaces to determine surface roughness. Similarly, [34] uses THz imaging for corrosion of metals beneath paint surfaces.

1.1.1 Realization of Integrated THz Circuits

In the previous section, the applications of THz radiation was introduced. While these applications are numerous, there are serious difficulties successfully realizing efficient THz circuits and systems. This is due to a number of issues, but in particular current electrical technologies are not capable of carrying large frequency signals with low loss.

In addition, current THz systems, as shown in the previous section, are relatively bulky and quasi-optical in nature. This makes the realization of compact and efficient THz circuits difficult to realize. However, the ideal solution would be to create completely integrable THz circuits on the wafer level that are efficient, compact, and cost affordable. In order for this to be accomplished, a number of both active and passive devices must be realized.

Many active devices must be realized, such as efficient THz diodes, transistors, amplifiers, modulators, and detectors, as shown in Figure 1.4. However, before the necessary active devices are realized, efficient passive building blocks must also be developed. While a number of passive devices are necessary to develop THz integrated circuits, waveguides and filtering are of particular importance.

Waveguides in-particular are a difficult challenge in the THz spectrum, as metal has particular high skin-depth losses in the THz spectrum. This makes traditional waveguides, such as microstrips and striplines, very inefficient. Therefore, THz waveguides must be based on dielectric or other non-metal structures which further complicates the design process. Further, actually coupling THz radiation into the waveguides, especially with current quasi-optical THz systems, is especially complex and inefficient. The next section of this dissertation will review some of the current waveguiding and filtering techniques, as well as current coupling methods proposed in the literature.

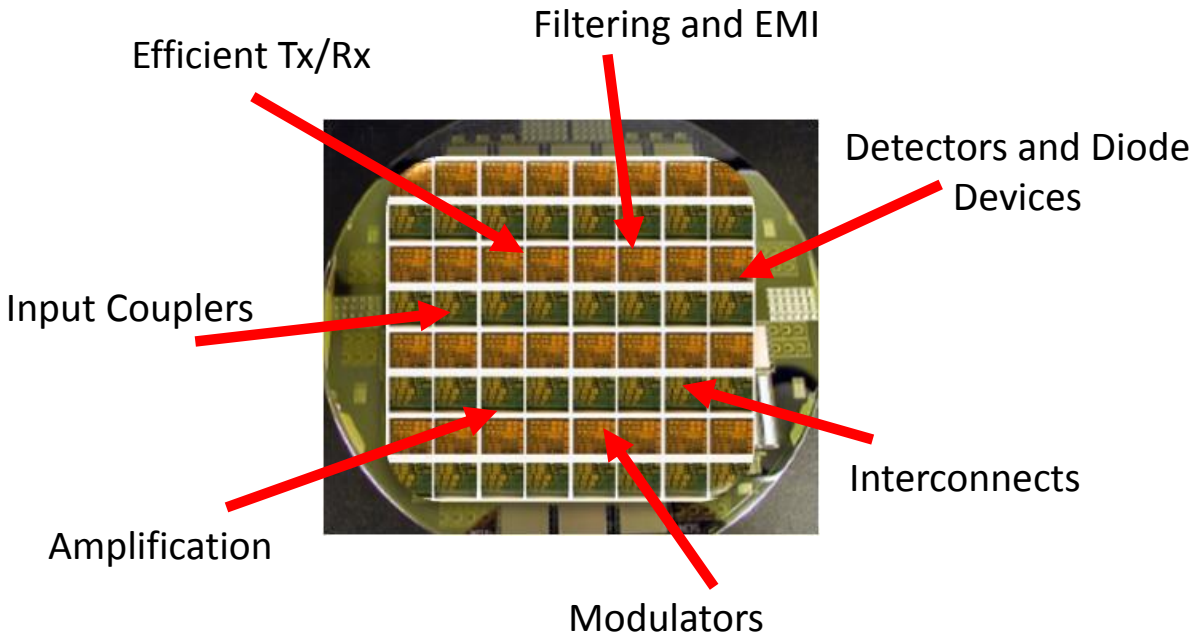

Figure 1.4 Some of the components necessary to realize THz integrated circuits.

1.2 Current Research Topics in THz Technologies

While the previous discussion covers some of the many applications of THz radiation that have recently been explored, this section will delve into three more technical aspects of THz research that have been presented in the literature. All three of these subsections are of particular importance in the realization of modern THz circuits and systems. First, THz waveguides in the current literature are explored. Next, current coupling methods that are used to excite the waveguides using modern THz systems are also investigated. Finally, modern THz filters are explored as well as current design methodologies and implementations.

1.2.1 THz Waveguides

Traditional waveguiding structures, such as microstrip lines and, striplines, and metallic waveguides have high attenuation constants at THz frequencies [35]. This leads to the necessity for the design of THz waveguides and devices that are much different than their RF and microwave counterparts. Due to the unavailability of efficient THz waveguides and interconnects, THz circuits have been slow to develop.

However, in recent years, a number of alternative THz waveguides have been introduced. These waveguide designs range from traditional metallic-type waveguides with unique aspects that lower their attenuation constants, to much more novel concepts such as metamaterial and plasmonic type structures. In this section, a general overview of many different types of THz waveguides will be presented, as well as some of the problems associated with the currently presented waveguide designs.

Initially, more traditional structures, such as thin wires were investigated. For example, in [36] cylindrical wire waveguides are investigated as THz waveguides by exciting surface waves on the wire. In this case, radially polarized THz radiation is incident on the wire, with a scattering mechanism used for input coupling.

Another wire based method is shown in [37], where THz radiation is coupled through onto

cylindrical wires which support low order radial mode propagation. These waveguides show virtually no dispersion, relatively low attenuation, and are relatively simple. However, both of these wire-based waveguides suffer from being difficult to implement, and not compatible with integration.

Hollow cylindrical metallic waveguides with thin inner dielectric coatings have also been studied for THz wave propagation, with the dielectric coating chosen to be much smaller than a wavelength[38]-[39]. The waveguides are coated with dielectrics in order to avoid some of the skin-depth losses that the traditional metal waveguides suffer from in the THz region. The waveguide show the use of both single and multi-layer dielectric coatings and are designed such that the low-loss transmission of the HE_{11} propagating mode is excited. Again, while these waveguides are capable of efficiently transmitting THz radiation, they are relatively bulky and difficult to implement.

Photonic bandgap (PBG) structures have also been studied in detail for THz wave propagation. In [40], two dimensional PBG structures are implemented with TEM mode propagation within metal parallel plate waveguides. In [41], one-dimensional photonic metal parallel plate waveguides are presented. The waveguides are designed to operate in a spectral region of .5-3 THz. Through this range, the waveguide has a high throughput with up to 40 dB of dynamic range.

Other metamaterial type structures, such as electronic bandgap materials made of dielectric structures have also been investigated. In [44], concentric cylindrically periodic dielectrics are used to realize low-loss propagation in the THz frequency spectrum. In this case, most of the power is contained within the air core region of the cylinder, and a propagating TE_{01} mode is excited. Another EBG waveguide is shown in [45], where an all-dielectric waveguide is developed through rapid polymer-jet prototyping.

Another recently proposed solution is the dielectric ribbon waveguide. Dielectric ribbon waveguides have been shown to be efficient carriers of THz waves by containing propagating THz radiation primarily in the air above the dielectric [49]. However, ribbon waveguides

suffer large losses at bends or curves due to the confinement of the fields in the surrounding area, making them non-ideal circuits and systems which require sharp bends or complex geometries. Recently, there have been promising results coating the dielectric core with high permittivity dielectrics in order to better contain the field in the center of the waveguide [50]. Figure 1.5 shows the geometry and Unfortunately, including the cladding regions tends to increase the fabrication complexity of the waveguides.

Ribbon waveguides have also been investigated for THz wave propagation when made of semiconductor materials. Typically, these ribbon waveguides do not require extra cladding materials due to the high permittivity difference between the semiconductor and surrounding air. As an example, in [51] - [52] highly resistive silicon is used on a glass substrate to create low-loss ribbon waveguides up to 500 GHz.

Another promising approach for guiding THz waves is through surface plasmonics. Surface Plasmons (SPs) are coherent, wave-like oscillations of free charges, which often reside at the surface of metal-dielectric interfaces, as shown in Figure 1.6. SPs have been exploited at optical wavelengths for numerous applications [47]-[48]. The SP phenomena is observed near the plasma frequency of a material, which in the case of a metal, typically lies in the UV spectral region. This makes SPs very weakly confined to metals in the THz frequency spectrum. However, the plasma frequency of metals can be altered by periodically texturing the surface of the metal [60]. Textured metal surfaces have been studied in great detail for the design of THz waveguides in [53]-[55]. These artificial metal-dielectric composite structures support so-called *spoof plasmons*.

A common method of tailoring the plasma frequency of a metal involves drilling an array of holes along the surface, provided that the periodicity between the holes is much less than a wavelength. This type of plasmonic waveguide has been studied extensively in the THz region [56]-[59]. The geometry of such a waveguide is shown in 1.7. The effective plasma frequency of the textured structure can be designed based on the resonance of the individual apertures [58]. In fact, the resonance of one cavity can be shown to be exactly

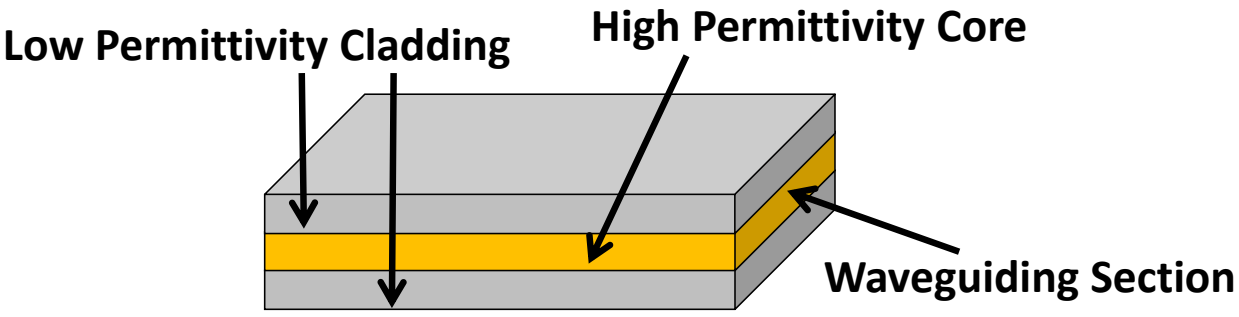

Figure 1.5 Typical configuration of a dielectric waveguide with high permittivity claddings.

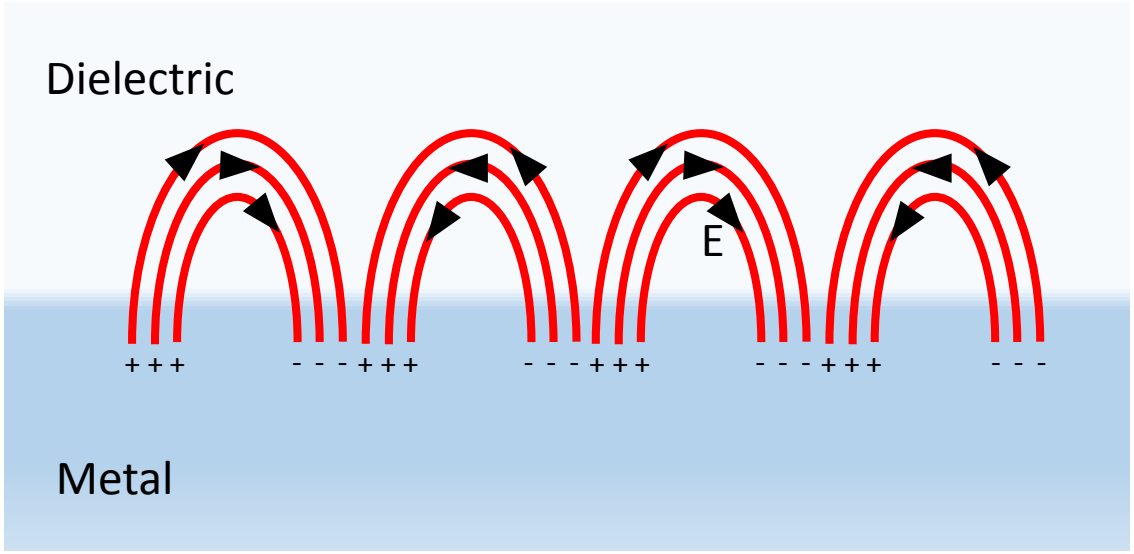

Figure 1.6 Plasmon osculations occurring near a metal-dielectric interface.

equal to the plasma frequency of the composite structure [60]. While the operating frequency of these composite metal structures can be tailored to a desired frequency, their practical application is limited. Commonly, these waveguides are built directly from metal substrates, which does not make them easily integrated in THz circuits. Also, the associated fabrication requirements to create these devices are expensive and not readily available.

While many of these proposed THz waveguides have been shown to transmit THz radiation, most are either inefficient compared with traditional RF methods, or are difficult to implement with integration level packaging in THz circuits. In the case of the metallic wire type waveguides, it is relatively clear that simple wires cannot be implemented in modern THz systems. While the hollow cylindrical waveguides introduced also show good THz propagation characteristics, they are relatively bulky, and would also be difficult to implement in integrated systems. Similarly, PBG and EBG type structures could be implemented on-wafer, but the currently proposed structures are mostly based on metallic waveguides. Other introduced waveguides, such as the dielectric ribbon waveguide, and the plasmonic type waveguides, suffer from a variety of problems, such as complex fabrication requirement and curvature losses. This leaves the THz research community in dire need of integration compatible, low-loss waveguides and interconnects.

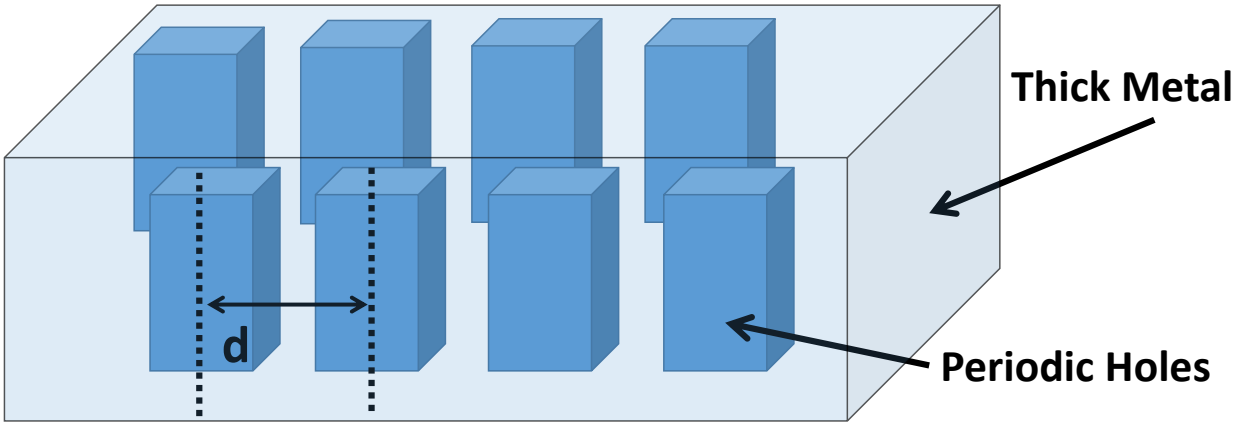

Figure 1.7 Spoof plasmonic type waveguide for THz frequencies.

1.2.2 THz Coupling Methods

While there have been many advances in THz waveguides, actually coupling radiation efficiently into waveguides has not been well explored. Typical THz measurement systems are quasi-optical in nature, with high speed fiber optics and receiver/transmitted heads. This makes the transition between the measurement system and desired waveguide difficult, especially when the waveguide is planar or integrated.

Many of the currently proposed THz waveguides are difficult to implement, inconvenient, or complex coupling methods [62]. In fact, many currently proposed waveguides have simply non-existent coupling methods, and are investigated only theoretically or through simulation, and then measured at much lower frequencies to be used for a proof of concept [63]-[64]. For example, in [63], plasmonic THz waveguides are investigated at THz frequencies, and then scaled to much lower frequencies of operation and measured with simple SMA connectors.

Other coupling methods have been suggested, but in general have been very complex and mostly inefficient. In [56], a plasmonic semi-circle groove is used to to couple incoming THz radiation onto a similarly constructed plasmonic waveguide. The signal is then measured along the surface of the waveguide with a ZnTe crystal detector. This method only provides a one way coupling method, as the signal is picked up with the detector. Also, this method is difficult to implement and very inefficient. The overall setup of the coupling method is illustrated in Figure 1.8.

Another method is shown in [51], where silicon dielectric waveguides are measured in the low THz frequency range. The waveguides are measured using a combination of two metallic rectangular waveguides acting as the launch points, with the dielectric waveguide placed in the mouth of each waveguide. While this efficiently acts as a coupling mechanism to the dielectric waveguide, it is relatively difficult to implement in a real-world system. The overall setup of this coupling method is shown in Figure 1.9.

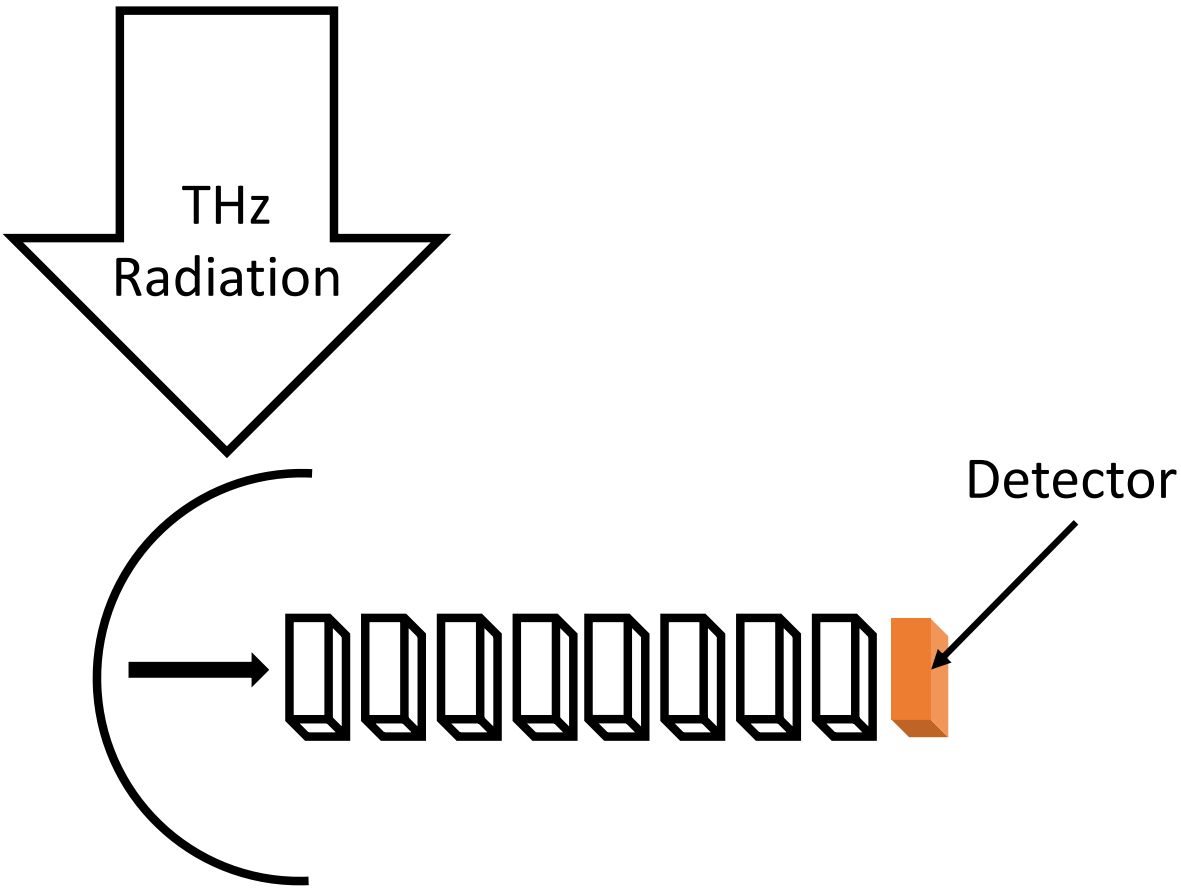

Figure 1.8 Semi-circular plasmonic groove used for coupling THz radiation to plasmonic waveguides.

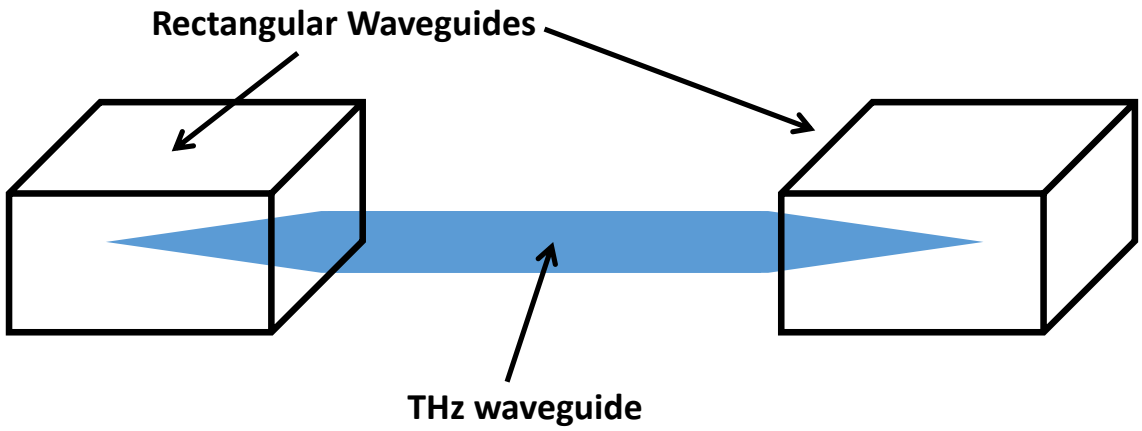

Figure 1.9 Rectangular waveguides used as couplers to THz waveguides.

1.2.3 THz Filters

An additional component of great interest in the THz research community are electromagnetic filters. In this case, a variety of filters are necessary, including high-pass, low-pass, and band-pass filters. However, typical THz filters are primarily based on optics designs. This makes them relatively bulky, difficult to measure, and not integration compatible. In this section, some common optical based filters and other currently proposed THz filters are reviewed.

Many types of filters have been demonstrated to work well above the THz frequency range in a variety of fashions. Typical optics-based filters rely on stacked layers of dielectric to achieve a desired filtering response [65] For example, glass pieces staggered by a quarter wavelength between layers can be used to create bandpass filters. The properties of the filter re primarily influenced by the thickness of each glass layer, as well the dielectric constant of the material. The implementation of this filter is shown in Figure 1.10.

Another popularly used optical structure is a 3D photonic crystal based with a complete band gap at the micron scale was first designed in [66]. This structure is simply a series of stacked logs in different directions, called a woodpile. The geometry of such a structure is shown in Figure 1.11. Based on the thickness of the logs, the material they are created from, and the amount of logs in the stack, the properties of the structure can be used to create a filtering mechanism. This has been explored recently in the THz spectrum as well. In [67], a 3D printed woodpile structure is created which acts as a strong bandstop filter. The potential for the filter to also be used as a sensor by changing the dielectric constant inside the woodpile is also discussed.

In [68], a THz filter based on a composite metal-dielectric-metal structure is introduced. The filters are primarily used for their stop-band characteristics in the application of band-pass filtering. Dual layer structures are also investigated to improve the filtering properties. This filter is studied primarily through simple cascading analysis, and tuning of the filter

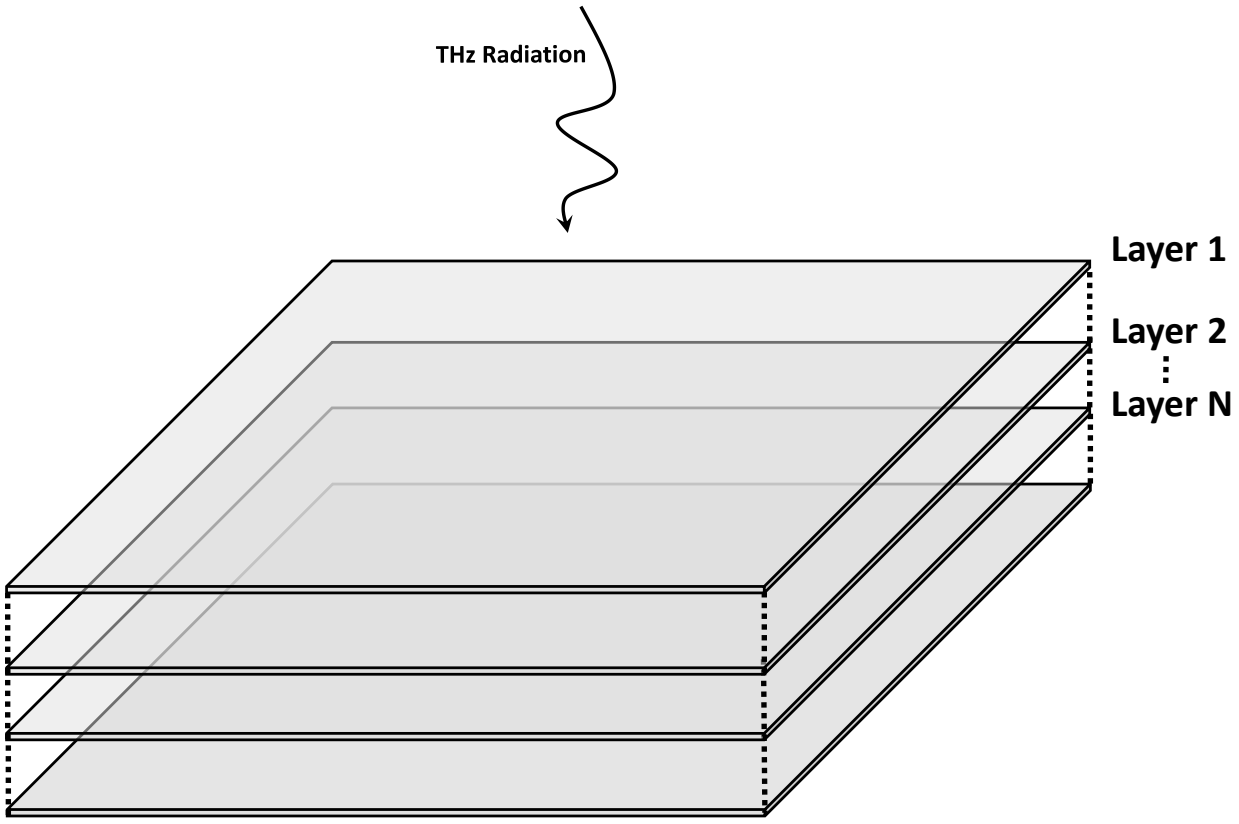

Figure 1.10 Filter based on multiple dielectric stacks.

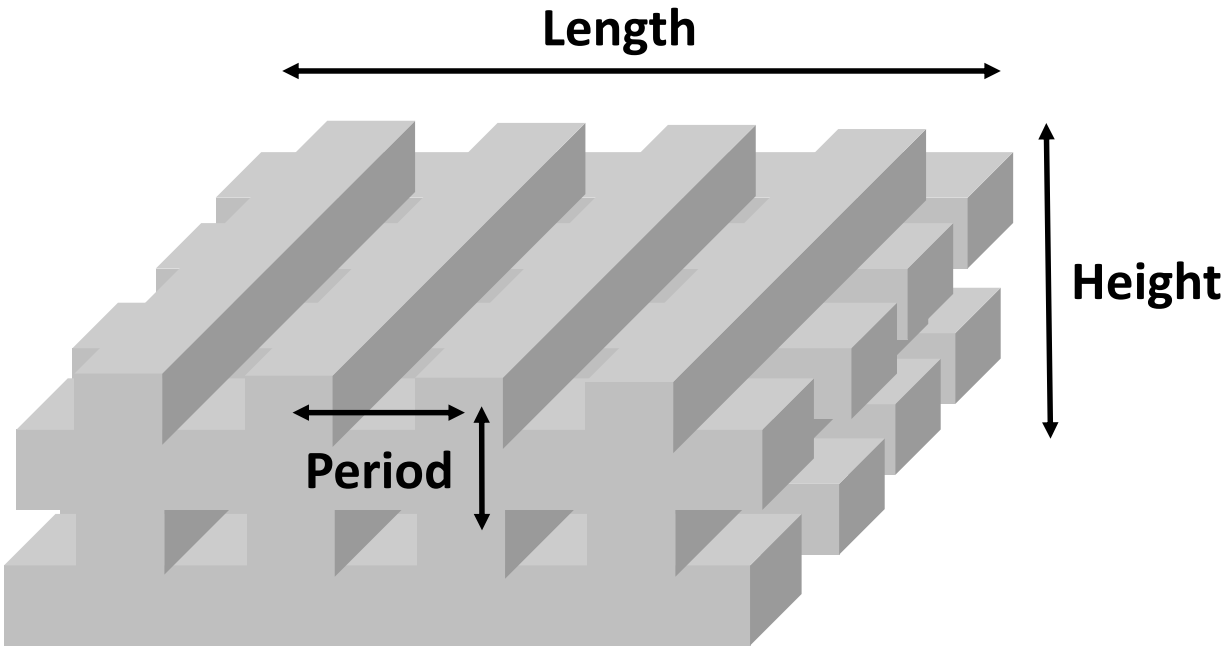

Figure 1.11 Periodic woodpile based filter.

bandwidth and center frequency is investigated by modulating the parameters of the structure.

The work presented in [69], a triple-channel THz filter is introduced which is capable of multi-resonance in the THz spectrum. The filter is based on a silicon multi-cavity resonant system that is experimentally investigated using a backward wave oscillator. The three resonance peaks in the filter are analyzed and the first is determined to come from a Fabry-Perot resonance caused by thick cavities in the structure, while the others are caused by coupling into the two central cavities.

Other more exotic solutions for THz filtering have also been developed. Similar to the waveguides shown earlier, plasmonic based structures have also been shown to act as effective filters in the THz region [70] - [72]. For example, In [73], a plasmonic high pass filter is designed by engineering the dielectric properties of a thin-wire lattice. In this case, the high-pass point of the filter is designed to be the transition point between a positive and negative dielectric constant, known as the plasma frequency. At this frequency, a sharp change of the reflection and transmission coefficients make the structure a high-pass filter. This allows the authors to achieve high-pass filter characteristics well above 0.7 THz, with a two dimensional cubic lattice.

In [74], a multi-band THz filter is proposed by utilizing the positive and negative refractive indices of a photonic crystal prism. In this case, a passband filter is implemented with a prism formed from a 2D hexagonal arrangement of metallic rods. The filter is able to operate over an approximate bandwidth of 250 GHz, starting at 1 THz.

Metal hole arrays have also been studied to provide very large bandwidth THz filters when stacked in multiple layers. In [75], a THz wideband filter based on a double layer of metal holes is developed. This is created by simply perforating a metal layer with circular air holes. The transmission characteristics of the filter are determined by the accumulation of scatting and plasmon polarations. Overall, the filter has a center frequency of .8 THz, with a relatively wide bandwidth of 400 GHz.

Tunable THz filters have also been investigated in the literature [79] - [80]. In [81], an optically controlled THz filter is presented which exploits the electron-hole pairs in a semiconductor quantum well to attenuate THz frequency content. This is accomplished in a mixed GaAS/AIAs multiple quantum well sample. In this case, the transmission spectra is able to be controlled over a wide frequency range for tunable filters.

Another solution is shown in [82], where a thermally tunable filter based on a simple photonic crystal structure is presented. The filter is based on a small transmission band, which originates from a small defect mode that appears in one of the crystals. This filter allows for tuneability of approximately 20 % over a wide range in the THz frequency spectrum. However, a large temperature swing is required to tune the filter significantly.

While the above filters work well as standalone components, they require complex fabrication steps and design procedures. Specifically, they are relatively bulky, and would not be compatible with integration level processing at the wafer level. While there has been some movement in the research community to create THz component designs that are compatible with wafer-level integration [76]-[77], filters are specifically difficult to achieve. This is primarily because thin-film THz filters in the current literature do not display as large of a rejection/acceptance band, nor have they been shown to be as flexible in filter design [78].

1.3 Dissertation Overview and Objective

To realize any modern integrated electrical system, a number of passive components are necessary. In particular, waveguides are needed to act as interconnects between many of the active components within the system. In addition, a method of coupling an excitation into the waveguides efficiently is necessary, weather it is a simple SMA connector at lower RF frequencies coupling into a microstrip, or a laser coupling into a fiber optics cable in the optical spectrum. Finally, a number of high-, low-, and band-pass filters are necessary both for elimination of noise, but also to control unwanted harmonics and other EMC issues.

As shown in the previous sections, many THz filters and waveguides have been developed. However, they are not easily fabricated, measured, or are they integration compatible with modern semiconductor wafer level fabrication.

In this Dissertation, THz filters, waveguides, and coupling methods are developed which are compatible with modern semiconductor wafer level integration. This overall objective is illustrated in Figure 1.12. Chapter 2 introduces methods of efficiently coupling THz radiation between commercial quasi-optical THz systems and integration compatible THz components. These methods include over-moded waveguide couplers, coupling between waveguiding structures, and dielectric focusing probes.

Chapter 3 investigates the use of dielectric ridge waveguides made of silicon. A theoretical effective index method is applied to determine the modal propagation properties of the waveguides as well the attenuation of the structures. FEM simulation is also carried out to verify these results. Various ridge waveguides made on silicon wafers are investigated through measurement and determined to provide low-loss waveguiding properties in the THz spectrum. Chapter 4 then focuses on the design of thin-film integration compatible THz filters. These filters are designed with multi-objective evolutionary algorithms coupled with FEM modeling. Bandwidth, stopband characteristics, multi-resonance, and other properties of the filters. The filters are measured using a commercial THz system, and shown to match well with the optimized expectations.

Finally, chapter 5 introduces another waveguiding structure built with thin-metal periodic structures on thin-film substrates. These structures efficiently guide THz waves along the surface of the textured metal structures. With these structures, other passive THz circuits, such as power splitters and sensors, are developed. The waveguiding structures, as well as power splitter, are measured in conjunction with the dielectric focusing probes developed in chapter 2, and show to provide high transmission properties at specific design frequencies.

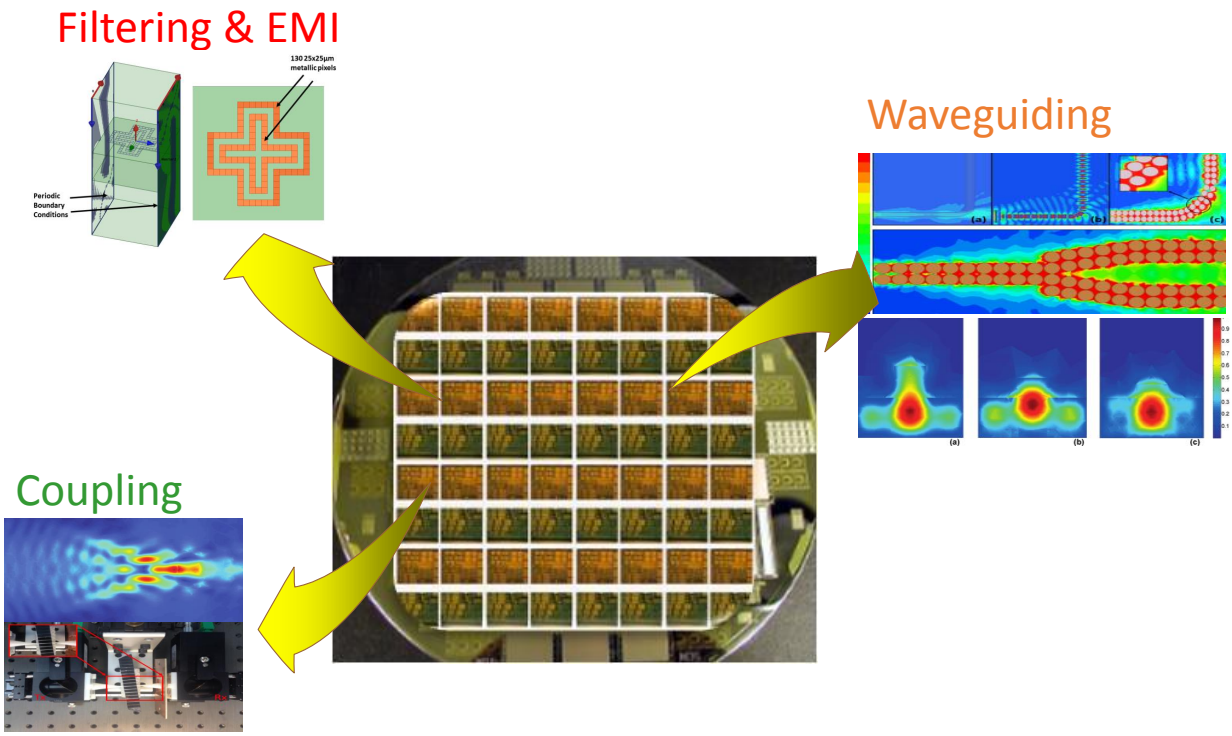

Figure 1.12 Overall objective of this dissertation.

CHAPTER 2

Coupling Methods

In this chapter, methods of coupling between modern THz systems and the waveguides and other devices presented within this thesis are established. A method of coupling between a THz source and waveguide is implemented by the use of dielectric focusing probes placed between the transmitter and receivers of the system and the waveguides. The probes are theoretically investigated through simulation. In addition, the measured characteristics of the probes are investigated, and the probes are shown to work efficiently in a THz waveguide measurement. These probes are then used throughout the rest of this dissertation to couple into other devices, particularly in chapter 3 and 5.

2.1 Dielectric Focusing Probes

2.1.1 Probe Design Simulation

The dielectric probes proposed in this work are made of High Density Polyethylene (HDPE). HDPE possesses very low loss properties in the THz spectrum, with a typical dielectric constant of $\epsilon_r = 2.4$ and $\tan\delta = 0.01$ at 300 GHz [117]. The probe design builds upon the demonstration of wide band dielectric probe in [**?**]. The probes are comprised of three primary sections: a plano-convex lens, cylindrical focusing region, and tapered cone. The

first section of the probe, the plano-convex lens, ensures proper wave polarization and focuses the wave to a point in the subsequent cylindrical region. The cylindrical focusing region is followed by the tapered cone. The tapering of the cone is primarily responsible for the focusing effect of the probe at its tip. Based on the taper design, the focal point of the probe can be adjusted. Since the probes are intended to be used as couplers between a THz system and waveguide, the probes are designed so that the focal point is directly at the tip. Figure 2.1 shows the geometry of a sample probe as well as the proposed setup when used to probe a THz waveguide.

To ensure the field is well confined within the probe and that the focal point of the probe is near the tip, a small section of the probe encompassing the region closest to the tip of the probe is first simulated. In this case, the commercial FEM solver HFSS 15.0 is used. Only a small section is simulated as the entire probe is many wavelengths long, and therefor too large to be fully meshed. The field in both the lateral and vertical directions throughout the probe and the surrounding area is shown in Figure 2.2. Clearly, the field is well confined to the probe in both the vertical and horizontal planes, with the only field penetration near the tip of the probe. Also, the field is highly localized near the tip of the probe, confirming that the focal point is directly at the tip.

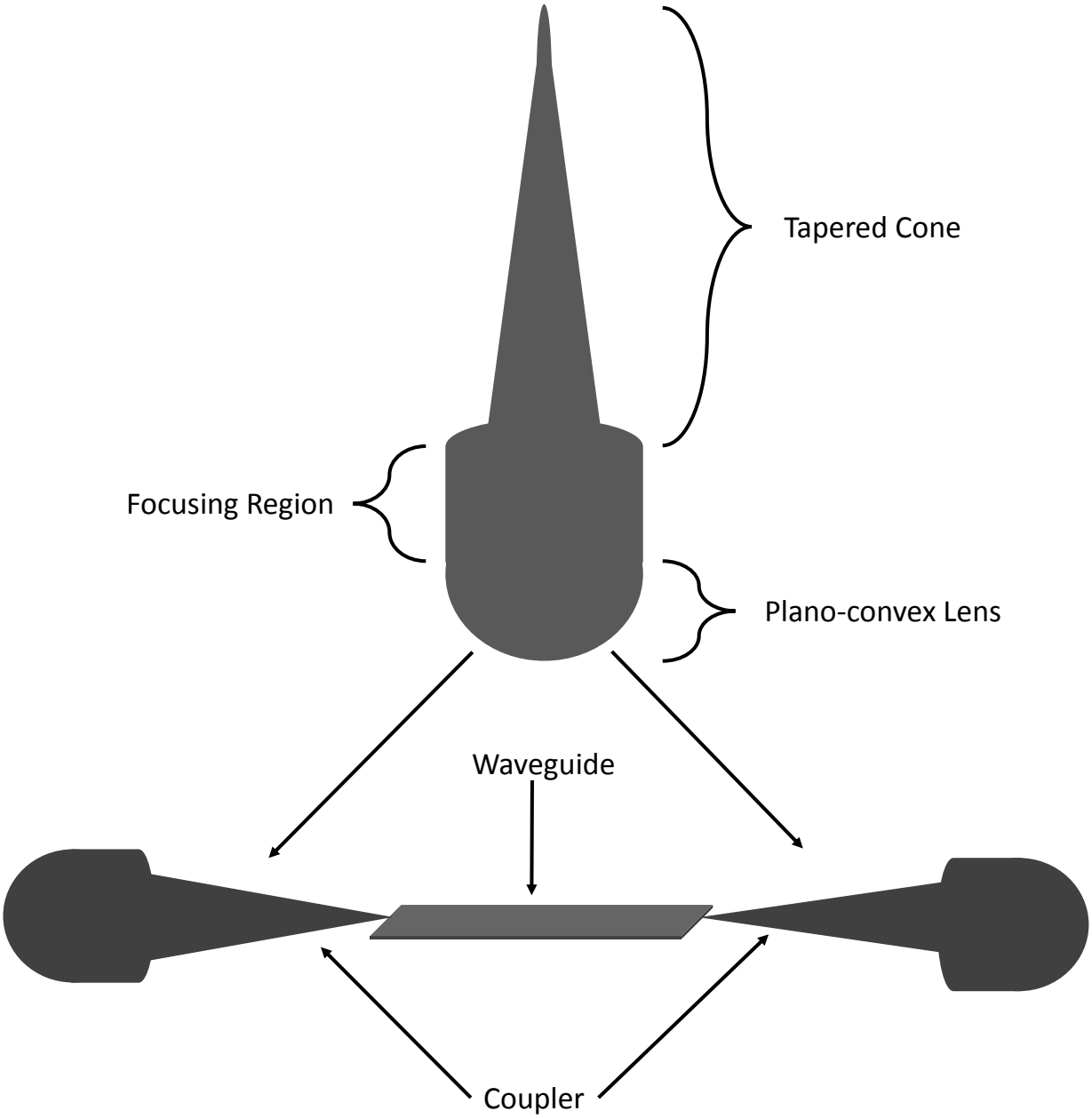

Figure 2.1 Proposed coupler geometry and setup.

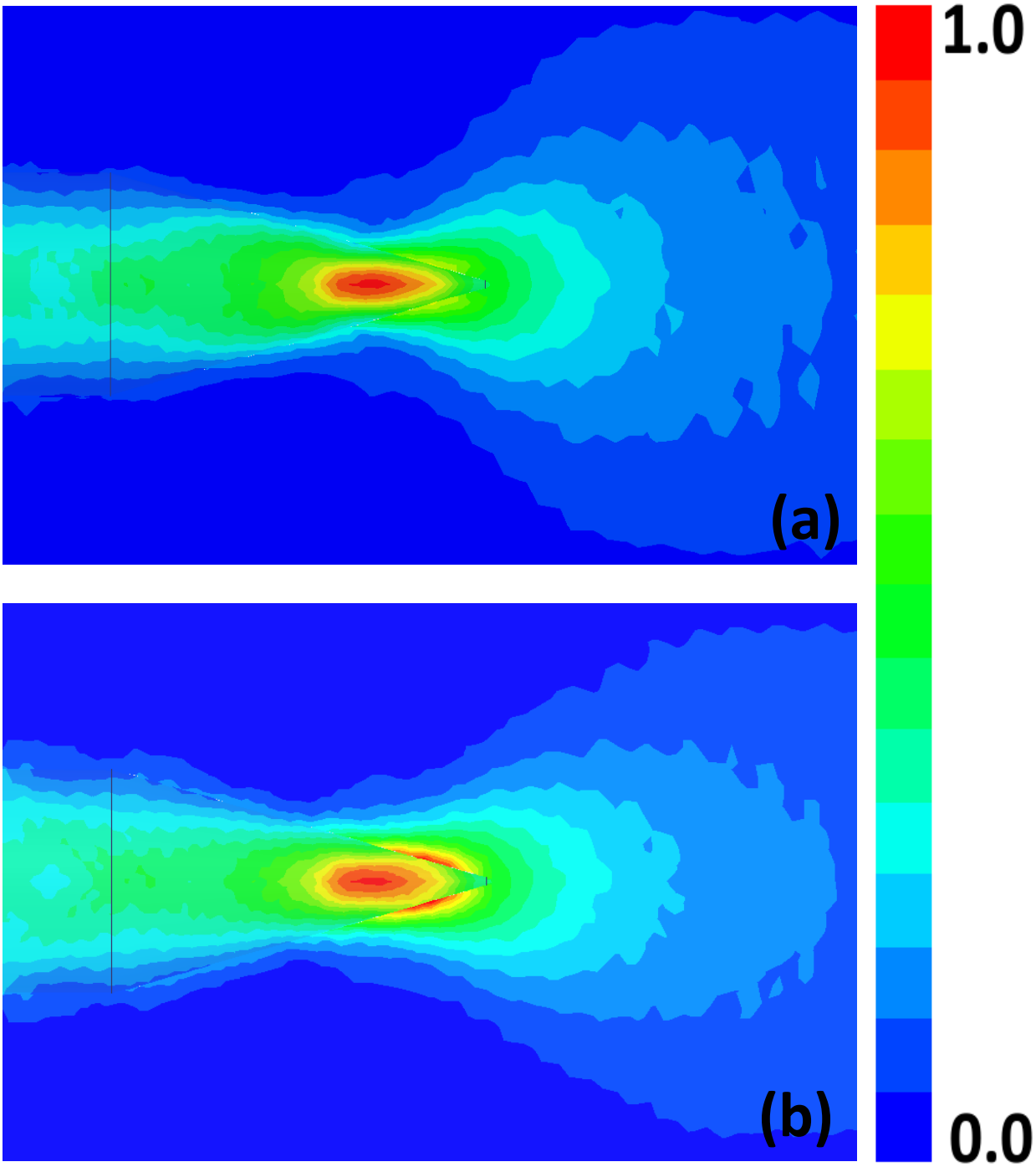

Figure 2.2 The simulated electric field confinement in (a) horizontal and (b) vertical planes in the dielectric probe.

2.1.2 Probe Verification

A quasi-optical THz measurement setup is used to characterize the probes. The THz signal is generated using an Emcore PB-7200 commercial frequency domain system. This system is made up of receiver (Rx) and transmitter (Tx) heads that are interfaced with sources through fiber-optics. The system is capable of measuring transmission between the Rx and Tx heads from 0.1 to 2 THz, with a frequency resolution of 100 MHz. The Rx and Tx heads are capable of being moved on a railing system separating each optical head. The probes are fabricated by taking a long HDPE rod and machining the geometry of the rod to fit the probe design. The probes are then further sharpened using sandpaper along the tapered cone section. An adapter is also fabricated using 3-D printing so that the probe can be fit directly into the THz system receiver/transmitter head. The fabricated probe inserted into the coupler and interfaced with the receiver of the THz system is shown in Figure 2.3.

To ensure the probes behavior matches that predicted by simulation, the transmission between each probe is first measured at various distances. The THz system measures signal power in arbitrary units between the Tx and Rx optical heads. Therefore, the exact power transmitted through the system is unknown, but comparisons between measurements can be made. First, the probes are aligned tip-to-tip, such that all the power is directly coupled through each probe. The probes are then slid along the railing and the transmission is recorded with spacings of 1, 2, and 3 cm between the probe tips.Figure 2.4 shows a continuous measurement of the probe-to-probe transmission of the system at each probe spacing from 100 to 300 GHz. Clearly, when the probes are placed directly tip-to-tip, the transmission through the system is largest. However, when distance is introduced between the probe tips, the signal is decreased. This confirms that the focal point of the probes is directly at the tip, as expected, given that power falls off with increased displacement.

2.1.3 Implementation with Commercial THz Systems

Now, to investigate the potential of the probes in waveguide coupling, the system is fitted with a probe in both the Rx and Tx heads. The probes are then aligned with the waveguide such that the tips are directly touching the waveguide edges. In this case, a simple dielectric ribbon waveguide is used as the THz waveguide. This waveguide is made from silicon, with a thickness of 250 μm and a width of 1 mm. More details on the design of similar ribbon waveguides for the THz spectrum can be found in [92]. The overall measurement setup of the waveguide probing system is shown in Figure 2.5.

In order to characterize the waveguide coupling method, the loss due to the couplers, as well as the loss due to the coupling into the waveguide, are of particular interest. To find the losses associated with these effects, a number of THz measurements must be taken. First, a reference measurement with nothing between the Tx and Rx head is taken. The distance between the heads as will be needed to contain both probes and the dielectric waveguide was used, yielding the total system power P_t. Next, a measurement of both probes in the tip-to-tip configuration is performed, which produces the total power of the system with both probes in place, called P_{pr}. Finally, a measurement with both a long and short dielectric waveguide is performed, which can be used to calculate the losses of the waveguide with none of the coupling effects, refereed to as P_{WL} and P_{WS}, respectively. In this case, a waveguide length of 1 and 2 cm is used. A summary of these four measurements is shown in Figure 2.6.

Each of the above measurements is necessary in order to perform a series of calculations to determine the loss of the system coupled with the probes and a waveguide. Assuming the total loss of the system is only due to the loss in the probes, the loss in the waveguide, and the coupling loss, the total loss of the system can be written as:

$$L_t = L_{pr} + L_W W_l + L_{CL} \tag{2.1}$$

where L_t is the total loss, L_{pr} is the loss due to the two probes, L_W is the waveguide loss (in loss/distance), W_l is the waveguide length, and L_{CL} is the loss due to coupling. Since the measured power is in arbitrary units, the mentioned losses can only be found as a percentage of the total power. From the measurement setups shown in Figure 2.6, each loss can be determined from the relative power readings. The probe loss can be found from dividing the power with the probes in place by the total power, which is shown in equation 2.2.

$$L_{pr} = 1 - \frac{P_{pr}}{P_t} \tag{2.2}$$

This yields to two way probe loss, meaning that the loss due to each probe is actually half of L_{pr}. The loss due to the waveguide can be found by dividing the transmission through the 2 cm waveguide by the transmission through the 1 cm waveguide as follows.

$$L_W = 1 - \frac{P_{WL}}{P_{WS}} \tag{2.3}$$

This leaves the waveguide loss in per centimeter, as the difference between the waveguide lengths was 1 cm. The total loss in the system with both the waveguide and couplers in place can now be simplified, as the shorter waveguide is exactly 1 cm long. The total loss of the system is then P_{WS} divided by the total system power.

$$L_t = 1 - \frac{P_{WS}}{P_t} \tag{2.4}$$

The two-way coupling loss can then be found by substituting equations 2.2 - 2.4 back into equation 2.1 and solving for L_{CL}. Again, the corresponding one-way coupler loss can be found by dividing this value by two. Table 2.1 shows the various arbitrary power measurements and losses discussed above for 100, 200, and 300 GHz. Clearly, at the lower frequencies the total loss is relatively low, with only a 14 % loss due to two way coupling, and a low loss for both the probes and waveguide. However, as the frequency is increased, the

Table 2.1 Calculated values for waveguide coupling and probe loss.

f (GHz)	100	200	300
P_t	1x10^7	7.21746x10^7	5.12385x10^7
P_{pr}	7.96358x10^7	5.57332x10^7	3.75581x10^7
P_{WL}	4.42376x10^7	1.07248x10^7	1.21856x10^7
P_{WS}	5.63175x10^7	1.712496x10^7	2.07195x10^7
L_W	21.45 %	37.37 %	48.18 %
L_{pr}	20.36 %	22.78 %	26.70 %
L_{cl}	13.95 %	16.12 %	20.63 %

waveguide loss is greatly increased, but the coupling and probe loss are relatively stable. In this work, we are primarily interested in the coupling and probe loss, and not the waveguide loss, as only a simple dielectric ribbon waveguide was used in this work. It is also observed that all other losses not included in the waveguide and probes are essentially built into the coupling loss. These losses could include loss due to diffraction, misalignment, and many other factors. Therefore, the reported coupling loss is actually higher than the actual loss due to the waveguide coupling.

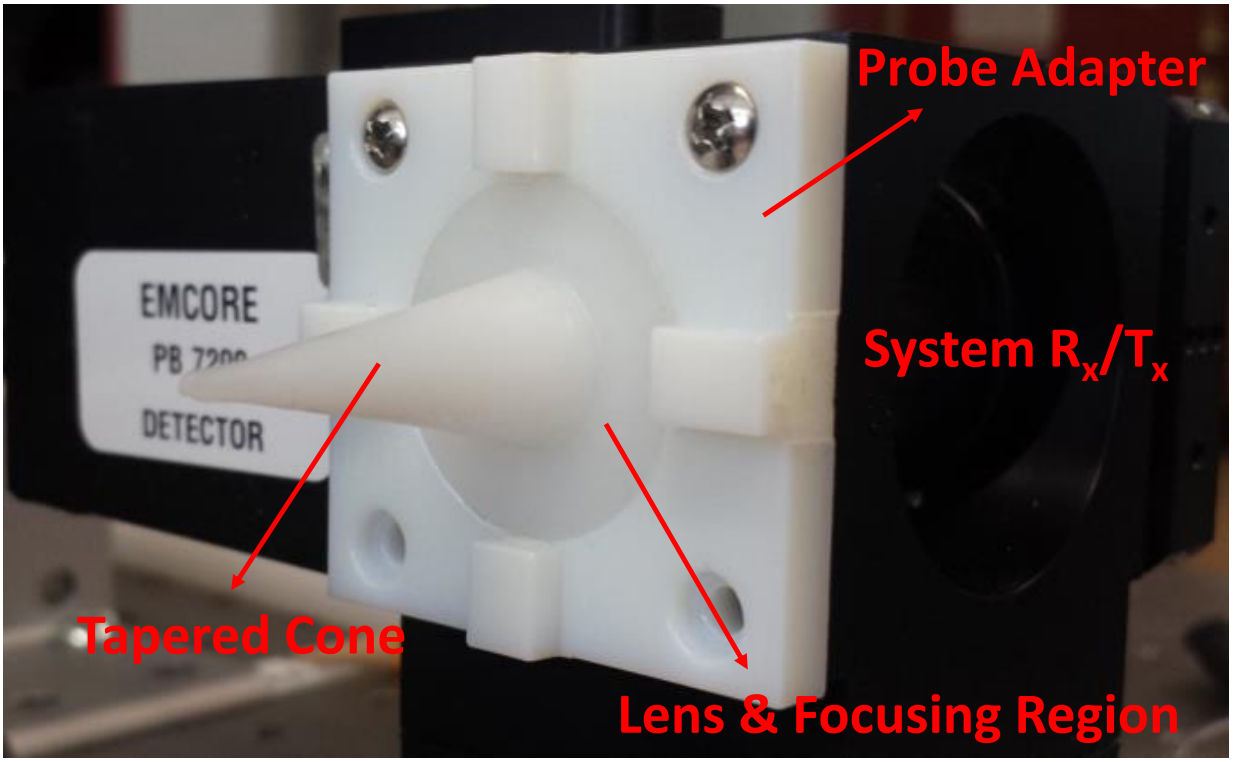

Figure 2.3 One fabricated probe placed in a Emcore THz system optical head.

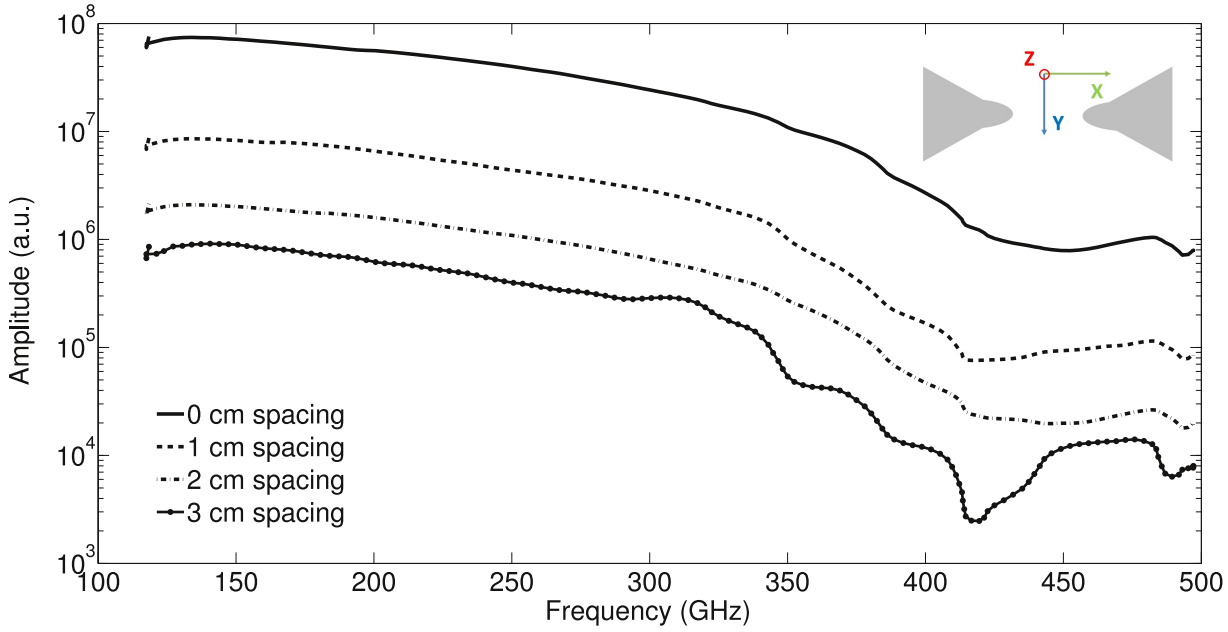

Figure 2.4 Transmission between each probe with increased probe spacing.

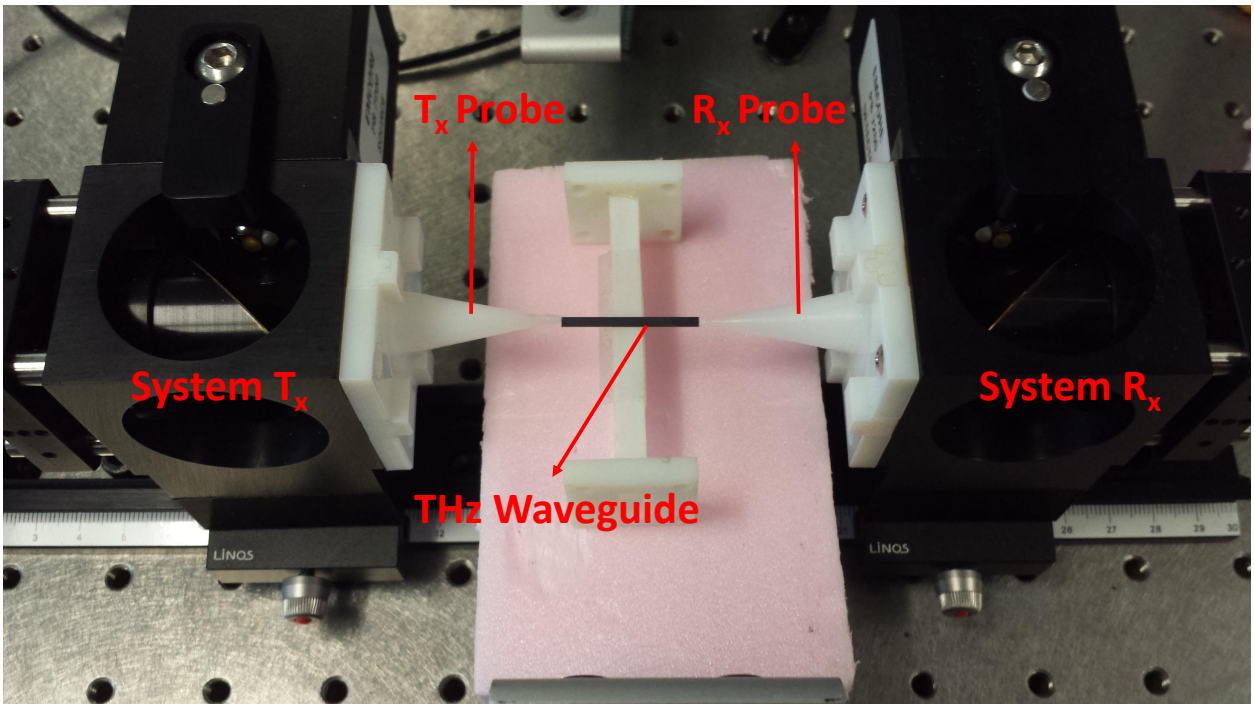

Figure 2.5 Waveguide measurement setup.

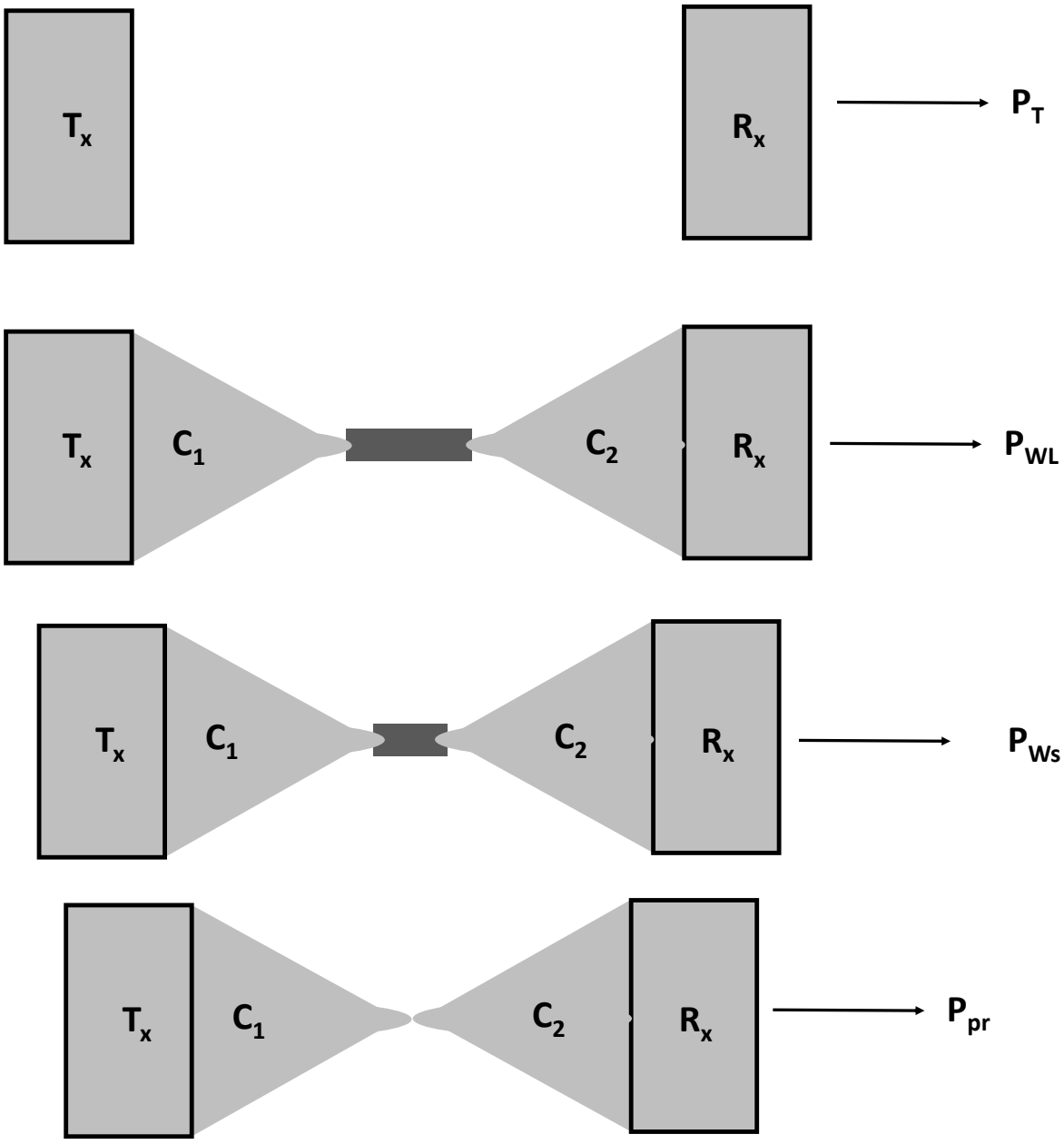

Figure 2.6 Summary of the required measurements for probe and coupling loss calculations.

2.2 Error Analysis and Discussion

For this method of coupling THz radiation between the commercial optical setup using dielectric focusing probes, some error will occur during the measurement. While there has been some discussion of THz measurement error [93], due to the complex setup of the measurement system and probes, some error is expected to occur. Many factors can contribute to this, beginning with the alignment of the focusing probes to the THz optics. For nearly every measurement, some alignment error is expected. The alignment of the probe tips with the measured device (in this case, the dielectric ribbon waveguide) is also difficult to quantify.

Additionally, the frequency domain test setup used in these experiments has some error within the system. This primarily comes from the heating and cooling of the laser, which controls what frequency the output THz radiation occurs. In this case, as the laser is heated, the frequency is increased, and as it is cooled, it is decreased. The problem occurs when multiple measurements are taken, the temperature of the laser will not be exactly the same as it was in the previous measurement, making the frequency not identical and introducing some error into the results. Overall, the expected error between measurements is likely to be no greater than 10 %, which is within the expectations set in the current literature.

2.3 Conclusions and Discussion

In conclusion, this chapter explored the development of an experimental method of coupling between commercial THz measurement systems and common THz waveguides using dielectric focusing probes. The probe behavior is validated both through FEM simulation as well as measurement. Overall, the method produces a one-way coupling loss into a dielectric ribbon waveguide as low as 7.2 %, and a two way coupling loss of 21 %. These values show relatively low loss coupling may be achieved even in the THz spectrum, with potential applications in nearly every passive THz system that requires waveguiding. This chapters work

will be used throughout the rest of this thesis when making THz measurements, especially for waveguiding applications.

CHAPTER 3

Dielectric Ridge Waveguides

3.1 Introduction and Proposed Geometry

A waveguide which is planar as well as directly compatible in on-wafer integration would be very desirable in the THz frequency spectrum. A possible method of guiding THz waves on wafer would be to directly fabricate the waveguide on the wafer itself. This can be accomplished with ridge or rib waveguides, which have been used extensively in the optical frequency spectrum, containing a bulk dielectric with a thin top layer ridge [83] - [86], show in in Figure 3.1. Typically made of glass or other dielectric materials, ridge waveguides do not require any of the dielectric layers to be much thinner than a wavelength. However, ridge waveguides have been little explored in the THz spectrum, outside of very specific applications, such as quantum cascade lasers [87] - [89]. In this chapter, ridge waveguides are evaluated through theoretical calculations, simulation, and measurement for their application as THz waveguides.

3.2 Theoretical Analysis

Unfortunately, the boundary conditions cannot be satisfied analytically for the ridge waveguide, meaning an analytical treatment of this problem is not possible. However, approx-

imate solutions for problems of this type have been well explore in the literature [90]-[91]. In this case, the effective index method (EIM) will be used to approximate the solutions of the ridge waveguide. The EIM has been widely explored in the optical region, however, there are certain assumptions that must be made before this method is applied. The bulk of the assumptions contained within the EIM method is that a two-dimensional structure must be approximated as a series of one-dimensional structures. In the optical spectrum, most of the explored structures are much larger than a wavelength, making this assumption valid. However, in the case of the ridge sizes that will be used in this analysis for the THz spectrum, the ridge dimensions are closer to the order of a wavelength.

Therefore, the EIM solution is only used to obtain a general understanding of the propagation characteristics of the waveguide. This includes the attenuation of the waveguide as well as the $\omega\beta$ propagation characteristics. Before the final conclusions are taken from the EIM solutions, these characteristics are first confirmed and compared to 3-D FEM simulation to ensure the assumptions contained within the EIM solution is still valid at these frequencies.

3.2.1 EIM Solution

The effective index solution method can be used to solve many dielectric-based waveguide problems. In this method, the proposed waveguide geometry is reduced to a number of 1-D dielectric slabs which can easily be analyzed using conventional methods. The effective refractive index (or dielectric constant) can be deduced from each 1-D waveguide from the propagation constant of the slab. Then, the effective parameters are used as parameters for a final 1-D slab which constitutes the effective system. In the case of the dielectric ridge waveguide, the geometry is broken down into 4 one-dimensional slabs. Two slabs correspond to the areas on the edge of the ridge, and one corresponds to the ridge itself. The effective indices of these three regions are then used to form a composite 1-D slab, which takes into account the width of the ridge. The overall process and geometry is summarized in Figure

3.2.

3.2.2 1-D Slab Analysis

In this section, the one-dimensional analysis of a slab waveguide is presented. The slab is made of a core and cladding section, with permittivity of ϵ_C and ϵ_{CL}, respectively. The slab has a thickness of h, with the origin placed at the center of the slab. Figure 3.3 shows the geometry of the 1-D dielectric slab. Assuming the slab is infinite in the y- and z-directions, with the wave propigation occurring in the z-direction, the dependance of the E and H fields in the y-direction is negligible ($d/dy = 0$). The wave equation in this case is then

$$(\nabla^2 + \omega^2\mu\epsilon)\vec{E} = 0 \tag{3.1}$$

for TE polarization, the electric field only has a y-component, leading to the following expression for the electric field.

$$\vec{E} = E_y(x, y, z)\hat{y} = E_y e^{-j\beta z}\hat{y} \tag{3.2}$$

The magnetic field is found through the Maxwell's equation

$$\nabla X\vec{E} = -j\omega\mu\vec{H} \tag{3.3}$$

$$\nabla X\vec{H} = j\omega\epsilon\vec{E} \tag{3.4}$$

which gives the following relation for the magnetic field.

$$\vec{H} = \frac{1}{\mu_0}(-j\beta E_y\hat{x} + \frac{dE_y}{dx}\hat{z})e^{-j\beta z} \tag{3.5}$$

By placing the origin at x = 0, the symmetry of the structure is exploited to find even and odd mode solutions for the fields.

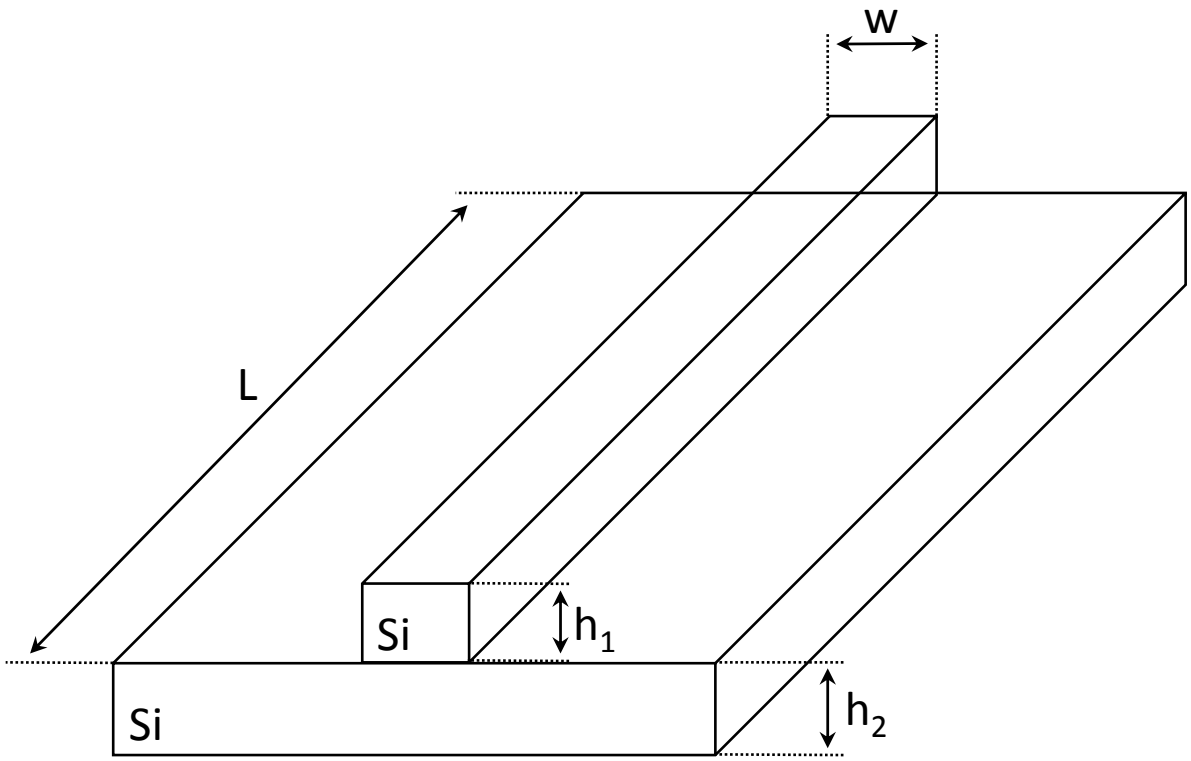

Figure 3.1 Proposed geometry of the dielectric ridge waveguide.

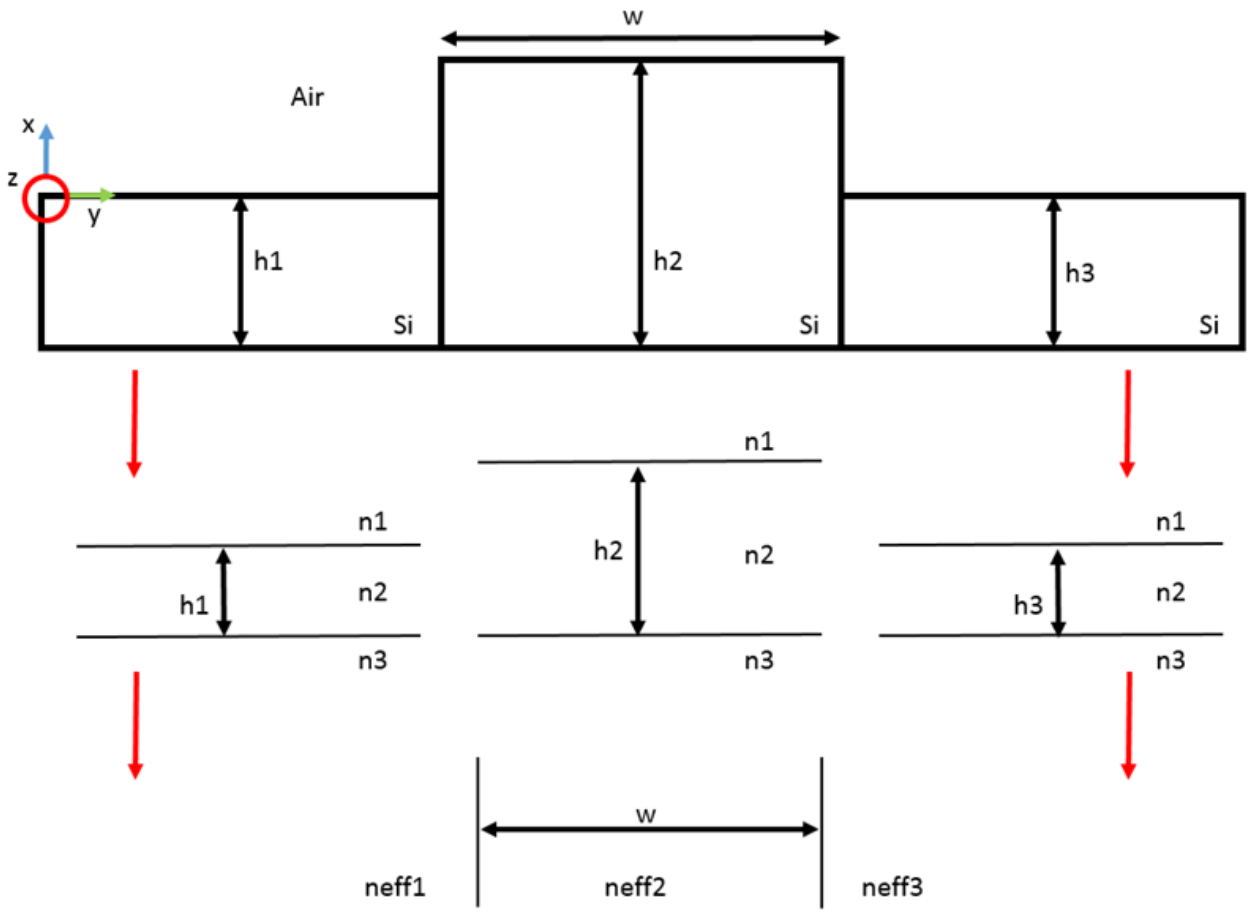

Figure 3.2 Effective index method.

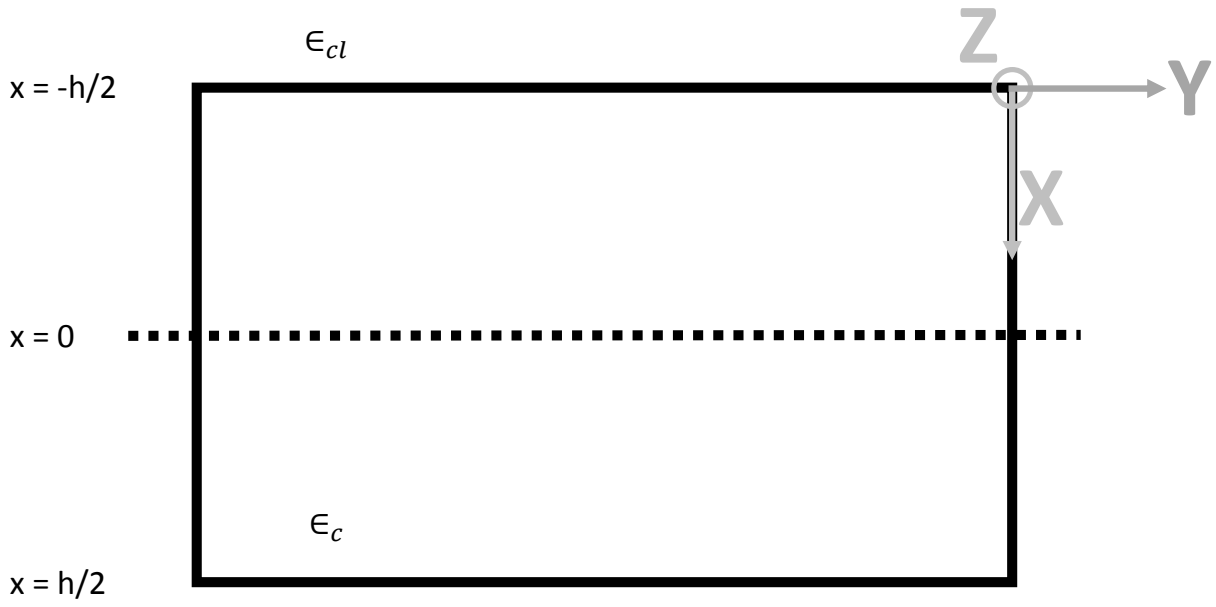

Figure 3.3 One-dimensional dielectric slab geometry.

3.2.2.1 TE Even Modes

The electric field for the TE even modes can be expressed as

$$E_y(x) = \begin{cases} C_0 e^{-\alpha y(x-h/2)}, & x \geq h/2 \\ C_1 \cos(\beta_y x), & h/2 \geq x \geq -h/2 \\ -C_0 e^{\alpha y(x+h/2)}, & x \leq -h/2 \end{cases} \tag{3.6}$$

where C_0 and C_1 are unknown constants. substituting these solutions back into equation 1, yields the following relation.

$$\beta_y^2 + \beta^2 = \omega^2 \mu_0 \epsilon_0 n_f^2 = \frac{\omega^2}{c^2} n_f^2 = k_0^2 n_f^2 \tag{3.7}$$

$$-\alpha_y^2 + \beta^2 = \omega^2 \mu_0 \epsilon_0 n_{cl}^2 = \frac{\omega^2}{c^2} n_{cl}^2 = k_0^2 n_{cl}^2 \tag{3.8}$$

Applying the boundary conditions on the edge of the slab (continuity of the E and H fields) yields

$$C_0 = C_1 \cos(\beta_y h/2) \tag{3.9}$$

$$\frac{\alpha_y}{\mu_0} C_0 = \frac{\beta_y}{\mu_0} C_1 \sin(\beta_y h/2) \tag{3.10}$$

setting these equations to zero yields a transcendental equation in terms of the propagation constant as follows.

$$\alpha_y = \beta_y \tan(\beta_y h/2) \tag{3.11}$$

3.2.2.2 TE Odd Modes

The electric field for the TE odd modes can be written as the following.

$$E_y(x) = \begin{cases} C_0 e^{-\alpha y(x-h/2)}, & x \geq h/2 \\ C_1 \sin(\beta_y x), & h/2 \geq x \geq -h/2 \\ -C_0 e^{\alpha y(x+h/2)}, & x \leq -h/2 \end{cases} \tag{3.12}$$

Applying the boundary conditions and eliminating for C_0 and C_1 yields a similar transcendental equation for the propagation constant as in the previous analysis, shown by the following.

$$\alpha_y = \beta_y \cot(\beta_y h/2) \tag{3.13}$$

3.2.2.3 Numerical Analysis

The propagation constants can now be found numerically, but first, if equation 6 and 7 are subtracted and multiplied by $(h/2)^2$, the following relationship is found.

$$(\beta_y h/2)^2 + (\alpha_y h/2)^2 = \omega^2 \mu_0 \epsilon_0 (n_f^2 - n_{cl}^2)(h/2)^2 = (k_0 h/2)^2 (n_f - n_{cl})^2 \tag{3.14}$$

This equation can be written in the form of a circle, with normalized coordinates $X = \beta_y h/2$, $Y = \alpha_y h/2$. Therefore,

$$(X)^2 + (Y)^2 == (k_0 h/2)^2 (n_f - n_{cl})^2 = R^2 \tag{3.15}$$

where $R = k_0 h/\sqrt{n_f^2 - n_{cl}^2}$. The intersection points between this circle and equations 12 and 10 will then give the propagation constants of the slab for TE odd and even modes, respectively.

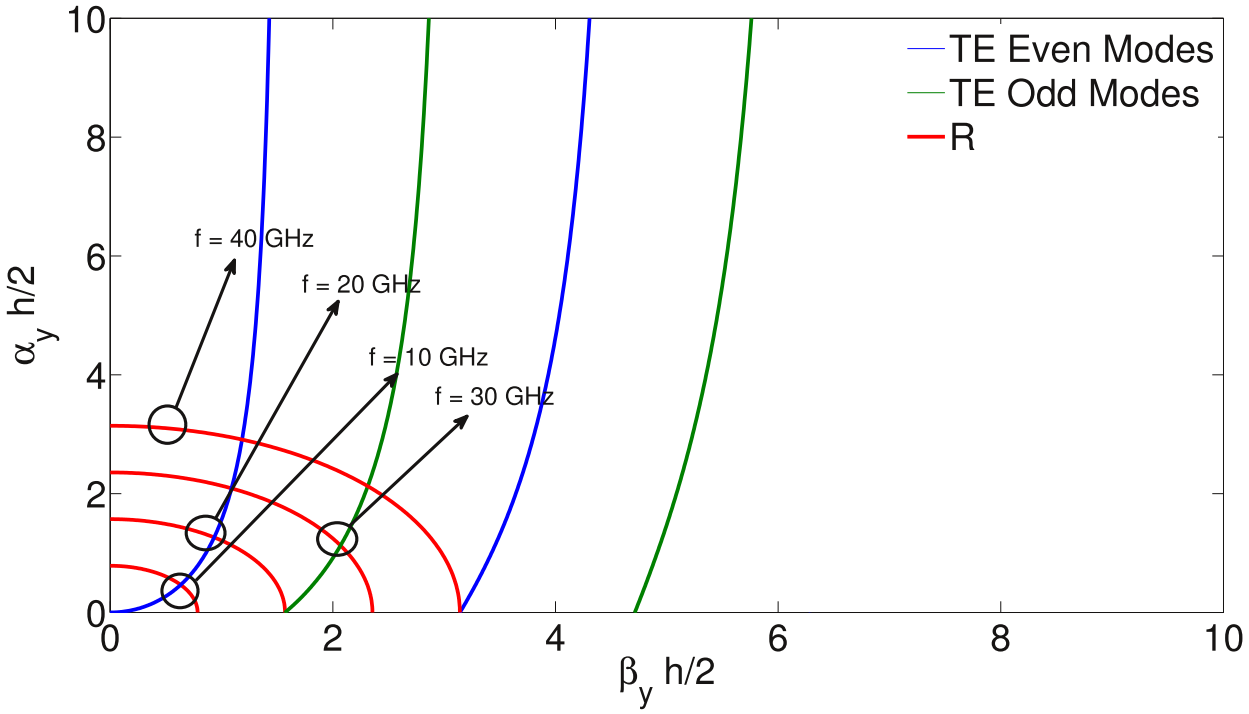

Figure 3.4 One-dimensional numerical slab solutions.

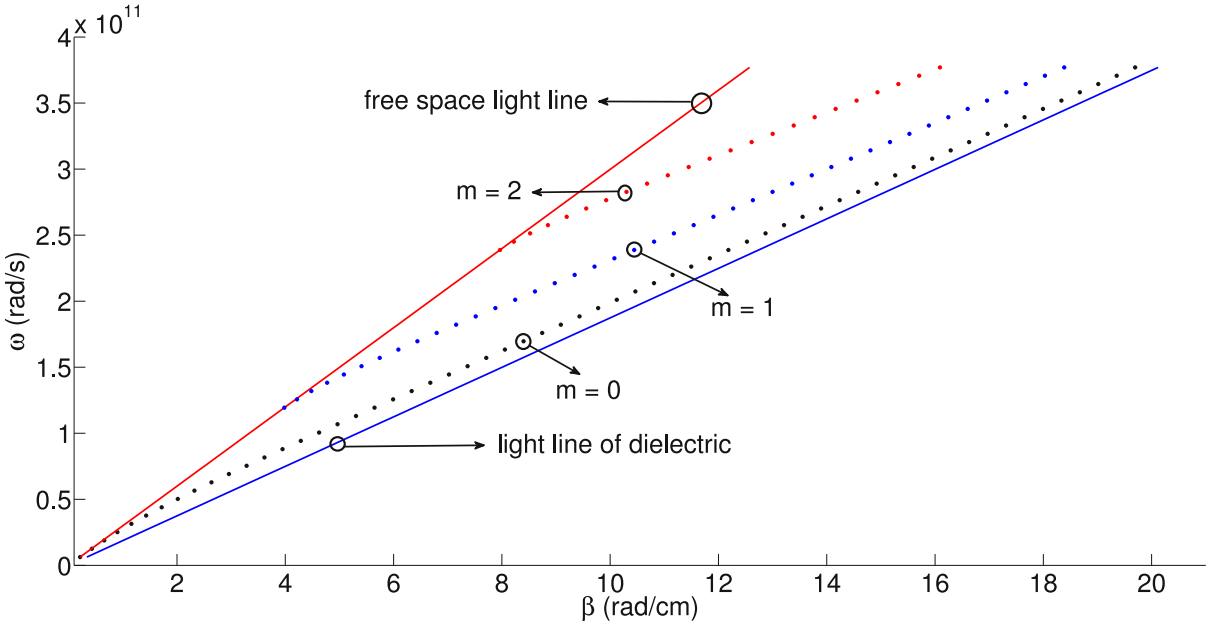

Figure 3.5 ω vs. β plot for varying modes in a one-dimensional slab

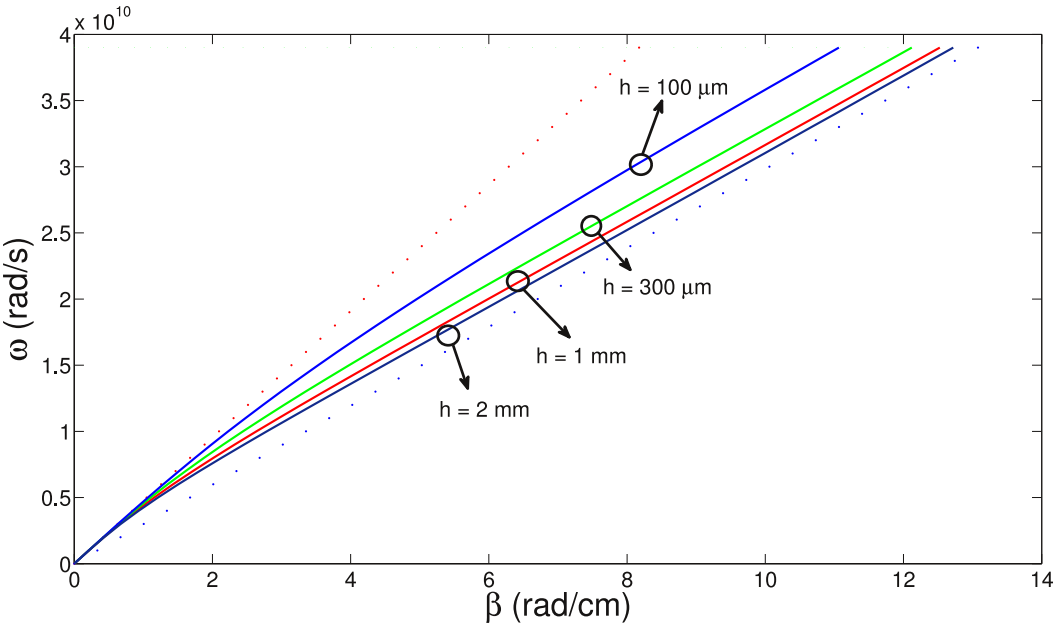

Figure 3.6 Effect of slab height on the propagation characteristics.

Figure 3.4 shows the graphical representation of the intersections between the above circle and the characteristic equations for the TE odd and even modes. For this slab, a slab thickness of $h = 3mm$, $\epsilon_c = 2.56$ and $\epsilon_{cl} = 1$ are used. Clearly, the intersection points vary depending on the input frequency. However, the same can be said when the thickness of the slab, or the permittivity of the slab or surrounding structure is changed. In addition, the modes excited within the slab will vary depending on the same parameters. In this case, at the highest frequency (40 GHz) only the $m = 0$ and $m = 1$ modes are excited.

With this graphical solution, the propagation and attenuation constants are solved for in the y-direction. However, the propagation in the z-direction is desired. Using a simple dispersion relation

$$\beta_z^2 = \beta_C^2 - \beta_y^2 = \omega^2 \epsilon_C \mu_C - \beta_z^2 \tag{3.16}$$

or in terms of the attenuation constant

$$\beta_z^2 = \alpha_y^2 + \beta_0^2 = \alpha_y^2 + \omega^2 \mu_0 \epsilon_0 \tag{3.17}$$

where β_C is the propagation constant in the dielectric region. Using the data from the graphical intersections and equation 15, the propagation constant in the z-direction for a 1-D slab can be found. Using these value, the propagation characteristics of the slab can be deduced in the form of an ω vs β plot. Figure 3.5 shows such a plot for a slab with a thickness of $4mm$, $\epsilon_C = 2.56$, and $\epsilon_{CL} = 1$. The propagation within the slab is contained within two light lines, one representing a wave propagating in free space, as well as another representing a wave propagating in a uniform material of the same permittivity of the slab. The propagation characteristics of each mode show that the wave is first confined closely to free space propagation, but as the frequency is increased the propagation constants slowly converge to that of the slab.

These characteristics intuitively make sense, as when the frequency is increased, the

wavelength will decrease, causing less of the wave to propagate in the cladding regions. Changing the thickness of the slab provides a change in the propagation characteristics of the ω vs β plot. Figure 3.6 shows the ω vs β plot with varying slab thickness. In this case, the slab is varied between $100\mu m$ and 2 mm. As the slab thickness is increased, the propagation characteristics converge to that of the uniform slab of dielectric constant ϵ_C more quickly.

3.2.3 Composite Ridge Analysis

3.2.3.1 Lossless Ridge Analysis

In this section, the above 1-D analysis is used to analyze a ridge waveguide made of 4 composite 1-D slabs using the EIM. In this case, each slab is made of a lossless material with a relative permittivity of 11.9 (similar to silicon). Similar to the previous section, ω vs β plots are derived for various parameters of the waveguide. In this case, there are three primary geometrical parameters describing the rib (and each slab). Referring to Figure 3.2, the height of the ridge, h_1, the height of the edge h_2, and the width of the ridge, W.

Figure 3.7 shows the propagation characteristics of a lossless ridge waveguide with varying ridge width up to 300 GHz. In this case, the light lines now correspond to the propagation characteristics of the slabs which represent the edge regions of the ridge, as well as the ridge itself. Clearly, as the frequency is increased, the propagation characteristics converge to that of the ridge portion of the waveguide. Figure 3.7 also shows the effects of changing the width of the ridge. As one would expect, if the ridge width is increased, more of the wave propagation is contained within the ridge, causing convergence to the light line of the ridge to be at lower frequencies.

A similar effect is shown in Figure 3.8 for varying ridge heights. However, no light lines are displayed as they would change with each different ridge height. Again, the propagation constant increases more quickly with frequency as the ridge height is increased. While this

analysis is useful for visualizing the propagating modes in the ridge waveguide, in real-world materials there will be loss, and the propagation constant will no longer be purely real. In this case, the imaginary portion of the propagation constant will be due to the attenuation of the waveguide.

3.2.3.2 Lossy Ridge Analysis

In this section, the effects of using a complex permittivity to represent portions of the ridge waveguide are investigated. When introducing a complex value into the above analysis, a graphical method of solving for the propagation constant is no longer feasible.

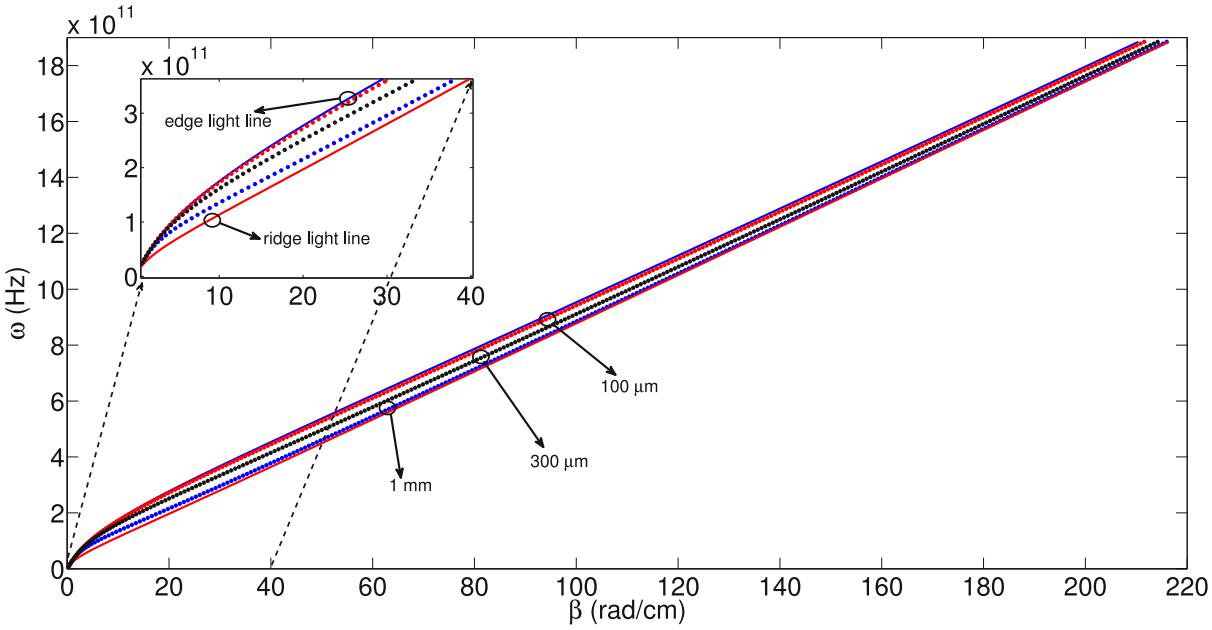

Figure 3.7 Effects of varying ridge width on the propagation characteristics of the ridge waveguide.

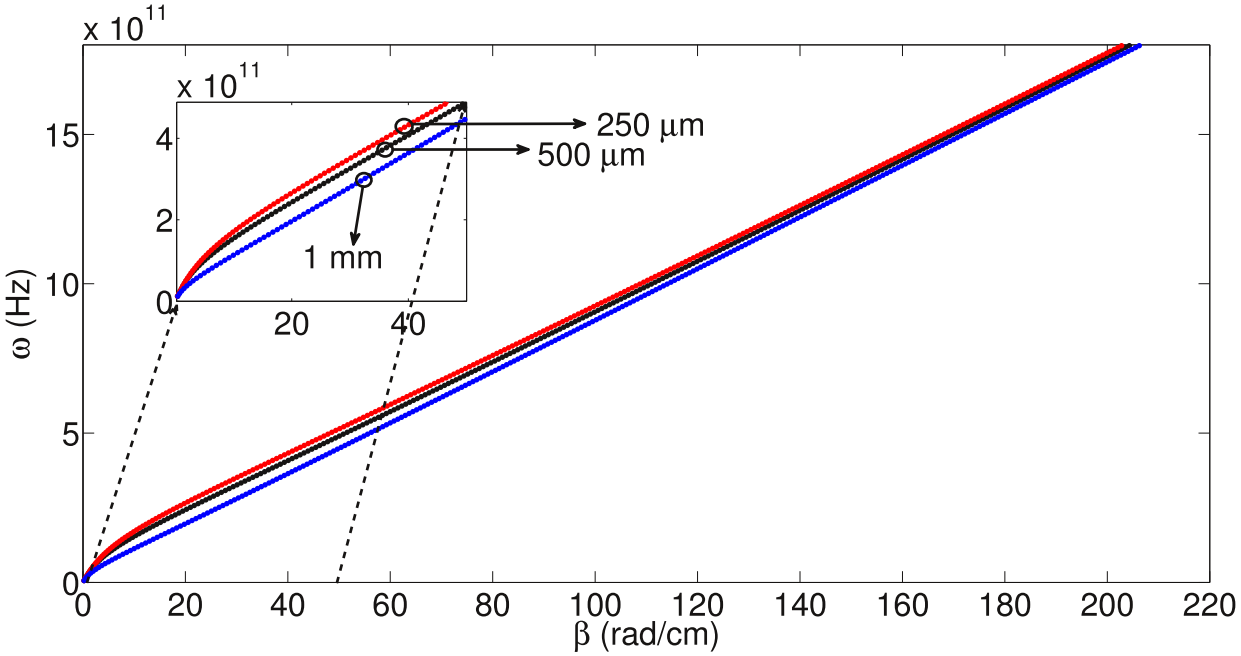

Figure 3.8 Effects of varying ridge height on the propagation characteristics of the ridge waveguide.

Therefore, a root solving algorithm which can solve for complex roots must be used. In this case, a simple newtons method is used. Each slab is modeled with typical properties of silicon, including $\epsilon_r = 11.9 + j.07$. Each slab is first solved graphically for the lossless case a the lowest frequency of interest, which is then used as an initial guess for the newtons method.

Figure 3.9 shows the attenuation of a ridge waveguide with $h_1 = 300\mu m$, $h_2 = 200\mu m$, and a width of $400\mu m$. As would be expected, the attenuation of the ridge is increasing with frequency. At 250 GHz, the waveguide has an attenuation of approximately .5 dB/mm.

The same analysis is performed, but with varying ridge height and width, at 250 GHz. The attenuation due to these parameters is shown in Figures 3.10 and 3.11. Clearly, the attenuation is increased when the ridge parameters (width and height) are also increased. This intuitively makes sense, as if the area of the lossy material is increased, more of the propagating wave will attenuate through it. Mathematically, equation 14 shows that the radius of the intersecting circle is directly proportional to the height of the slab, as well as the permittivity of the cladding and core layers. Therefore, if one of these permittivites is complex, when the height of the slab is increased the imaginary portion will be increased, leading to a higher attenuation. Figure 3.13 also shows the attenuation characteristics for both increasing ridge width and height at 300 GHz.

To confirm these assumptions, a similar analysis is performed with just one of the ridge regions modeled as lossless. In this case, the slab representing the ridge height is modeled as a lossless material, while the other slabs are still lossy with the same parameters mentioned above. Figure 3.12 shows the effect of changing the ridge height in the lossless region on the overall attenuation of the ridge waveguide. Now, when the lossless region is increased, the overall attenuation is decreased. This confirms the above assumptions, and validates that if a lossy material is increased, the overall attenuation will also be increased.

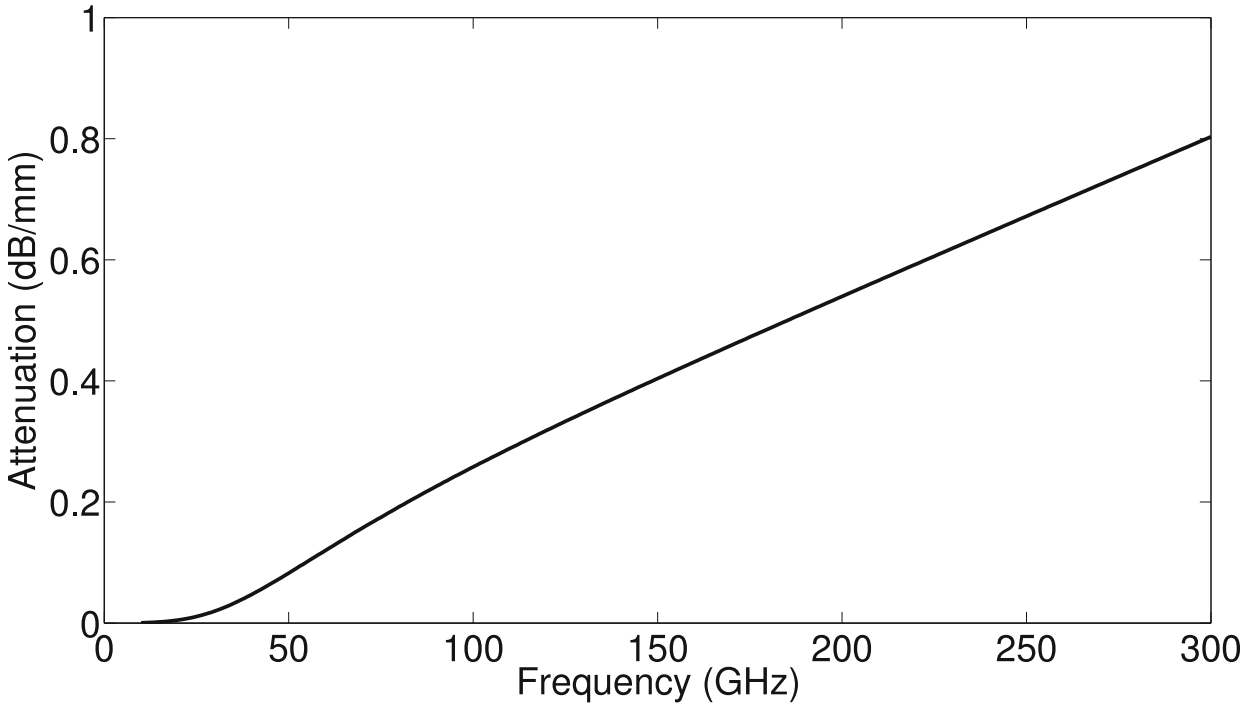

Figure 3.9 Theoretical attenuation of ridge waveguide versus frequency.

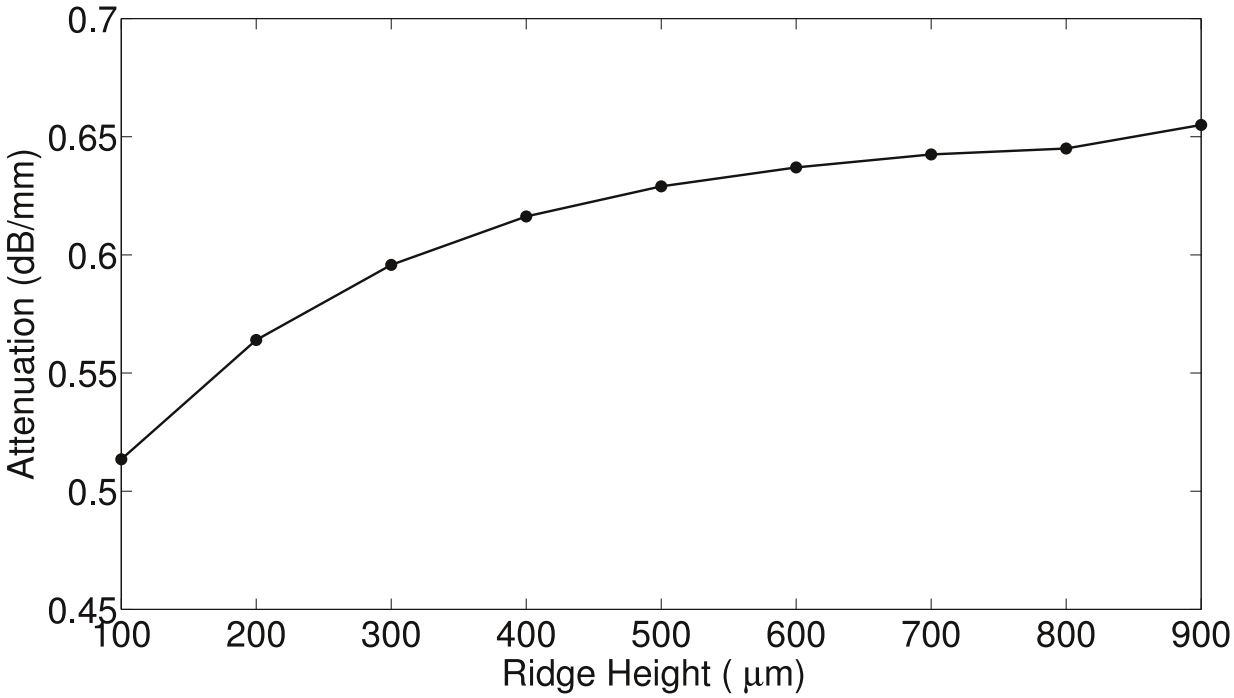

Figure 3.10 Theoretical attenuation of ridge waveguide at 250 GHz with varying ridge height.

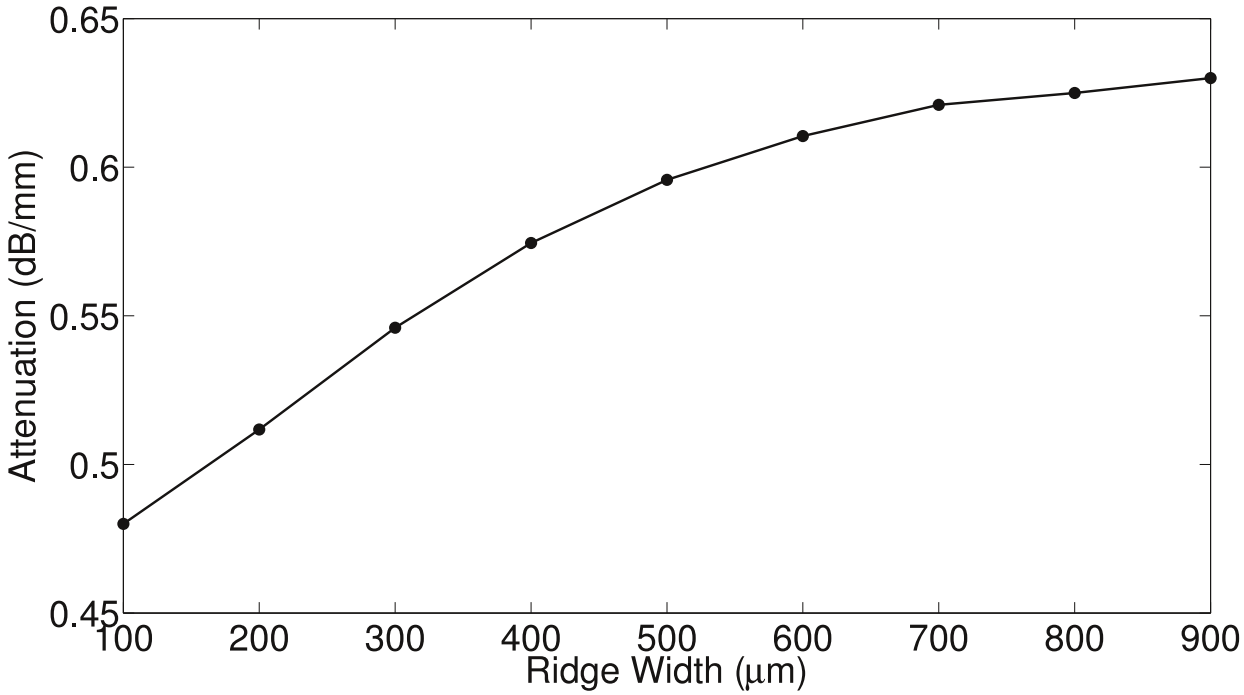

Figure 3.11 Theoretical attenuation of ridge waveguide at 250 GHz with varying ridge width.

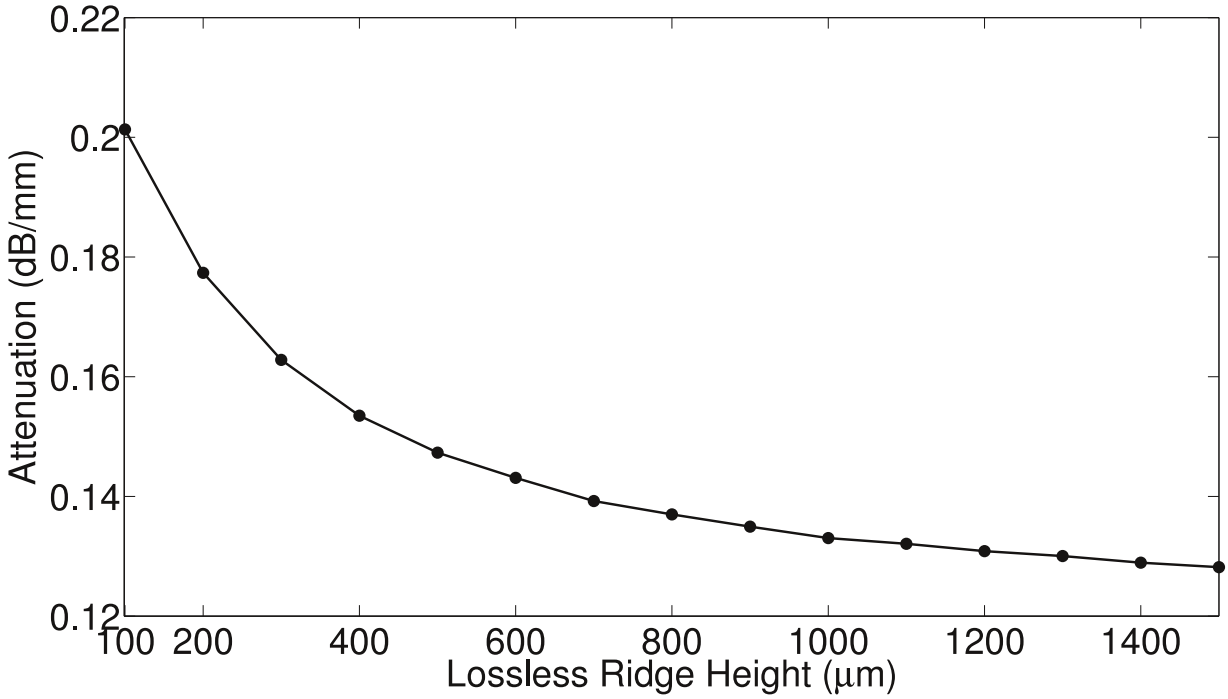

Figure 3.12 Effects of changing lossless ridge height on attenuation of the waveguide.

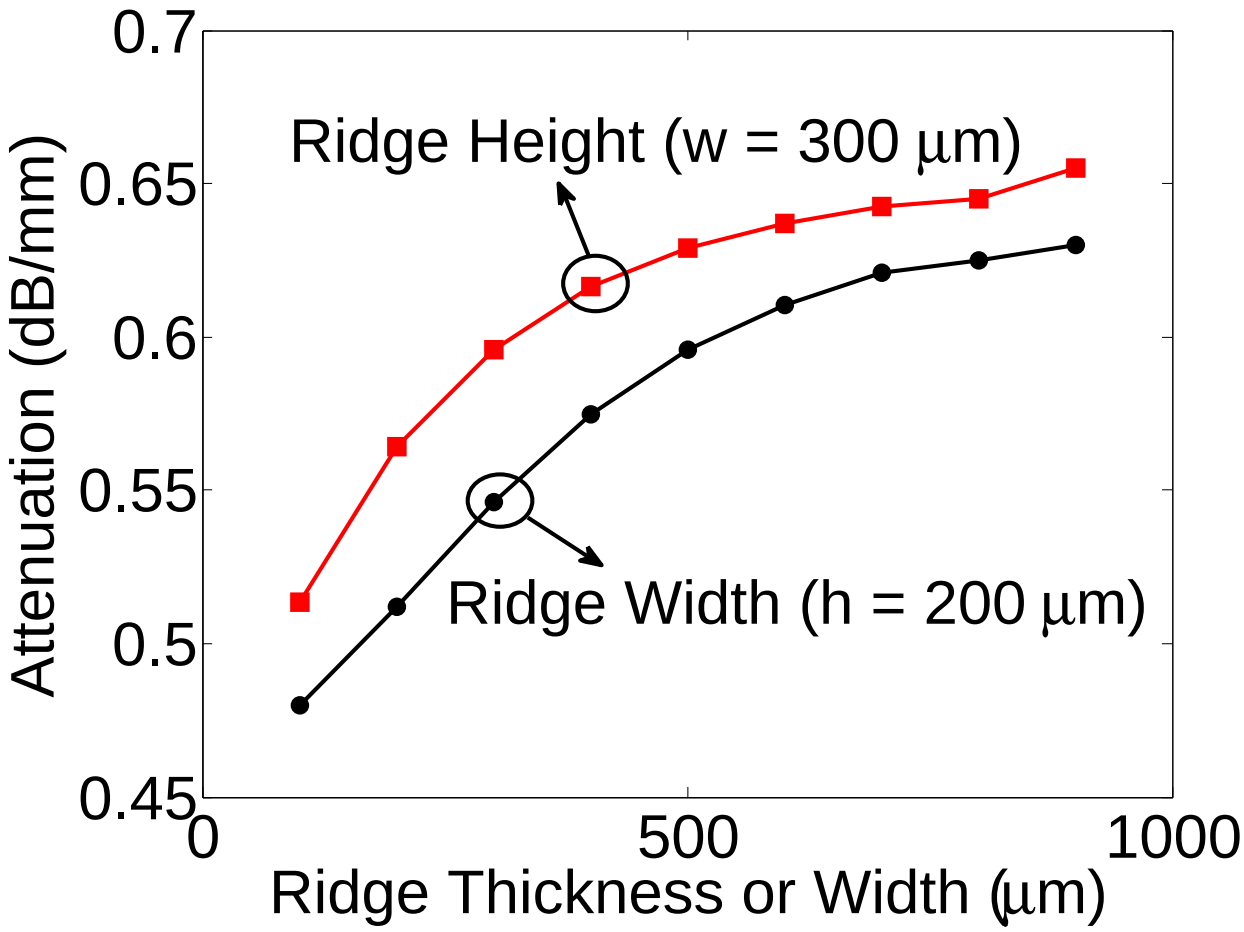

Figure 3.13 Theoretical attenuation at 300 GHz of silicon ridge waveguide with various ridge height and widths.

3.3 FEM Modeling

Three-dimensional FEM modeling is also used to analyze the waveguides and confirm the theoretical results. In this case, the commercial FEM modeler ANSYS HFSS 13.0 is used. Again, silicon is used as the material for the base dielectric and the ridge, with the same electrical properties as used in the theoretical analysis. First, the field profiles inside the ridge waveguides are investigated. The fields inside the ridge are sampled on a vertical plane placed inside the waveguide.

The fields inside the waveguide for three separate cases are shown in Figures 3.14 - 3.16. Figure 3.14 shows the effect of changing the height of the ridge, while keeping the base and ridge width constant. As the height of the ridge is increased, the field is more confined within the ridge, and the field spread within the base dielectric region is also decreased, the latter effect is observed especially near the edges of the ridge, as the height is increased. Figure 3.15 shows the effect of increasing the ridge width on the field contained within the waveguide. Similar to increasing the ridge height, increasing the width also increases the field concentration in the ridge. However, in some cases, more of the field is spread to the base dielectric layer. Finally, Figure 3.16 shows the effect of increasing the dielectric base height. These results show it is important that the dielectric base height is not too thin, as fields can easily leak out of the base. If the thickness is large enough the field is more confined towards the center of the ridge/base region. Overall, there is a great effect on the field confinement within the waveguide based on the dimensions chosen for the ridge.

As shown in the field profiles, some amount of power will leak out of the waveguide as there are no metallic boundaries. The amount of power leaked from the ridge can be calculated from the FEM simulations by calculating the average power in two regions. First, the field is integrated over the region corresponding to the area of the ridge. Next, the field in the area surrounding the ridge is integrated to find the total power in the ridge and the surrounding area. Subtracting these two averaged powers leaves just the power in the

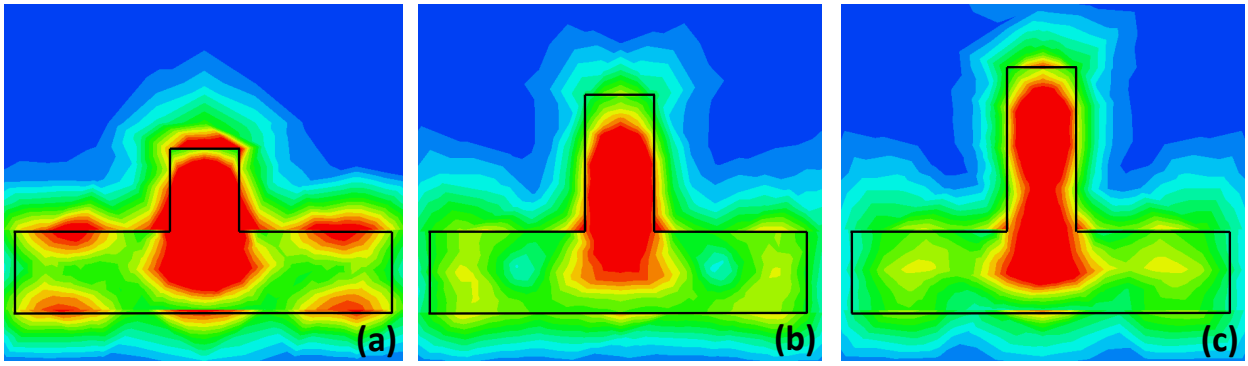

Figure 3.14 Field profile in ridge waveguide with varying ridge height at 300 GHz.

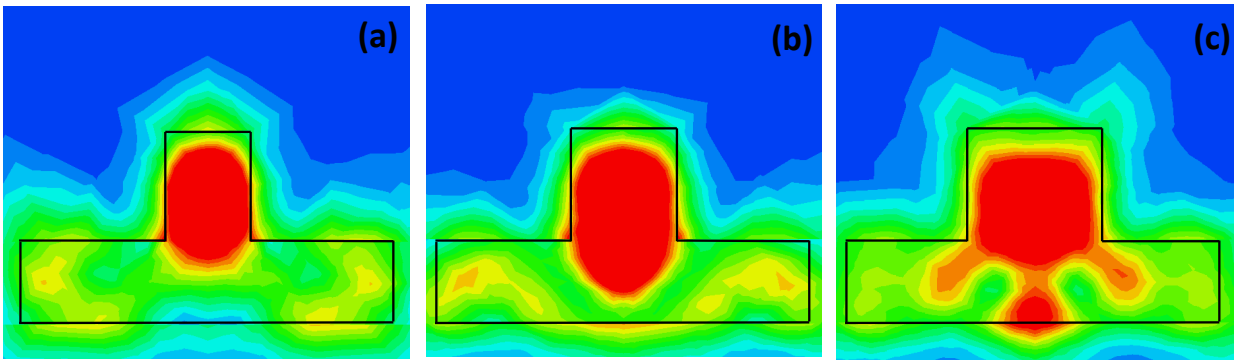

Figure 3.15 Field profile in ridge waveguide with varying ridge width at 300 GHz.

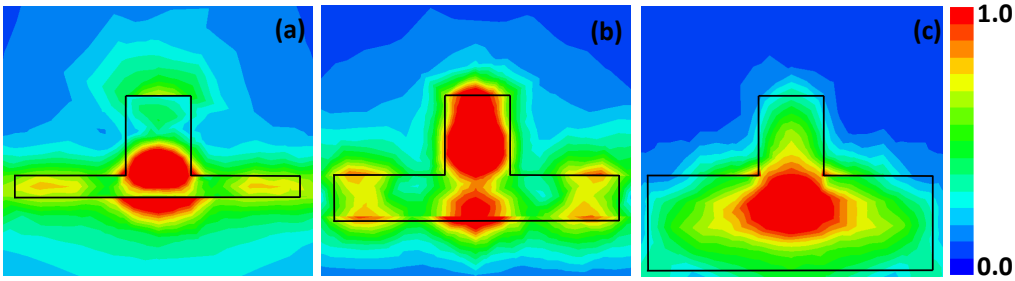

Figure 3.16 Field profile in ridge waveguide with varying dielectric base height at 300 GHz.

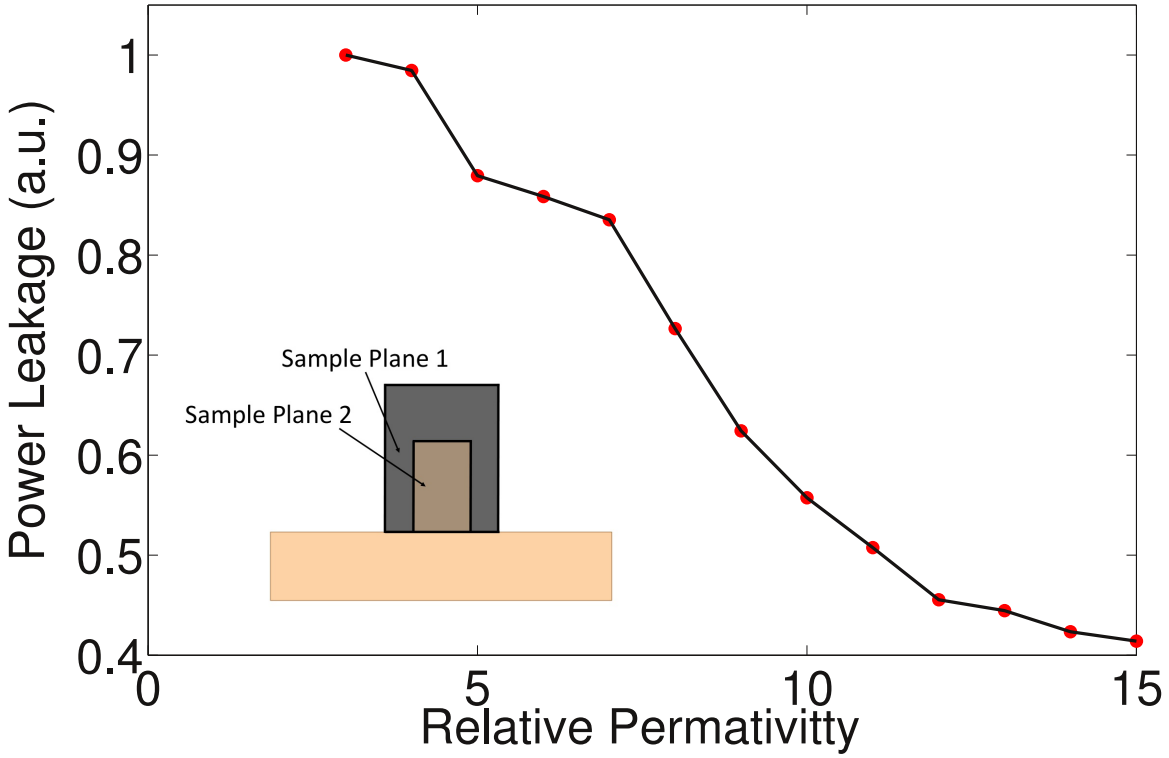

Figure 3.17 Percent of total power leaked from ridge as a function of the permittivity of the ridge at 300 GHz.

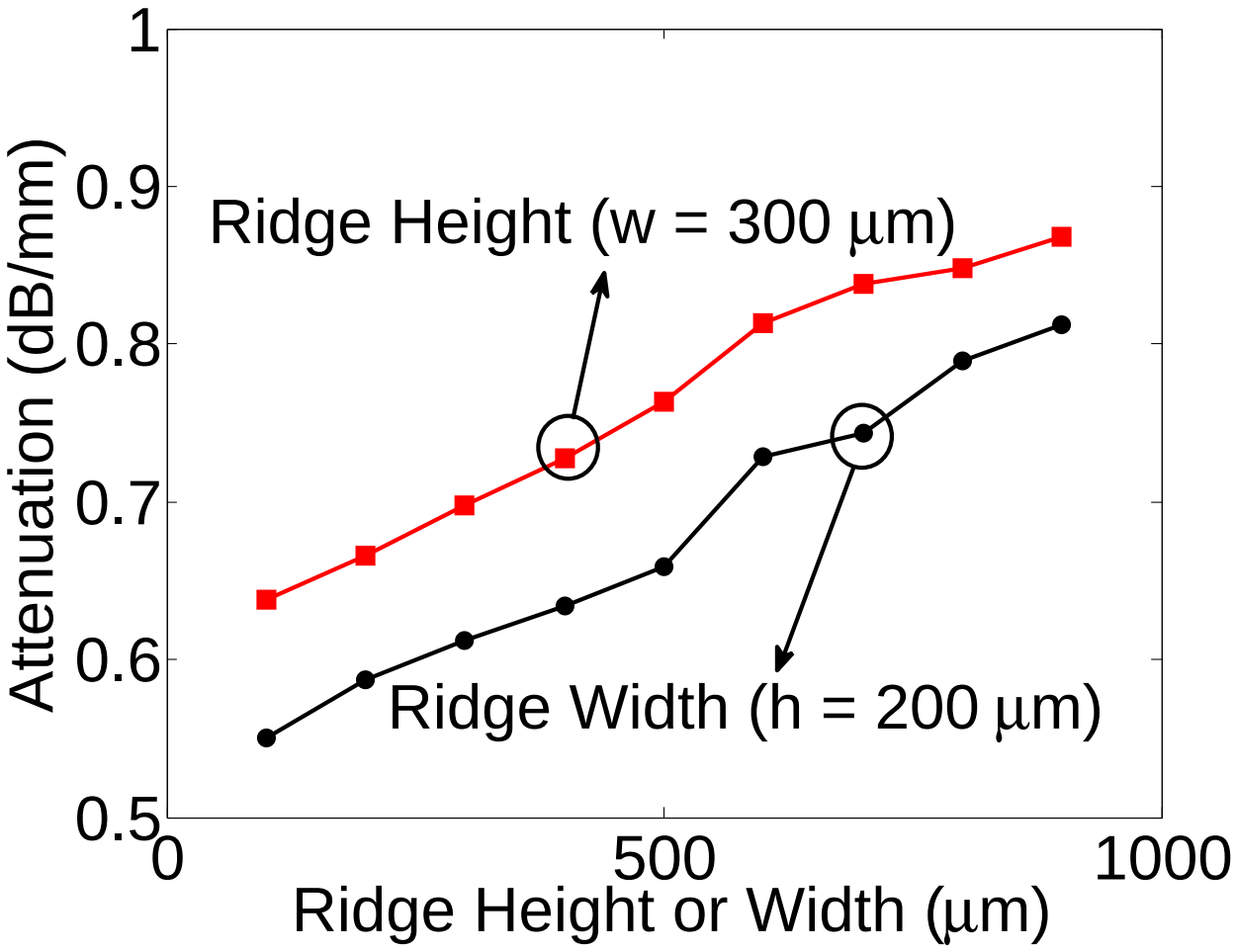

Figure 3.18 Simulated attenuation of ridge waveguide at 300 GHz for varying ridge height and widths.

surrounding area, this is summarized in the inset of Figure 3.17. The effect of changing the dielectric constant of the waveguide on the power leaked from the waveguide is shown in Figure 3.17. Clearly, when the dielectric constant of the waveguide is increased, the power that is leaked outside of the waveguide is decreased. Therefore, a dielectric material with a high dielectric constant, such as silicon, is ideal to construct these waveguides and reduce the power radiated.

The attenuation of the waveguides can also be found through simulation. This is accomplished by calculating the transmission properties for waveguides of two different lengths and subtracting the results. This leaves just the attenuation through the waveguide, as any coupling losses are removed. Figure 3.18 shows the simulated attenuation with various ridge heights and widths, with a constant base height. The simulated attenuation matches relatively well with the theoretical results, with the attenuation increasing with increased ridge height and widths. In the simulated case, due to the three-dimensional nature of the simulations, the attenuation is slightly higher than in the theoretical investigation.

3.3.1 Curves and Passive Circuits

Overall, the ridge waveguides show relatively low-loss propagation over 300 GHz. However, while the attenuation of the waveguide is comparable to other THz dielectric waveguides, due to the extra ridge area, these waveguides display slightly higher losses. While the ridge waveguides display larger attenuation, they have other advantages over typical dielectric waveguides (such as the dielectric ribbon waveguide). Outside of the integration compatibility advantages, these waveguides also have many applications in complex curved structures that would be difficult to realize using other dielectric waveguides.

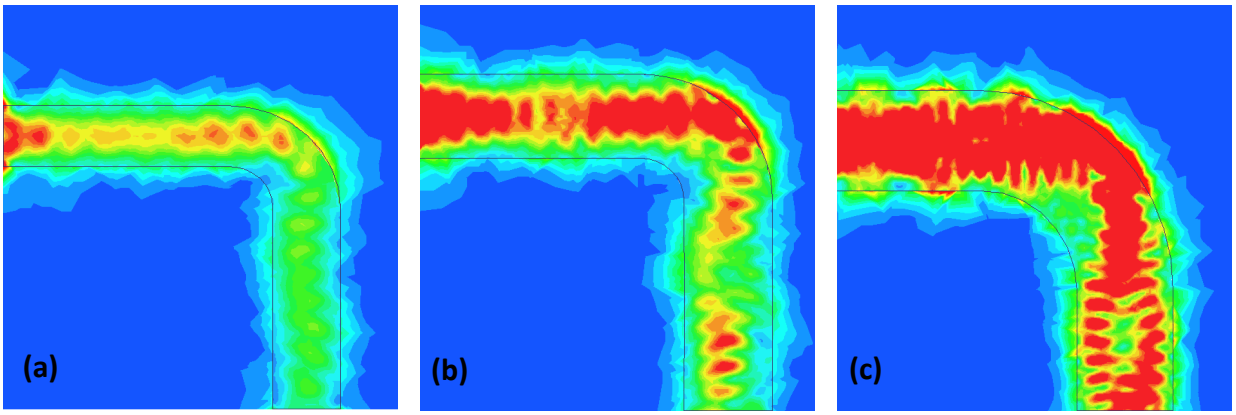

Figure 3.19 Field profile in ridge waveguide curves with varying ridge width at 300 GHz.

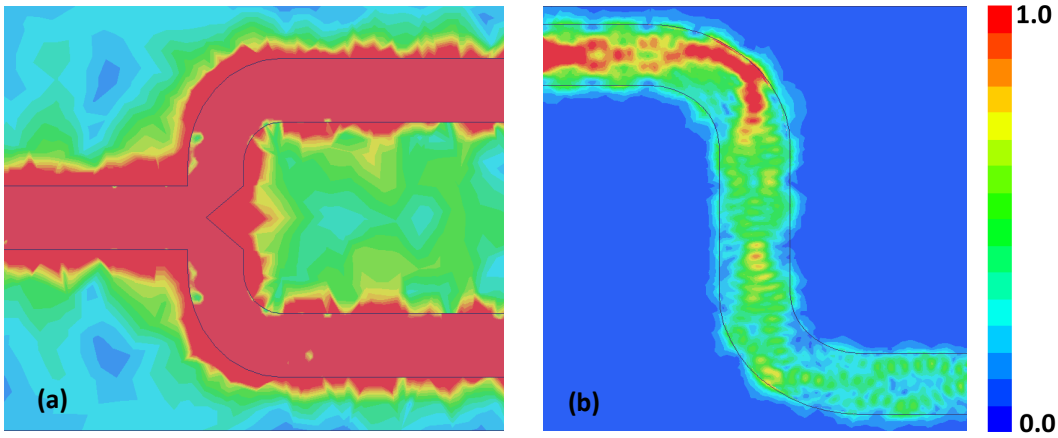

Figure 3.20 Field profiles of complex ridge waveguide geometries at 300 GHz.

As mentioned in the previous section, the width and height of the ridges impact the attenuation of the waveguide. If the ridge is too narrow near the bend of a curve the power is radiated, as displayed in Figure 3.19, where the field on a curve made from a ridge waveguide is shown with varying ridge widths. Clearly, as the ridge width is increased, more of the power is accepted into the ridge, with less radiated at the bend. Therefore, for curved wave guiding applications, there is a tradeoff between the increased attenuation of the waveguide due to a wider ridge and the field being more confined within the ridge.

In addition to simple curves, other more complex structures can be implemented with the ridge waveguides. Figure 3.20 shows field samples of two more complex structures, a power splitter and a multi-curve structure. For the power splitter, the field is well contained within the center portion, and the field is approximately split between the two branches as would be expected. Additionally, the multi-curve structure shows that while some power is lost in the first bend, the signal is still efficiently transmitted.

3.4 Fabrication and Measured Results

Several silicon-based ridge waveguides were fabricated, with different height and widths. In this case, the silicon ridge waveguides were fabricated using n-type single side polished silicon wafers with resistivity of approximately $100\Omega cm$, and a total wafer thickness of $500\mu m$. The waveguides were fabricated using a standard optical lithography and wet etching process.

The silicon wafer was first prepared by removing the native oxide using a buffered hydrofluoric acid (HF) solution. A titanium film of proximately $2\mu m$ was then deposited on the front and back side of the silicon wafer using e-beam evaporation. Here, the titanium film was used as the mask for deep anisotropic etching of the silicon wafer due to its excellent adhesion properties. This is followed by patterning and etching of the top titanium layer on the polished side of the wafer using HF: H_2O_2: H_2O = 1:1:100, while protecting the titanium film on back side with photoresist. Next, the etching of the silicon was performed

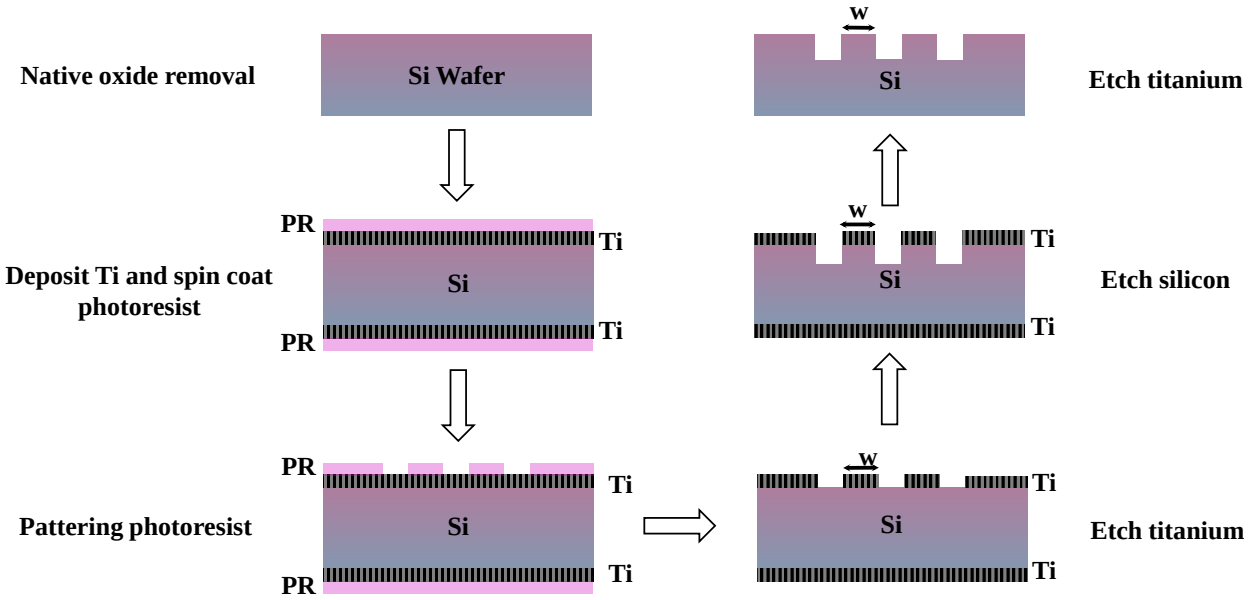

Figure 3.21 Fabrication process for the silicon ridge waveguide.

using a 30% Potassium Hydroxide (KOH) solution at $75^{\circ}C$ for 1 hour for a ridge height of approximately $50\mu m$. Finally, the titanium film was removed using HF: H_2O_2 :H_2O = 1:1:100 to reveal the ridge structures within the silicon. The overall fabrication process is summarized in Figure 3.21. For a ridge waveguide with a larger height, SiO_2 deposited using plasma enhanced chemical vapor deposition (PECVD) was used as a hard mask, with patterning achieved using a buffered oxide etchant (BOE 6:1). Figure 3.22 shows SEM image of one of the silicon ridges under magnification. A ridge is clearly developed within the silicon, although the ridge does not have a clean vertical wall due to the etching process. Therefore, two separate widths are associated with the ridge.

The ridge waveguides are measured using a quasi-optical THz measurement setup. The THz signal is generated using a Emcore PB-7200 commercial frequency domain test system. This system is made up of receiver (Rx) and transmitter (Tx) heads that are interfaced with sources through fiber-optics. The system is capable of measuring transmission between the Rx and Tx heads from 100 GHz to 2 THz, with a frequency resolution of 100 MHz. The ridge waveguide samples are interrogated with dielectric focusing probes made of HDPE introduced in chapter two, that are designed to operate up to 500 GHz. A metallic window is also placed on the back end of the Rx probe so that any excess probe-to-probe coupling is reduced. Figure 5.22 shows the overall measurement setup.

To measure a sample with the above setup, a reference measurement is required. For the ridge waveguide samples, a reference was taken by de-coupling the probes form the silicon wafer by a small distance such that no signal is transmitted into the silicon. Water, a strong absorber of THz, is also placed on the surface of the waveguide to further ensure that no signal is transmitted during the reference measurement.

Figure 3.22 SEM photography of a fabricated ridge waveguide.

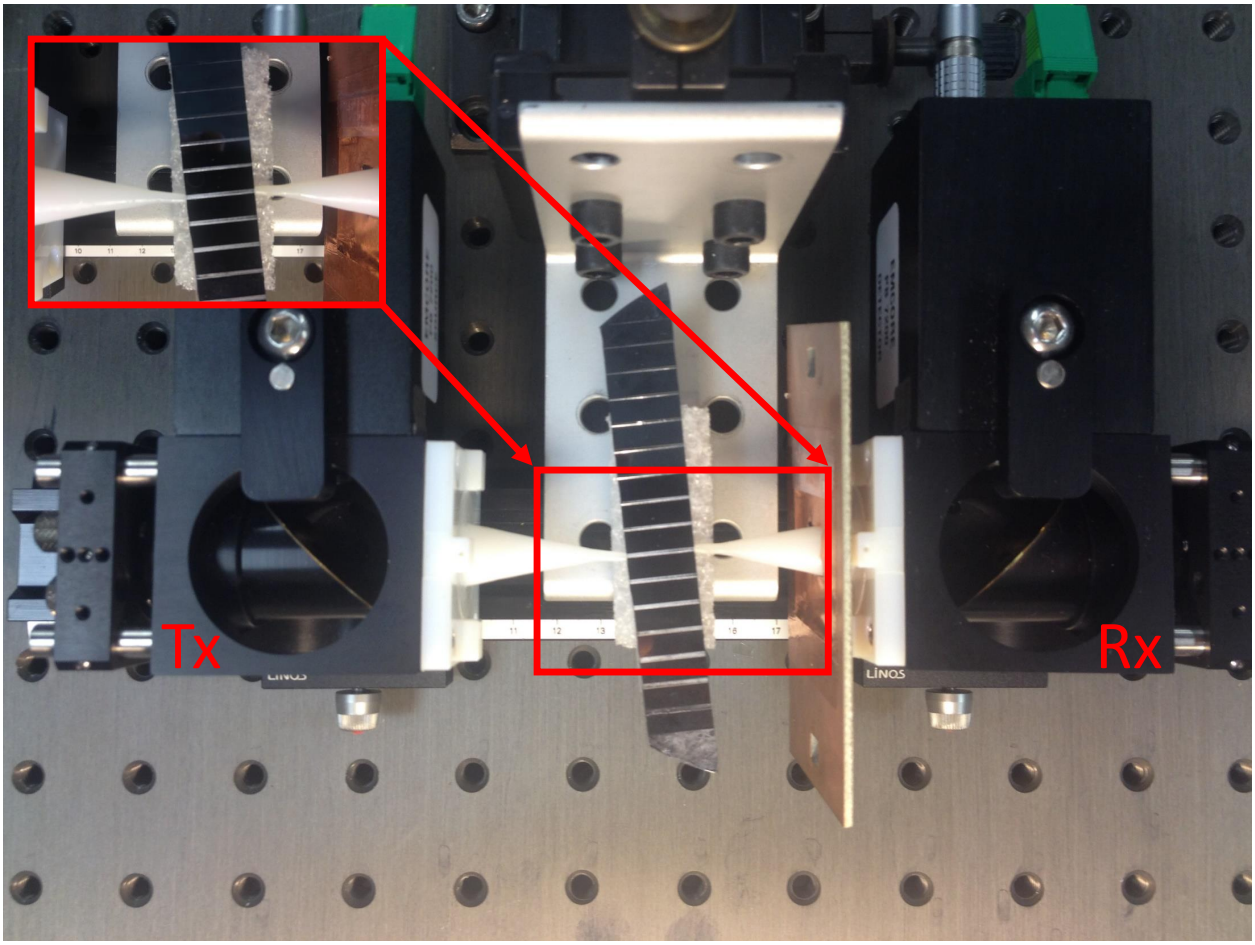

Figure 3.23 THz measurement setup for silicon ridge waveguides.

Multiple ridge heights and widths were etched onto silicon wafers to be measured. For this work, two different ridge widths are measured each having two separate heights. The two ridge heights used in this case are approximately $H_1 = 40\mu m$ and $H_2 = 80\mu m$. The two sample ridge widths are $W_1 = 460\mu m$, and $W_2 = 750\mu m$. Figures 3.24 and 3.25 show the transmission between four different ridge waveguides with different ridge height and width combinations. The waveguides have a wide transmission spectra, from 100 to 500 GHz. Additionally, as expected from the theoretical and simulation results, the waveguides with the thinner ridges display the least amount of loss.

The measured attenuation of the waveguides is also calculated by using two separate length waveguides with the same ridge width and height. The transmission of both waveguides is then subtracted and converted to an attenuation in units of dB/mm. The measured attenuation of the waveguide is shown in Figure 3.26. Here, the attenuation of four waveguides corresponding to ridge heights of H_1 and H_2, as well as ridge widths of W_1 and W_2 is displayed. These results match relatively well with the predicted attenuation from the theoretical and simulated results in the previous sections. Overall, the lowest measured attenuation of a ridge waveguide with a ridge width of $460\mu m$ and a height of $40\mu m$ is approximately 0.4 dB/mm at 100 GHz, or 0.5dB/mm at 300 GHz.

3.5 Error Analysis and Discussion

In this chapter, the measurement of silicon based dielectric ridge waveguides is presented. Similar to the last chapter, errors in the probing and coupling are expected due to the nature of the THz system. Again, the alignment of the probes with the sample is critical, but very difficult to quantify. Another factor which occurs in the measurement of the ridge waveguides directly on silicon wafers is that the wafers are not perfectly diced evenly between samples. This leads to slightly different transmission and coupling characteristics between samples due to the differences on the edge of the wafer. For more discussion on the errors involved

with probe coupling, refer to the previous chapter.

3.6 Conclusions and Discussion

This chapter displays the potential for dielectric ridge waveguides for THz on-wafer applications. The waveguides show relatively low-loss even at high frequencies ($> 300GHz$). This is confirmed through both theoretical approximations as well as FEM simulation. The waveguides also have very wideband single-mode propagation at frequencies well into the THz region. The simulated and theoretical attenuation for various ridge height and widths are compared, with attenuation as low as 0.45 dB/mm at 300 GHz. Finally, a method of fabricating and measuring the waveguides is presented. These methods allow for simple and

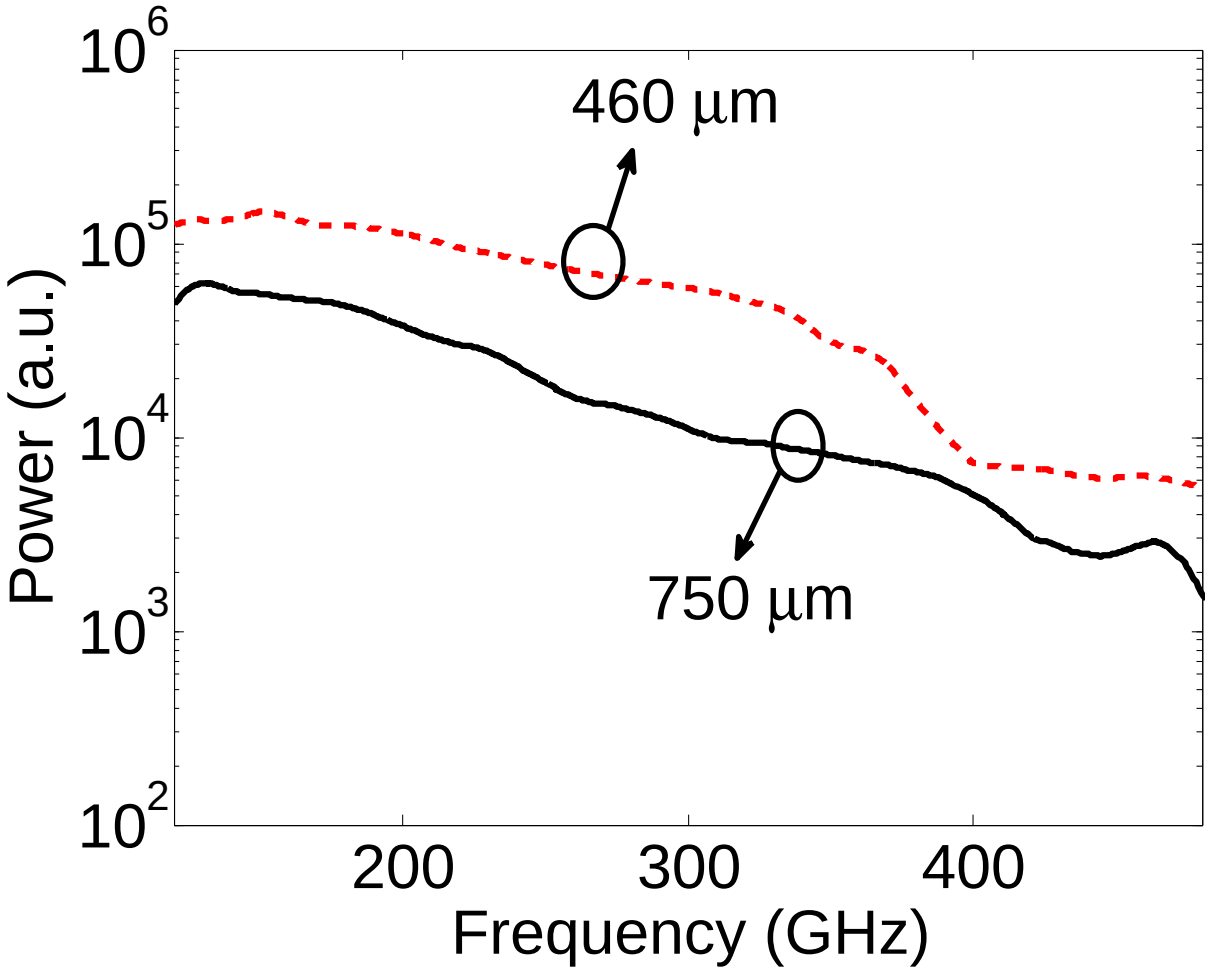

Figure 3.24 Measured transmission for ridge waveguides with $80\mu m$ ridge height, with two different ridge widths (normalized power).

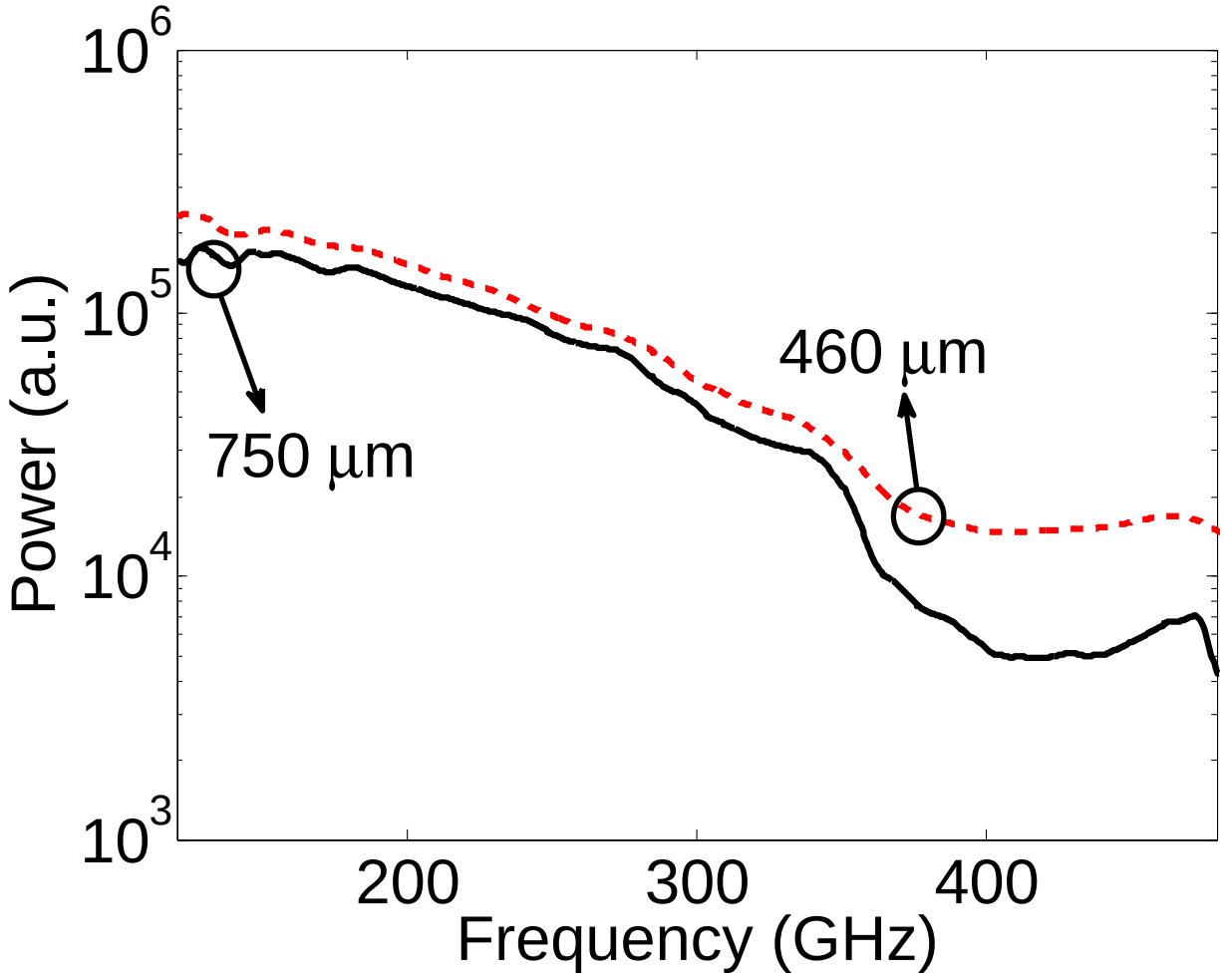

Figure 3.25 Measured transmission for ridge waveguides with $40\mu m$ ridge height, with two different ridge widths (normalized power).

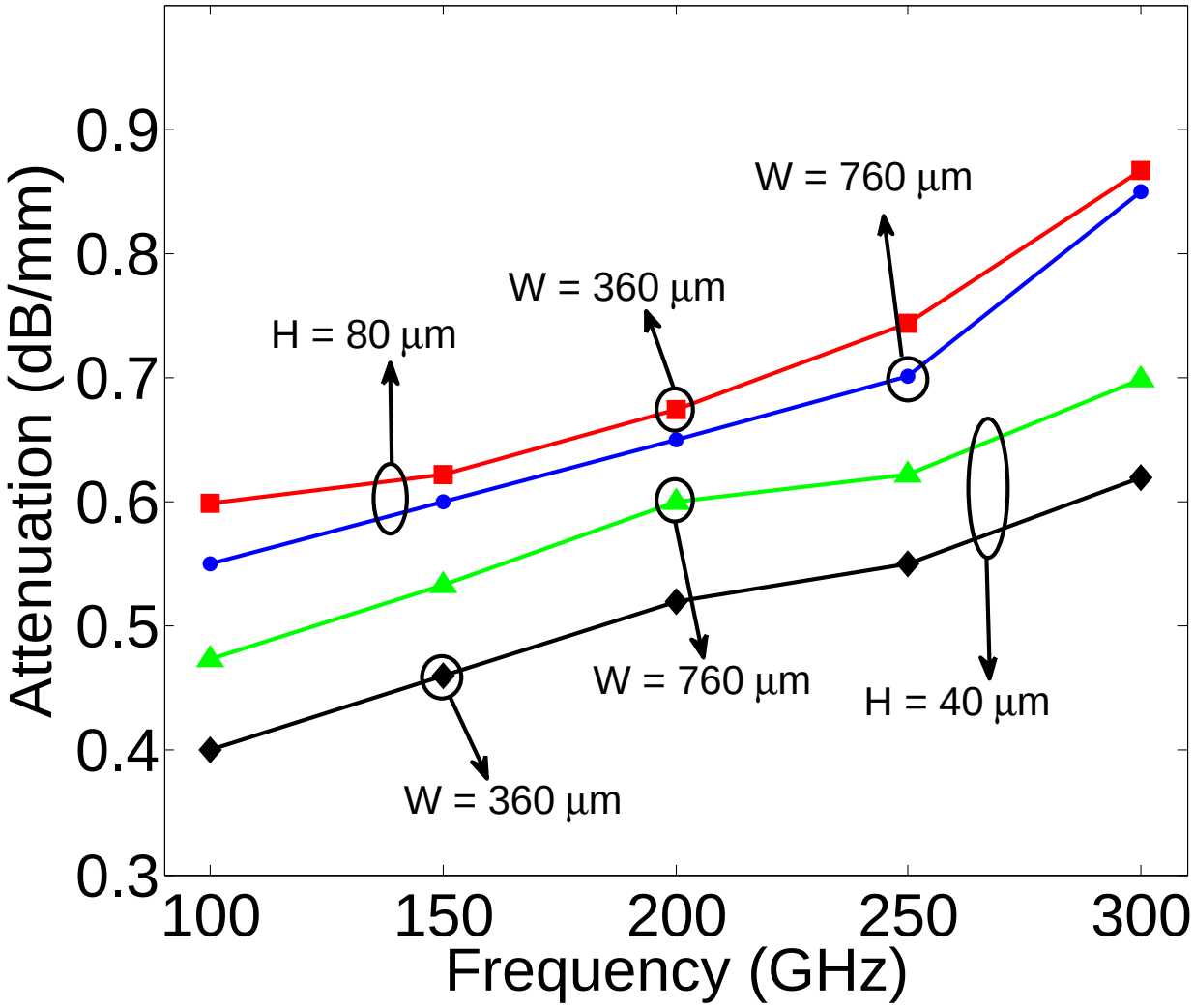

Figure 3.26 Measured attenuation of several ridge waveguides.

efficient coupling between wafer-level waveguide and current quasi-optical THz systems. The measured attenuation also shows relatively good agreement with the 0.4 dB/mm at 200 GHz. Overall, the dielectric ridge waveguides present a very promising solution to the complex problem of high frequency interconnects that are compatible with on-wafer applications.

CHAPTER 4

Optimization of Thin-film Terahertz Filters

In this chapter, the design of THz thin-film components using single and multi-objective evolutionary algorithms is introduced. Each structure is optimized through a HFSS-MATLAB interface with infinitely periodic boundary conditions and plane wave incidence. First, terahertz band-stop filters are investigated based on a dual-cross structure. The filters are optimized for rejection, bandwidth, and multi-resonant properties. A bandwidth of approximately 45 GHz with -25dB of rejection at 300 GHz is observed, as well as multi-resonant filters at 250 and 300 GHz.

4.1 Optimization Techniques in Electromagnetics

A number of problems in electromagnetics become difficult to solve with conventional analytic equations. Most of these problems can be solved using numerical means, however, a number of problems exist that require very complex structures with many possible variables. Optimization can be used to solve these types of problems, and is widely used in many area of electromagnetics such as antenna design and material characterization, along with others. There are three conventional categories of optimization and search methods used in the

current literature. These three methods include calculus-based, exhaustive search, and random search methods [94]-[95]. All of these methods, as well as non-traditional optimization method based on natural selection, are subsequently introduced in this section.

4.1.1 Calculus-based Optimization Methods

Calculus-based methods are widely studied throughout a variety of research areas. These methods involve seeking local maxima and minima by solving the gradient of the desired objective function set equal to zero. Given a smooth objective function, finding a corresponding peak involves calculating derivatives in a local area and finding where they converge to zero. While this method is local in scope, for a function similar to the one shown in Figure 4.1 the peak location and value of the objective function can be easily found. However, this method is extremely dependent on the location of the initial guess for the search. Depending on the guess, there may be no way to tell if the maximum of the objective function is a local maxima, or a global maxima. This means that the solution the method converges to may not be the optimal, or even best, solution available. For example, if the domain of the function shown in Figure 4.1 is extended as shown in Figure 4.2. The current maxima is revealed to not be the global maxima in the area, meaning a better solution could be found with a different initial guess. In addition, these methods depend upon the existence of well defined derivatives which may not always be available.

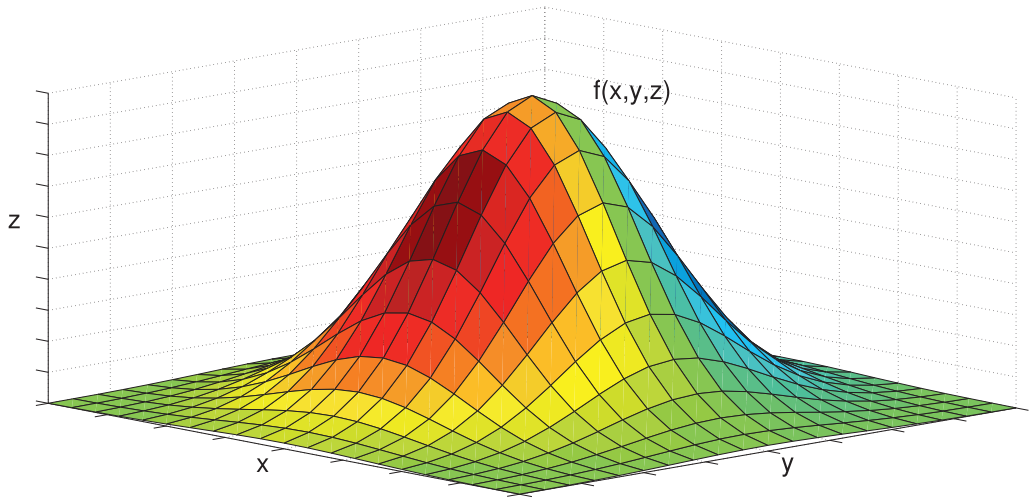

Figure 4.1 Local maximum of function f(x,y,z).

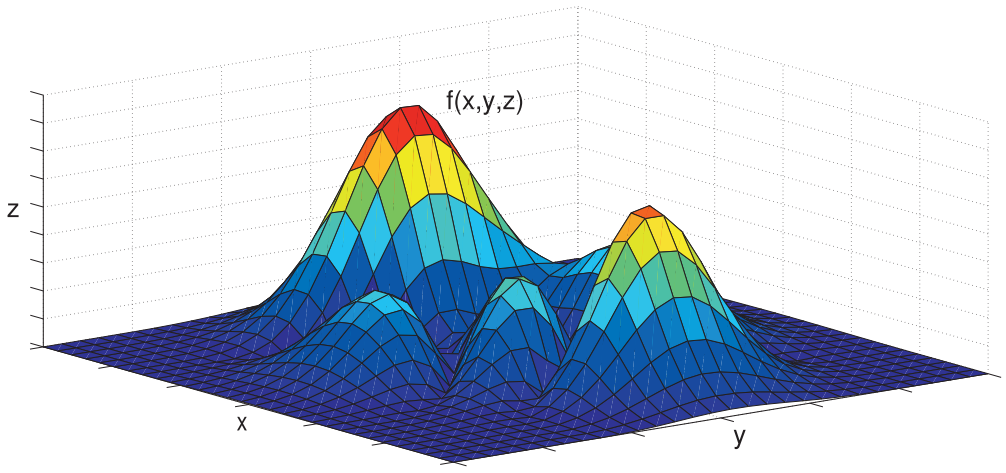

Figure 4.2 Extended domain of function f(x,y,z) showing multiple maximas.

4.1.2 Enumerative Optimization Schemes

The idea of an enumerative (also known as exhaustive) search is possibly the most straight forward method. Within a finite search space, the algorithm will evaluate the desired objective function at all possible points within the space. The simplicity of this search is very attractive, and for small solution spaces can be effective. However, for more complex problems, these methods lack the necessary efficiency. Searching a large sample space element by element simply takes far to long.

4.1.3 Random Search Algorithms

Random search algorithms have been shown to be effective for many problems. These search methods involve randomly selecting points along the desired solution space, as opposed to an exhaustive search searching every point. These techniques also have some of the short comings of the exhaustive searches. Once again, the efficiency of such a search can be far too low for very complex problems. However, for many desired solution spaces, a random search is able to find satisfactory results.

4.1.4 Genetic Algorithm Optimization

The genetic algorithm (GA) is an optimization and search technique based on the principles of natural selection. These algorithms are widely used in many different engineering applications in a wide range of fields. A GA allows a population composed of many individuals to "evolve" under specific rules in order to maximize a desired fitness, or cost, function associated with the current problem. GA optimization has many advantages over the optimization techniques described previously. For example, the GA can optimize with continuous or discrete values, although in this work only the discrete binary GA is used. In addition, this method does not require and derivative information. GAs can also simultaneously search a wide range of objective functions and deal with a large number of variables.

In addition, finding a local minimum or maximum as opposed to a global one is not an issue with a GA, meaning that extremely complex objective functions can be evaluated. Finally, GAs also work very well with numerically or experimentally generated data as opposed to analytic functions. These advantages provide an interesting optimization approach that can solve many problems the previous search and optimization methods cannot. A thorough explanation of the processes of the GA optimization technique is presented in the section, with each component explained separately. In addition, some current applications of GA optimization in electromagnetic problems are presented.

4.1.4.1 Fitness Functions and Chromosomes

A fitness function (sometimes called a cost function) represent the desired solution space that the GA will attempt to minimize (sometimes maximize). This function generates an output from a set of input variables. These input variables in the GA are referred to as a chromosome. The GA begins by defining a chromosome array to be optimized. If the length of the chromosome is N_{bits}, and each element of the chromosome are given by P_{Nbits}, then a chromosome can be written in the following way.

$$chromosome = [P_1, P_2, ..., P_{Nbits}] \tag{4.1}$$

4.1.4.2 Variable Selection

As the variables of the GA are represented as binary, the actual meaning of the variables must be translated into binary bits. To illustrate this concept, a sheet discretized into square pixels with equal sides of a length is shown in Figure 4.3. Each pixel can be in two possible states, on or off. In this case, a 1 can be thought of as an on state, and a 0 can be thought of as an off state. The grid has 10 rows and 10 columns, and the overall geometry is representative of a chromosome of 100 bit length. For example, the the chromosome representing the

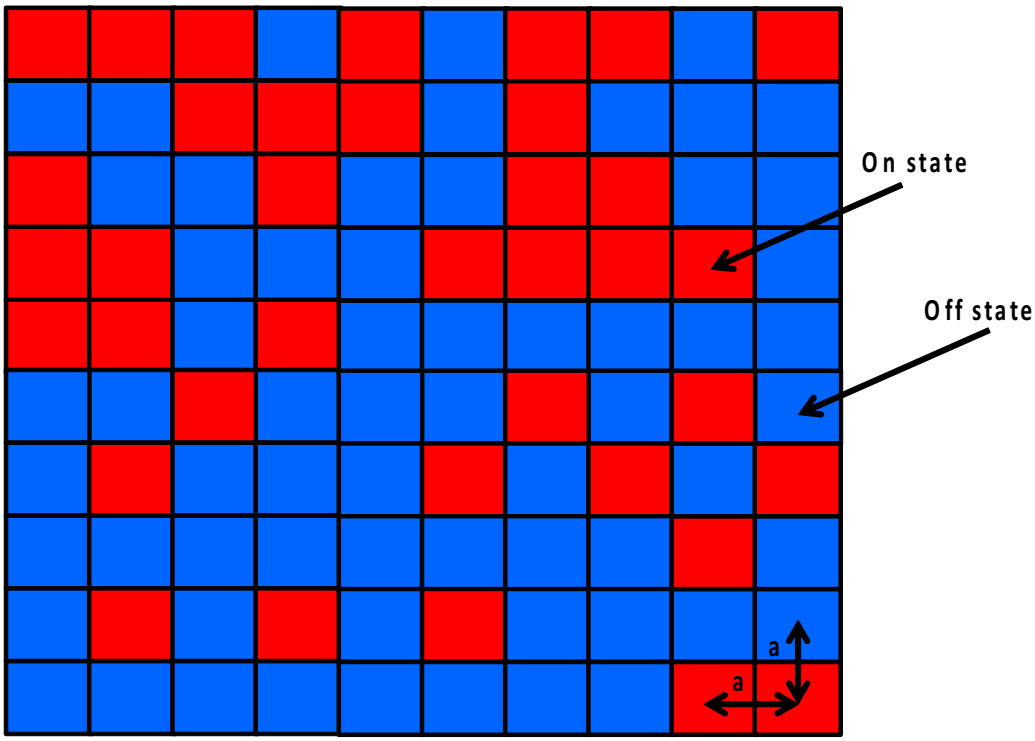

Figure 4.3 Sample discretized pixel grid.

geometry of the grid can be written as be represented as in equation 1.3.

$$chromosome = [1110101101....] \tag{4.2}$$

With this discretization, the binary bits are able to be represented in the geometry we wish to optimize.

4.1.4.3 Population

The collection of all the chromosomes within the GA is known as the population. The population has N_{pop} chromosomes and each chromosome has N_{bits} so the population will be an matrix of N_{pop} by N_{bits} in size. In order to begin the GA optimization process, an initial population must be generated. The initial population is found by performing a random search and filling the population with random ones and zeros. This initial population is then passed into the fitness function to be evaluated.

4.1.4.4 Selection

From the evaluation of the initial population, the best chromosomes are selected by the GA. This is done by first ranking the chromosomes from best to worse according to the desired fitness function. From here, only the best chromosomes are kept and the others are discarded. The number of chromosomes to be kept are selected based on the selection rate, X_{rate}, which represented the fraction of the N_{pop} chromosomes that are kept. The number of chromosomes that are kept are given by

$$N_{keep} = X_{rate} N_{pop} \tag{4.3}$$

Selection occurs at each iteration (known as a generation) of the algorithm. Deciding how

many chromosomes are kept depends on the application. However, keeping too few will limit the availability of genes in the offspring. Keeping too many chromosomes could bring in too many bad performers from the previous generation.

Two chromosomes are then selected from the remaining chromosomes N_{keep} to produce two new offspring until the discard chromosomes are replaced. While there are a number of techniques used for the selection of the new chromosomes, a tournament selection method is used throughout this thesis. Tournament selection involves randomly picking a small subset of chromosomes from the remaining pool, and the chromosome within this selection with the best fitness is chosen to become a parent. The tournament repeats until every parent needed to regenerate the population of chromosomes are found. This method works especially well for large populations because there is no extra sorting necessary.

4.1.4.5 Mating

Mating is the creation of offspring from the parents found in the selection process. The most common form of mating involves two parents which create two offspring. A crossover point between two parents is chosen randomly between the first and last bit of both parents chromosomes. The first parent will pass its binary code to the left of the crossover point to the first offspring. The second parent also passes its binary code to the second offspring from the left of the same crossover point. The binary code to the right of the crossover point of the first parent is then passed to the second offspring, while the binary bits to the right of the crossover point for the second parent are passed to the first offspring. This leaves us with two offspring with the genetic makeup of both parents, which are used to replace the two parents selected for N_{keep}. This process is summarized in Figure 4.4

4.1.4.6 Mutations

Random mutations are also used to alter the a percentage of the remaining population matrix. Mutation introduces another element to the optimization process by introducing traits into

the population that were not initially present in the selected parents and offspring. In the binary GA, mutation can be as simple as changing a single bit in a chromosome from a 1 to a 0, or vice versa. Mutation is important for the GA process as it introduces traits not found in the selected parents and offspring to fill the population. Without mutation, the GA may converge too quickly to an answer that does not include other possible combinations. The number of mutations are given by equation 1.5, where μ_{rate} is the desired number of mutations for the entire population.

$$mutations = \mu_{rate}(N_{pop} - 1)N_{bits} \tag{4.4}$$

4.1.4.7 Convergence and Future Generations

After the mutations takes place and the fitness functions associated with the offspring are calculated, the results are compared with a stopping criteria. If the stopping criteria is not met, the algorithm takes the current population and begins the selection process again in a new generation. If the criteria is met, the algorithm will stop and the results will be exported. The overall GA optimization process is shown in Figure 4.5.

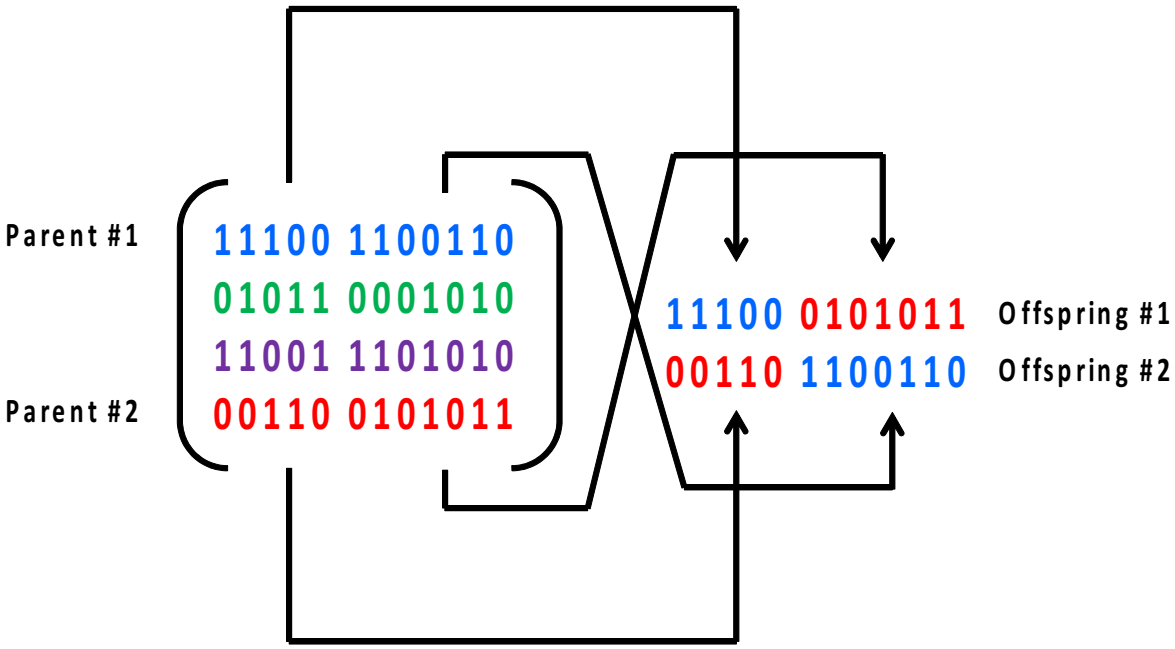

Figure 4.4 Mating process in the binary genetic algorithm.

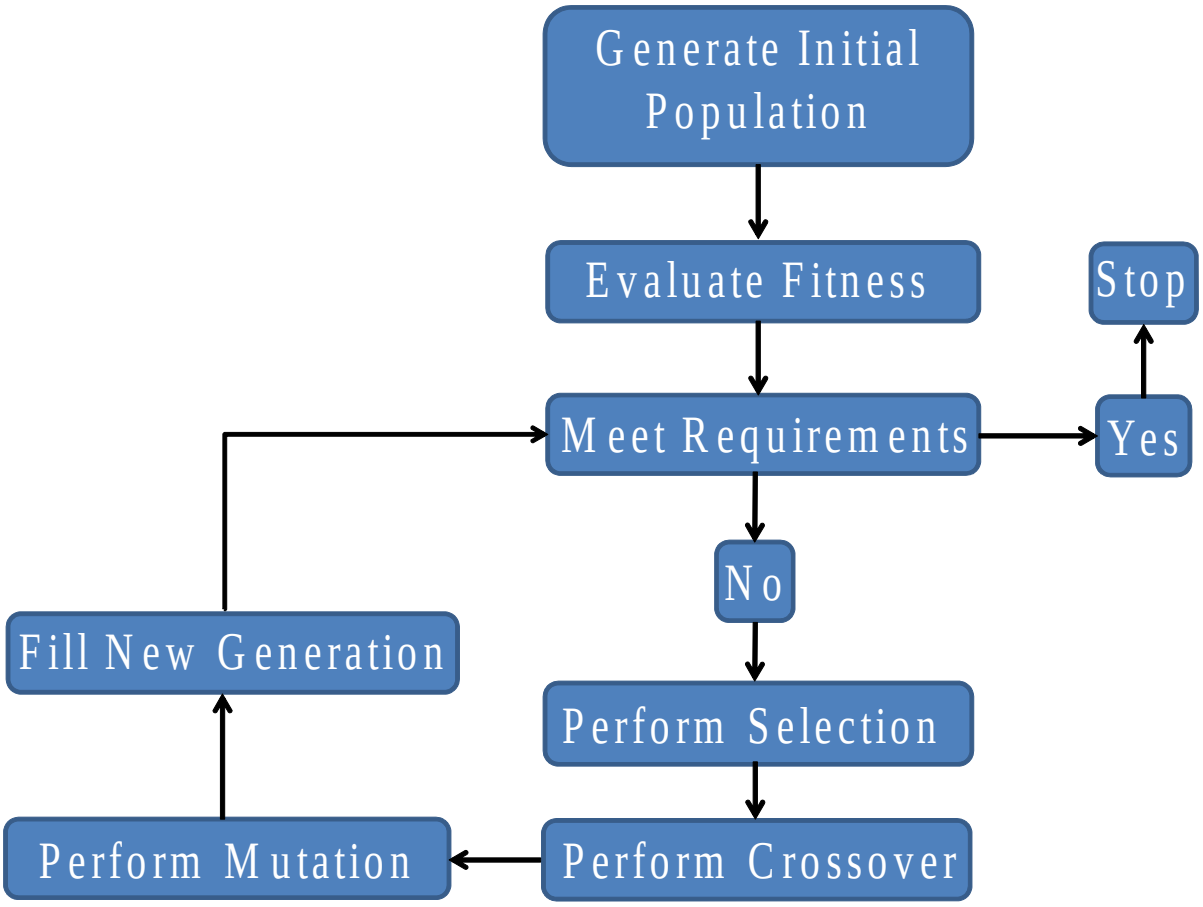

Figure 4.5 Summary of genetic algorithm optimization process.

4.1.5 Multi-objective Optimization

the GA has been primarily studied as a single-objective algorithm, and in the past was widely believed to be incompatible with multi-objective problems [97]. In recent years, however, a number of promising multi-objective GAs have been established, including the pareto evolutionary algorthm (SPEA) [98], the multi-objective genetic algorithm (MOGA) [99], and the non-dominated sorting algorithm (NSGA) [100]. In particular, an elitist based version of NSGA, called NSGA-II, has been extremely popular for many multi-objective optimization applications [101].

4.1.5.1 NSGA-II

When dealing with multiple objectives, the raw fitness value of each objective does not describe necessarily the best solution. When two or more objectives are considered, a pareto optimal front is formed between each solution representing the tradeoff between each objective. Therefore, the goal of such an optimization procedure is to first find solutions as close as possible to the pareto efficient front (the best possible set of solutions), as well as maximize the number of possible tradeoff points along the pareto front.

To handle the multi-objective nature of the problem, NSGA-II is used optimize multiple characteristics of the filter. NSGA-II primarily differs from the single-objective GA shown in Figure 4.5 by the evaluation of the fitness of each objective. In this case, the fitness of each objective is first calculated for each member of the population. A new population is then created, R_t. This population contains the fitnesss of each objective for the previous generation (known as the parents), as well as the previous generation after selection, mutation, and crossover (known as the children) such that $R_t = [P_t Q_t]$, where P_t is the parent population, and Q_t is the child population.

R_t is then divided into non-dominated fronts which are used to sort the trade-offs of each objective. The best fronts are chosen and kept in the next generation of the algorithm,

referred to as P_{t+1}, which is of the same size as the initial population. Therefore, the members of low-ranking fronts will be discarded, only leaving the best trade-off solutions. However, there will most likely be some overlap between a single front at the border of the cutoff for the next generation. Members of this front are chosen for the next generation based off of the distance between their location and the location of the nearest point on the front. The points with the maximum distance from other points (known as the crowding distance) are chosen for the next generation. In this case, the end points are always preferred and assigned an infinite crowding distance. This allows for not only the best solutions to be present in the next generation, but also ensures the most diverse solutions are also preserved. The overall process of the NSGA-II algorithm is shown in Figure 4.6.

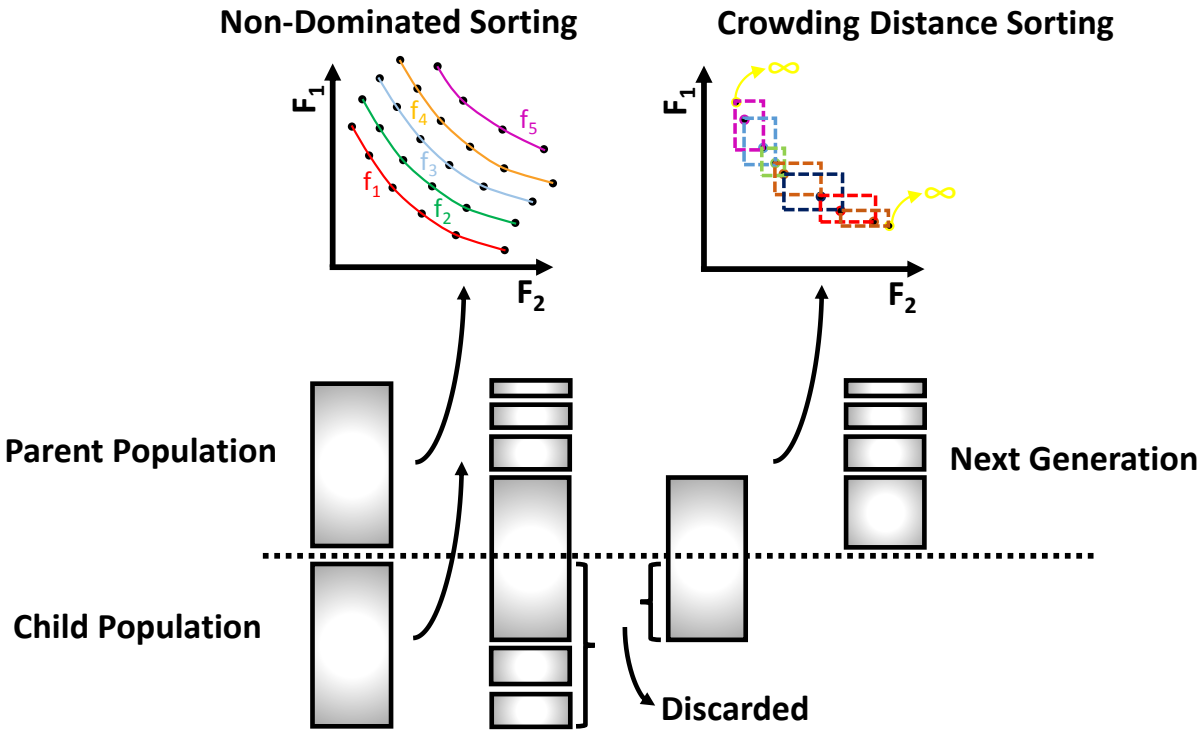

Figure 4.6 NSGA-II optimization process.

4.1.6 Applications of Genetic Algorithms in Electromagnetics

Genetic algorithms are used as an optimization tool in a wide variety of Electromagnetics problems. In [102], genetic algorithms are used to synthesize light-weight, broadband microwave absorbers. The absorber is intended to be as light-weight as possible, while being thin and multi-layered, backed with a PEC conductor. Each layer of the antenna is optimized with a frequency dependent material, while the permittivity and permeability are varied. The reflectivity of the array is optimized while changing the materials in the array-stack, while keeping the stack as thin as possible. A wide range of frequency absorbers are designed, with reflection coefficients ranging from .2-8GHz.

These algorithms have also been used in the design of frequency selective surface (FSS) structures [103]. In this work, the FSS structures are desired to be used as waveguide filters. As the filter characteristics depend upon the shape and size of the individual elements, as well as the number of element layers, both are optimized with the GA. Very strong bandpass and bandstop filters are shown in this work, at frequencies as high as 25GHz.

GAs are also widely used in antenna array design. In [104], the sidelobe levels of an antenna array are decreased by thinning or removing the elements that makeup an array. This is done by representing the elements with a binary number, and turning them to either a 1 or 0 based on if the element is on or off. Extremely low sidelobe levels, as low as -22dB, are reported. Refrence [105] uses the genetic algorithm to optimize a linear antenna array to shape the mainbeam of the radiation pattern. In this case, the goal is to select a set of amplitude and phase coefficients for the antenna to achieve a narrow beam at a specific location.

Optimization has also been done extensively on single antenna elements. In [106], a patch antenna is optimized so that the bandwidth of the antenna is significantly wider than a traditional patch. The GA is coupled with a method of moments so that a binary string could represent the presence or absence of a subsection of metal in the patch. With this

method, the bandwidth of one patch was able to be increased by approximately 20%. The GA optimization method has also been recently used to miniaturize antennas.

In [108], a patch antenna is miniaturized by placing SRRs between the top layer of the antenna and the ground plane. The geometry of the SRRs are optimized with a GA, while the fitness function is designed to minimize the reflection coefficient of the antenna. A good impedance match and radiation characteristics are maintained with the optimization, and one state is shown to achieve a miniaturization of approximately 1/16th the size of the original patch. [107] presents a loop antenna that is miniaturized using a binary GA. The loop antenna is printed on a planar dielectric, with a pixelized sheet directly above it. Each pixel is controlled with the binary GA and the fitness function is chosen to miniaturize the reflection coefficient at a desired frequency.

Another miniaturization method is presented in [110]. In this work, a monopole antenna is surrounded by a metallic pixelized grid controlled by a binary GA. The pixel grid is used to miniaturize the antenna through control of the GA. The radiation characteristics of the monopole are well maintained throughout the miniaturization, and an overall miniaturization of $\lambda_0/26$ is achieved. All three of these methods are implemented using a HFSS-matlab interface, which will be discussed in detail in the following section.

4.2 HFSS-MATLAB Optimization Interface

In order to implement the GA optimization successfully with an electromagnetics problem, a numerical solution method must usually be implemented. While some simple problems can be solved through analytic equations, most require approximate solutions. There are many numerical solution techniques that can be used, however, perhaps the most popular method is in the use of commercial electromagnetics solvers. One such commercial solver is Ansys High Frequency Structural Simulator (HFSS), which is based on a finite element method. This solver has a CAD like interface which can be easily used and can implement a number

of solution methods in both the frequency and time domain.

Implementing a GA to solve a problem iteratively is unfortunately not available in HFSS. However, HFSS commands are able to be executed through simple macro scripts that can be imported and run in real time. These macros can be executed through MATLAB, and compiled into a script which can be imported to HFSS. This allows for the automated creation of geometry, boundary conditions, and excitations in HFSS. This allows the geometry to be altered after every iteration of a parameter, meaning a GA can be used to optimize structures with an interface between HFSS and matlab.

An overall flow of the optimization process is as follows. First, matlab is launched and the GA parameters are initialized. The geometry is then created for the first iteration of the GA. The script is then assembled and HFSS is launched. The script is passed to HFSS, and the geometry is drawn in real time. The structure is then simulated, and the relevant results are exported back to matlab for post processing. If these results meet the desired requirements, then the GA is stopped. However, if the results do not meet the requirements desired, the overall process is restarted with a new geometry and the next iteration of the GA is performed. The overall flowchart for this process is shown in Figure 4.7.

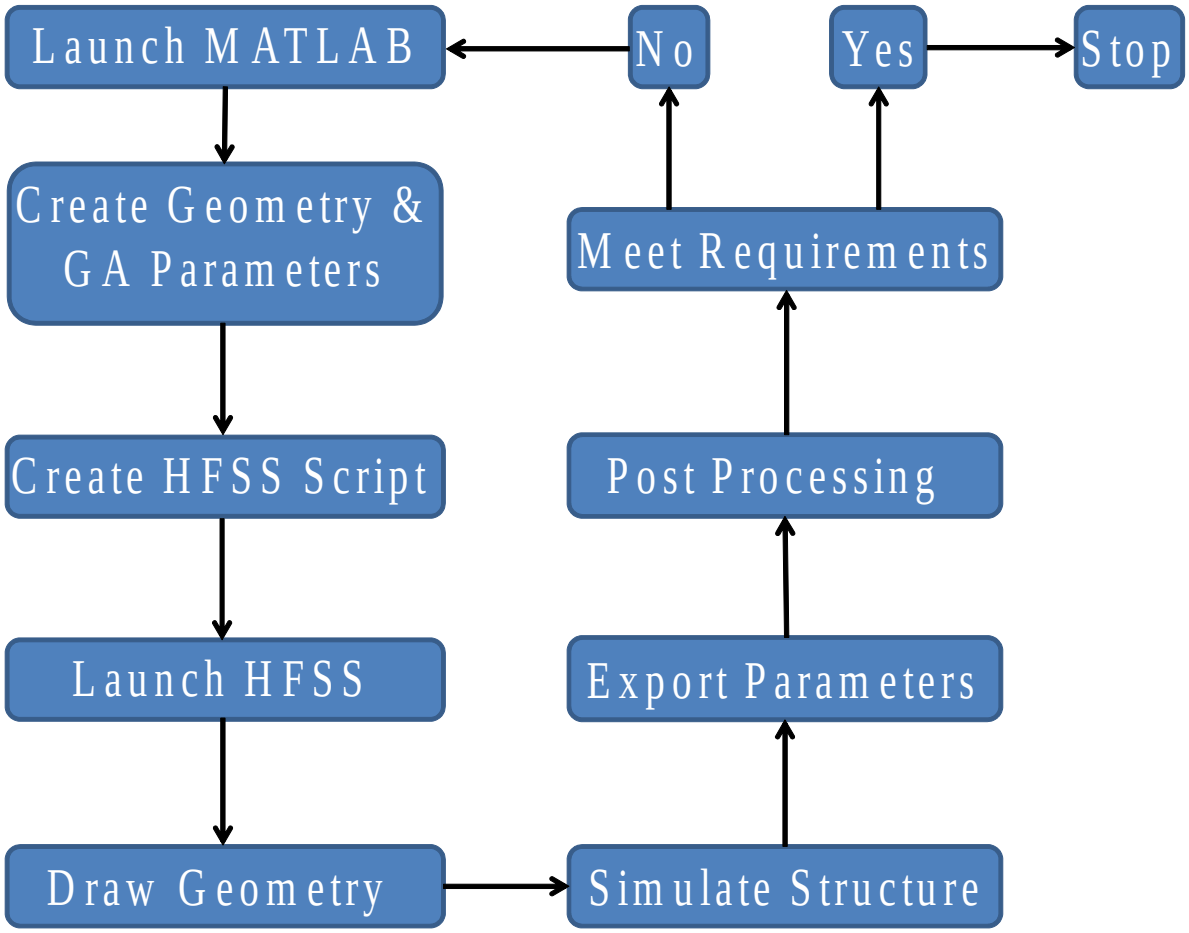

Figure 4.7 Genetic algorithm Matlab-HFSS interface flowchart

4.3 Filter Design and Implementation

The geometry of the suggested THz filter geometry is shown in Figure 4.8. The filter implemented here is based on a dual cross unit cell structure. However, the crosses are broken into small subsections, similar to the pixel grid example given in the previous sections. This allows the filter topology to be optimized to produce certain desired results.

In this case, Ansys HFSS is used along with periodic boundary conditions with a fundamental floquet-mode incidence to find the desired properties of the filter. The setup of the boundary conditions for the filter is shown in Figure 4.9. Further information pertaining to the floquet mode analysis is presented in the chapter 5. The overall unit cell size is given by $Y_p = X_p = 550\mu m$, with a outer cross length of $425\mu m$ and inner cross length of $300\mu m$. The crosses are split into small square pixel subsections with $a = 25\mu m$ sides. The filter is built on a $250\mu m$ polyethylene terephthalate (PET) substrate, with $\epsilon_r = 3.4$ and $tan\delta = .001$, found from the characterization in [117] at 300 GHz.

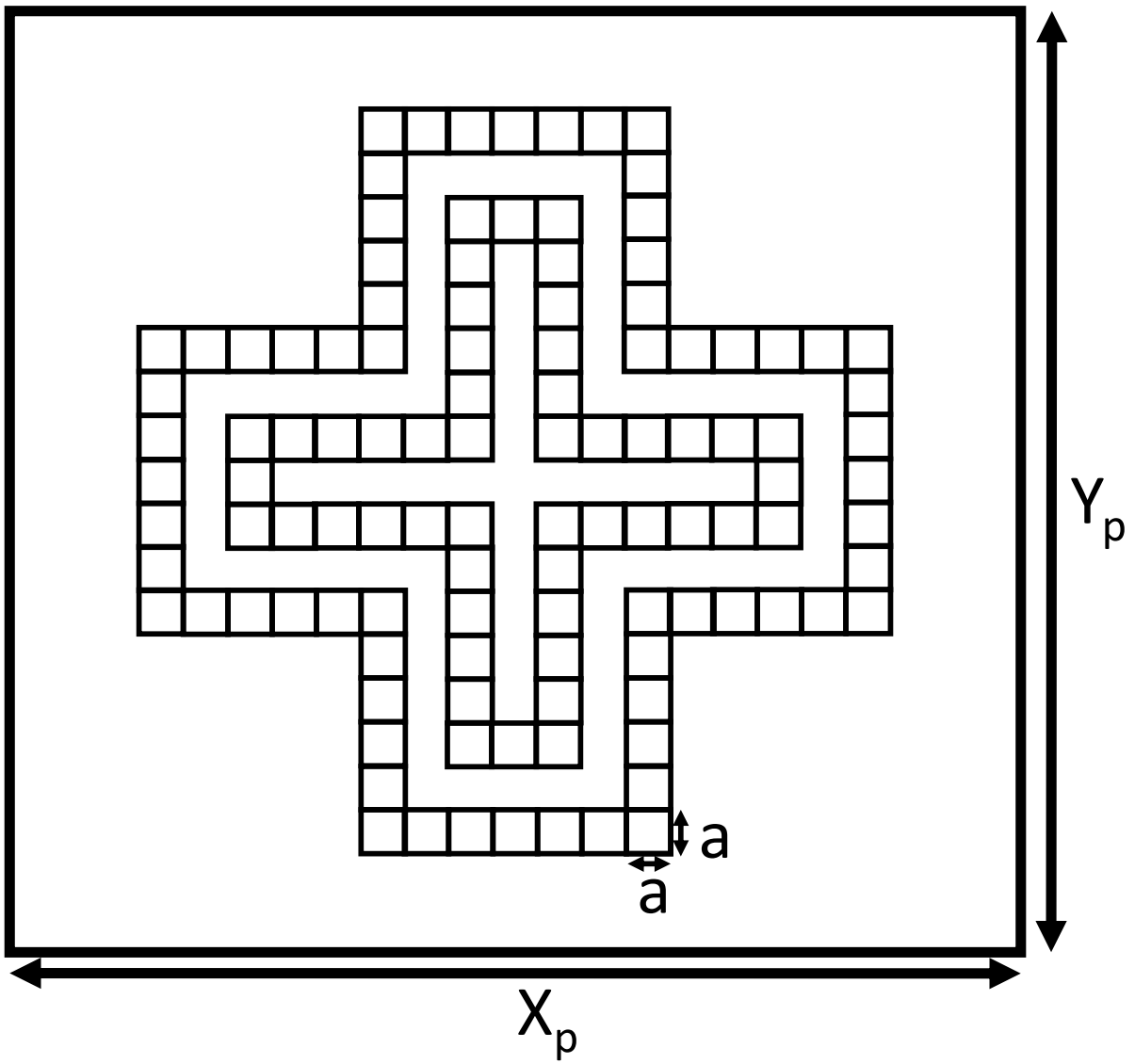

Figure 4.8 Proposed filter geometry.

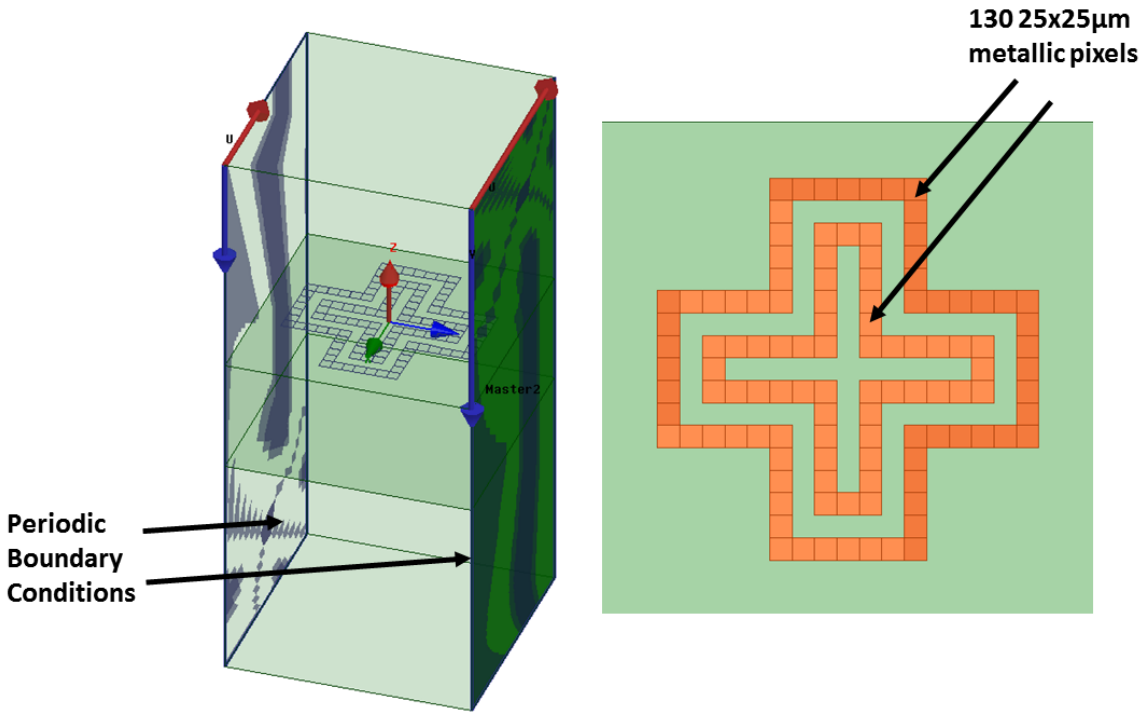

Figure 4.9 HFSS floquet mode modeling setup.

4.4 Implementation Test of NSGA-II Algorithm

First the NSGA-II algorithm is tested to ensure convergence and diversity among its solutions, as well as to ensure the algorithm is performing correctly. Many multi-objective test problems have been introduced throughout the years [111] - [114]. The Zitzler-Deb-Thiele (ZDT) test functions have been particularly useful since being introduced in [115]. The ZDT test problems consist (at least initially) of 6 functions which test the convergence and complexity of a multi-objective optimized. Since the multi-objective algorithm used here is a binary NSGA-II as opposed to a real coded version, the test problem ZDT5 is used as it is particular useful in testing binary coded GAs. The representative equations for ZDT5 are shown in equations 2-5.

$$f_1(x) = 1 + u(x_1) \tag{4.5}$$

$$g(x) = \sum_{i=2}^{11} V(u(x_i)) \tag{4.6}$$

$$h(f_1(x), g(x)) = \frac{1}{f_1(x)} \tag{4.7}$$

$$V(u(x_i)) = \begin{cases} 2 + u(x_i) & u(x_i) < 5 \\ 1 & u(x_i) = 5 \end{cases} \tag{4.8}$$

The NSGA-II algorithm is run with a population of 500, 10 % mutation, and 1000 generations. The results for the NSGA-II algorithm are shown in Figures 4.10 - 4.11. Figure 4.10 shows the attainment surfaces found for 5 runs compared with the global pareto optimal front. Figure 4.11 also shows the best run versus the global pareto optimal front. The NSGA-II algorithm constructed in this work shows good agreement with ZDT5, especially after f_1 is greater than three.

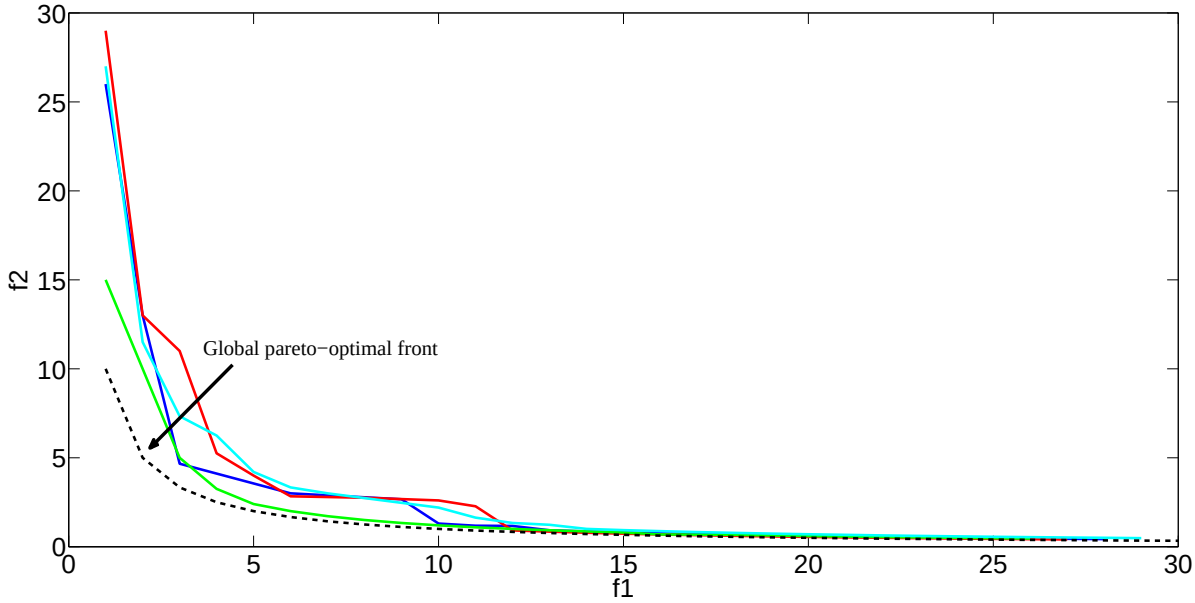

Figure 4.10 Attainment surfaces found from NSGA-II algorithm.

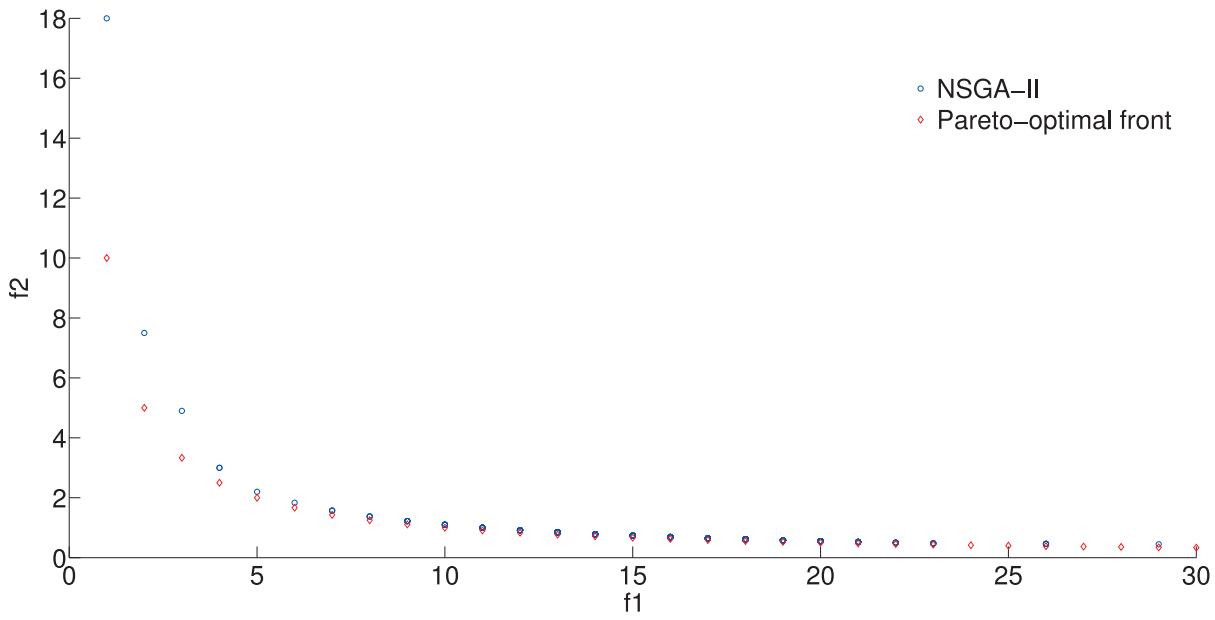

Figure 4.11 Convergence of NSGA-II to ZDT5 test problem.

4.5 FEM Simulation and Optimization Results

4.5.1 Single Objective Optimization

First, a single-objective GA is used to optimize the band-stop characteristics of the filter at 300 GHz, described by minimizing the following fitness function

$$F = |S_{21}|(300GHz) \tag{4.9}$$

where S_{21} is the transmission coefficient of the filter at 300 GHz. The single-objective GA used in this optimization process is interfaced through MATLAB with the EM solver HFSS 13.0. A single-bit mutation rate of 10%, along with single-bit crossover, an initial population of 240, and 115 total pixels are used as GA parameters. This arrangement leaves the GA optimization process with approximately 2^{115} possible combinations to chose from. In HFSS, the filter is modeled as an infinitely-periodic unit cell using master/slave boundary conditions and an incident TE polarized plane wave normal to the surface of the structure.

The results of three separate single-objective GA runs over 50 generations with the objective to minimize Equation 1 are displayed in Figure 4.12. A minimum S_{21} of approximately -24.68, -24.92, and -24.31 dB are found for each run, respectively. The low value of the transmission coefficient suggests that the described filter geometry and optimization technique are suitable to create a stopband like response at a desired frequency. In addition, the results of each run converge to approximately the same value, showing that the algorithm is repeatable.

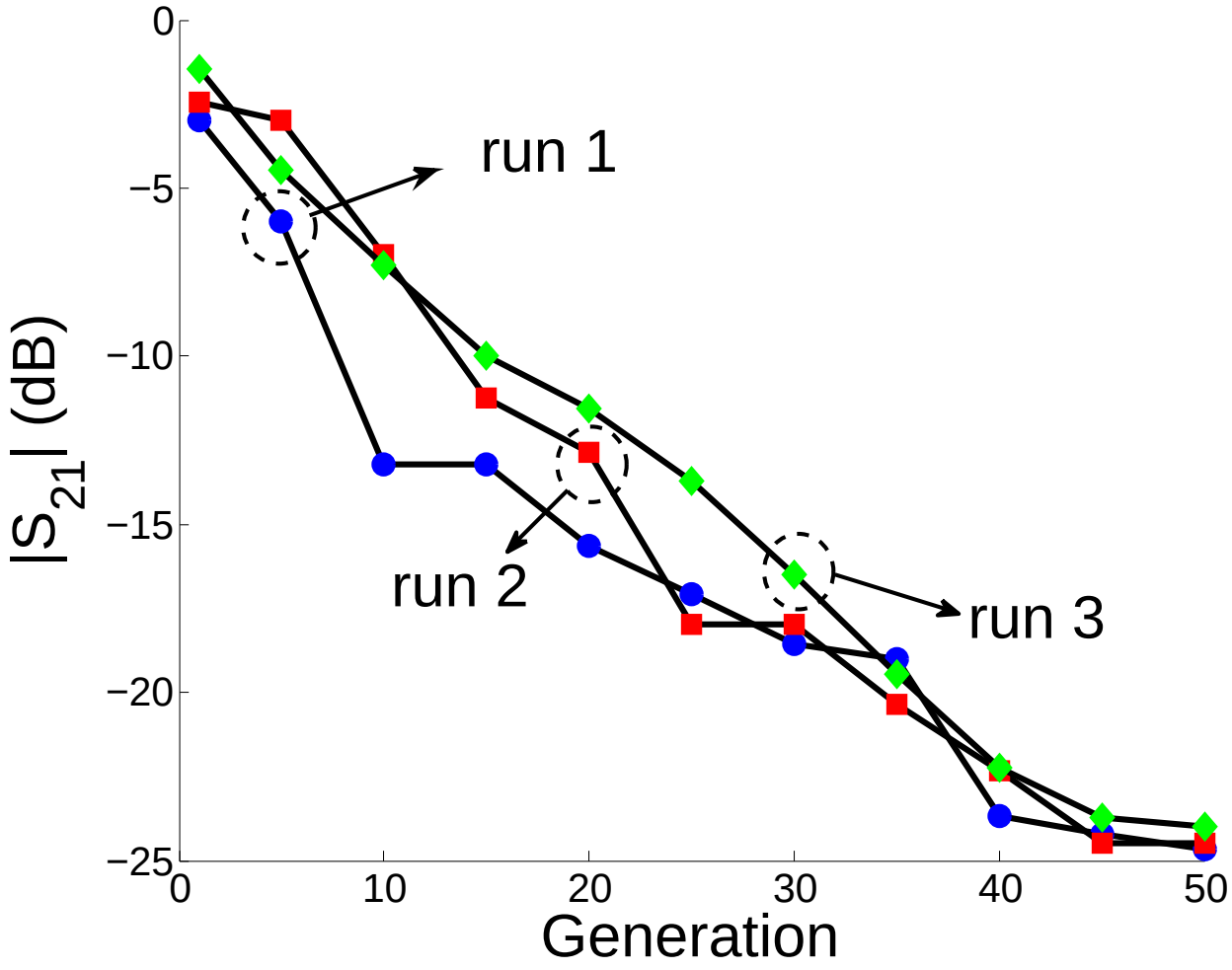

Figure 4.12 Progression of $|S_{21}|$ through GA generations.

4.5.2 Multi-Objective Optimization

While the single-objective results show promise in the rejection characteristics of the structure, other aspects of a filter are also desirable. However, a simple single-objective GA will not work when more than one characteristic is desired to be optimized simultaneously.

4.5.2.1 Optimization of Bandwidth and Stop-band

The first multi-objective filter design is a min-max problem, described with the following fitness functions described by P1.

$$P1 = \begin{cases} \text{Minimize} & F1 = 20\log_{10}(S_{21}(225:325GHz)) \\ \text{Maximize} & F2 = f_H - f_L \end{cases} \tag{4.10}$$

where f_H is the high frequency -3dB point and f_L is the low frequency -3dB point with respect to the center frequency of the stopband. Therefore, F2 represents the bandwidth of the stopband, and F1 represents the maximum rejection of the filter. The results of NSGA-II are shown in Figure 4.13 for a frequency range from 225 to 325 GHz. A pareto front is formed showing a tradeoff between solutions with a maximum rejection of approximately-25 dB and a maximum bandwidth of 44GHz. Keeping in mind that this is for a single layer thin-filter structure, a bandwidth of 44GHz is relatively large (and could drastically increased with multiple layers). In addition, the minimum S_{21} of approximately -25 dB matches well with the single-objective case, showing convergence between the single and multi-objective GAs. Figure 4.14 also shows the progression of the best fitness of each objective during the NSGA-II process over 30 generations.

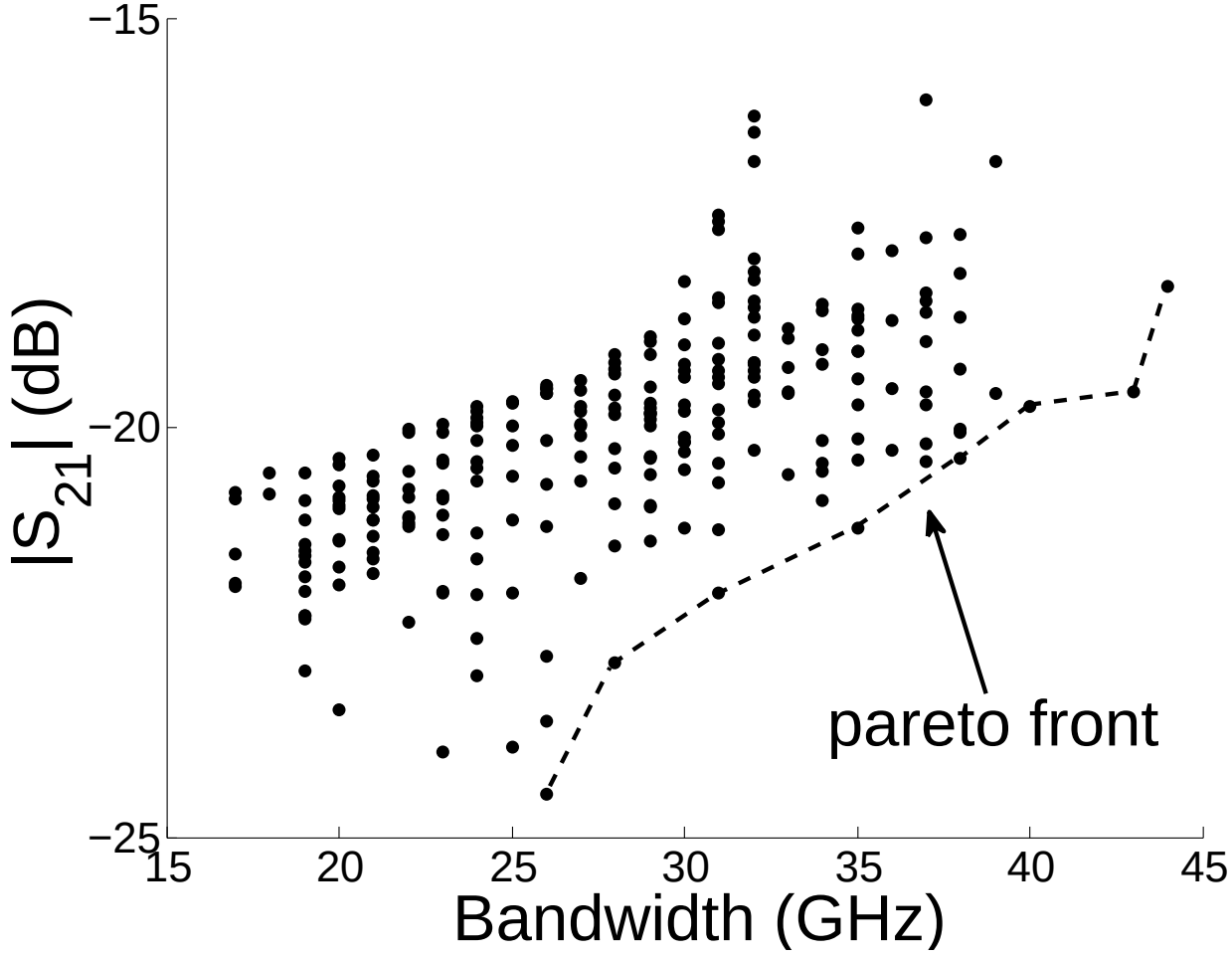

Figure 4.13 Solutions for P1 objective functions after 30 generations.

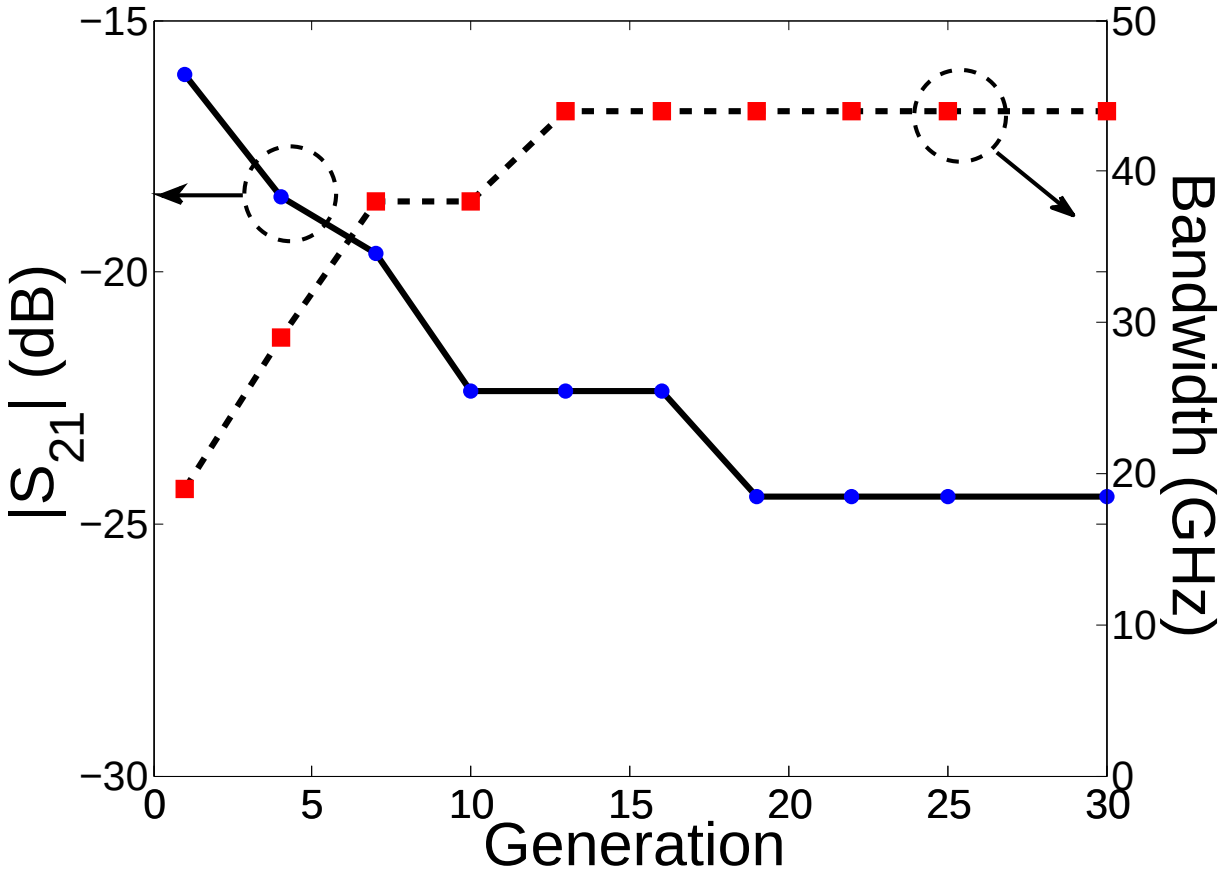

Figure 4.14 Progression of P1 objective functions through GA iterations.

4.5.2.2 Multi-resonant Optimization

Next, the min-min problem of the optimization of rejection at multiple frequency points is considered with NSGA-II using the following objective functions.

$$P2 = \begin{cases} \text{Minimize} & F1 = 20\log_{10}(S_{21}(300GHz)) \\ \text{Minimize} & F2 = 20\log_{10}(S_{21}(250GHz)) \end{cases} \quad (4.11)$$

In this case, P2 describes the rejection of the filter at the two frequencies 300 and 250 GHz. The tradeoff between these objectives is shown in Figure 4.15 after 80 generations of NSGA-II.

Clearly, a tradeoff between the two objectives is formed, and 5 pareto front members are found which describe a tradeoff between the resonances at each frequency. Figure 4.16 shows the progression of each objective as the generations of the GA are increased. Again, it is worth noting that F1 clearly converges to the single-objective case displayed at 300 GHz of approximately -25 dB.

4.5.2.3 Filter Implementation

Four filters found in the above analysis representing the ideal tradeoffs among each objective are evaluated over their full frequency spectrums using HFSS. Figures 4.17 and 4.18 display the S_{21} for two filters from the multi-resonant optimization described by P2 and the bandwidth optimization described by P1, respectively. The transmission through each filter clearly matches well with the expected results from the GA optimization process. In the case of the multi-resonant optimization, the filters show good out of band acceptance with the expected rejection properties at the optimized frequencies. Figure 10 shows solutions corresponding to the highest transmission, and the highest bandwidth. In this case, the highest bandwidth solution is at approximately 240 GHz, while the lowest transmission solution is at 320 GHz. These values match well with the expected results from the optimization procedure, with a bandwidth of approximately 45GHz and maximum rejection of -20dB for

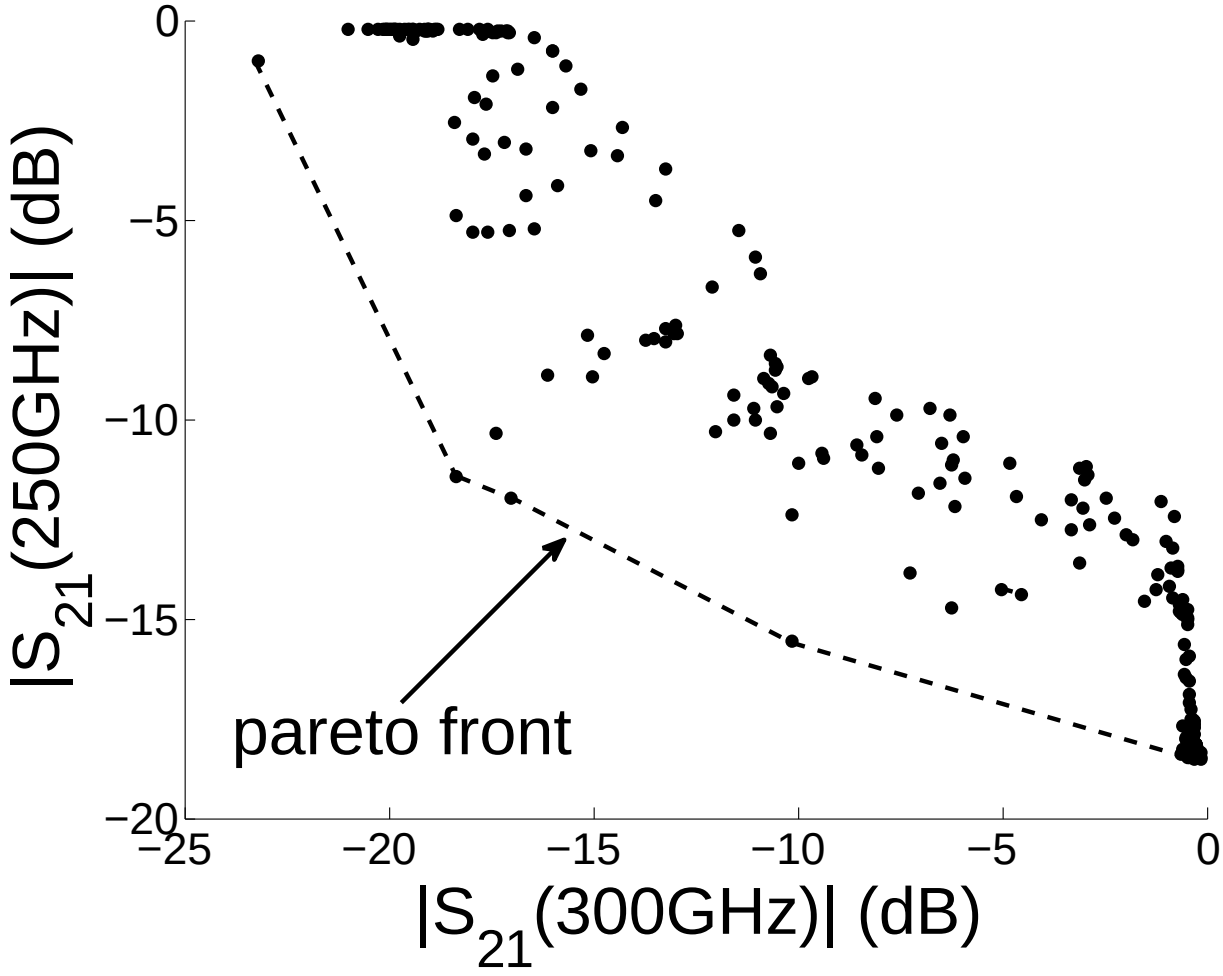

Figure 4.15 Solutions to P2 objective functions after 80 generations.

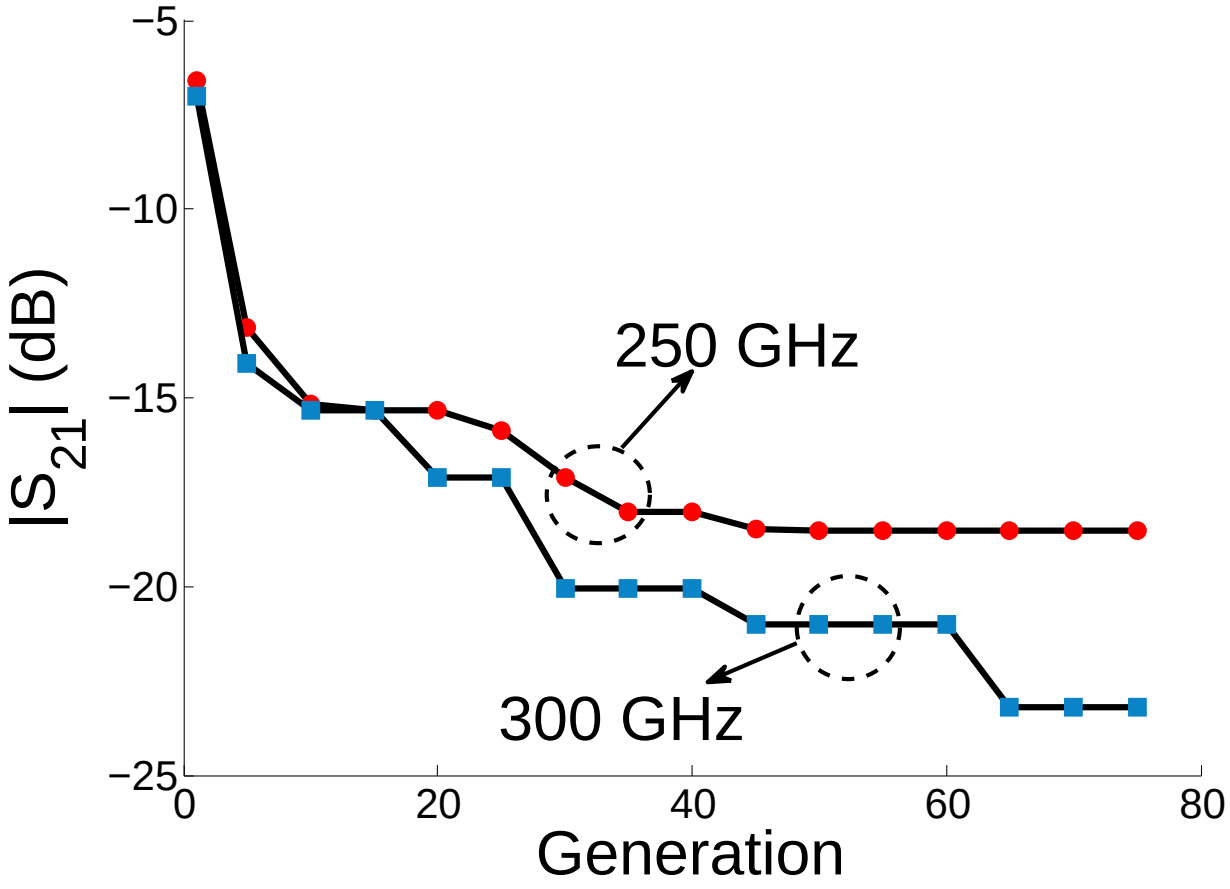

Figure 4.16 Progression of P2 objective functions through GA iterations.

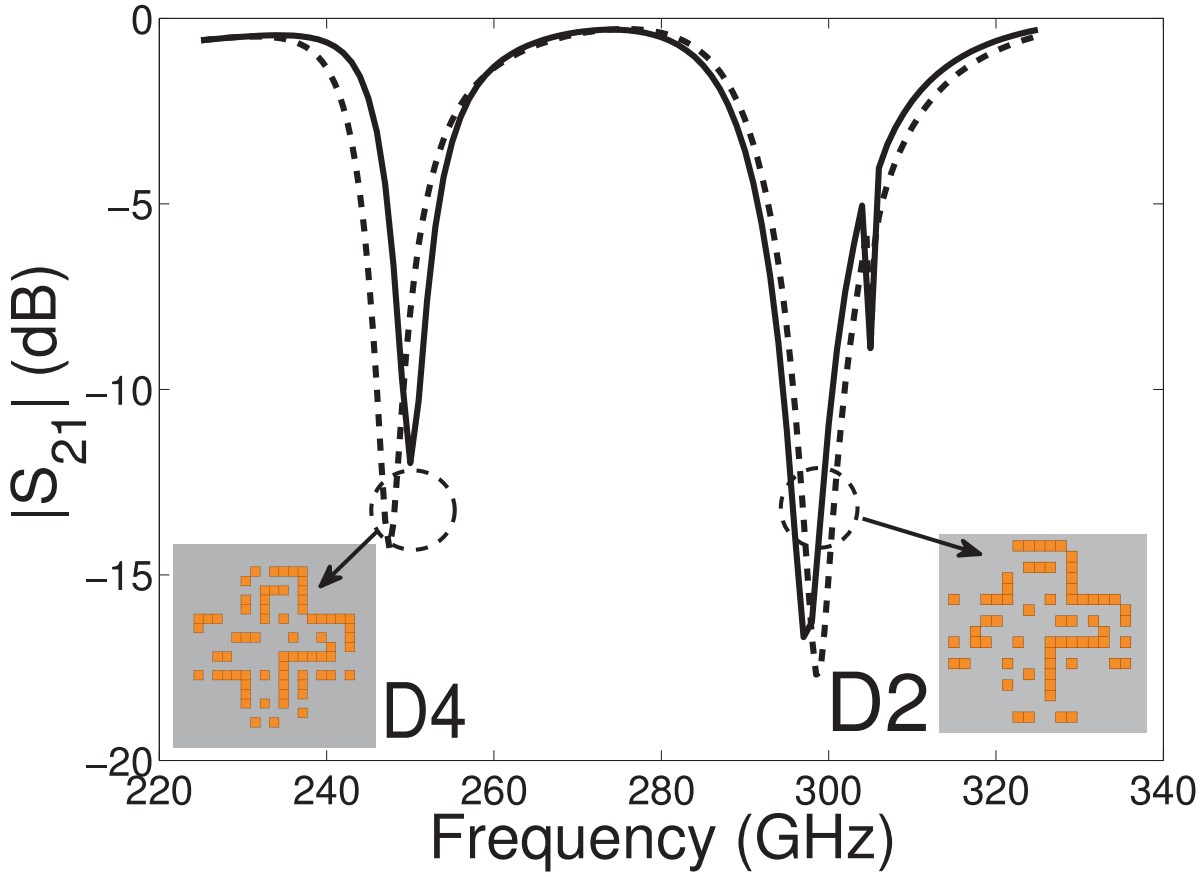

Figure 4.17 Two pareto front solutions from the P2 objective space.

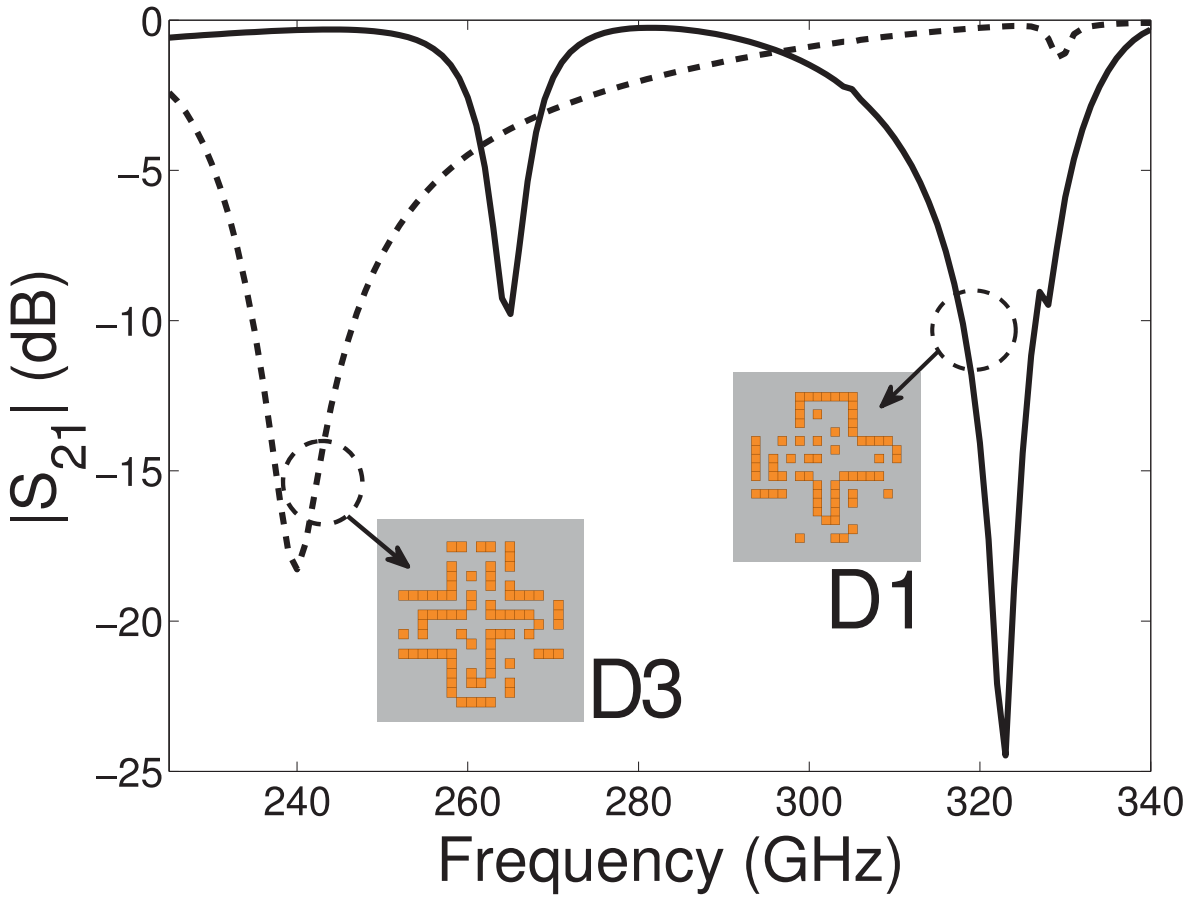

Figure 4.18 Two pareto front solutions from the P1 objective space corresponding to maximum transmission (D1) and maximum bandwidth (D2).

the highest bandwidth solution, and a bandwidth of approximately 25GHz and rejection of -25dB for the lowest transmission solution.

4.6 Measurement and Fabrication

Three filters from the above analysis are chosen for fabrication and measurement. These filters correspond to D1, D2, and D3 shown in Figures 4.17 and 4.18. The filters are fabricated on $250\mu m$ thick PET substrates, with $1\mu m$ of sputtered copper. Simple lithography and wet-etching is used to pattern the metal, with a minimum feature size of approximately $25\mu m$. The fabricated filters are shown in Figure 4.19, with a U.S. dime included for scale.

In order to characterize the filters, a Emcore PB-7200 THz frequency domain test system is used. The measurement system consists of two rigid receiver and transmitter heads, with a frequency range from 100GHz to 2 THz, and a sampling resolution as low as 10 MHz. To measure the sample, a reference measurement is required in order to isolate any noise from the result. In this case, a blank PET layer with the same thickness as the filter is used as a reference measurement. The PET layers are placed in a 2cm metallic window, designed to block out all transmission between the receiver and transmitter other than through the sample placed in the window. The overall test setup is shown in Figure 4.20.

Each filter is measured over a frequency range of 225 to 350 GHz, with a step resolution of 250 MHz. The resulting transmission spectra of each filter compared with the reference measurement is shown in Figure 4.21. The measured results match relatively well with the expected simulated and optimized results. D2 shows multi-resonant behavior at the two optimized frequencies of 250 and 300 GHz. D3 has the widest bandwidth among the samples as expected, and is shifted in frequency by approximately 25 GHz. D1 still shows a strong resonance, however, the frequency is shifted by approximately 50 GHz.

Overall, the measured results confirm that the band-stop characteristics of the filter can be optimized through a GA to achieve a desired response in the THz frequency spectrum.

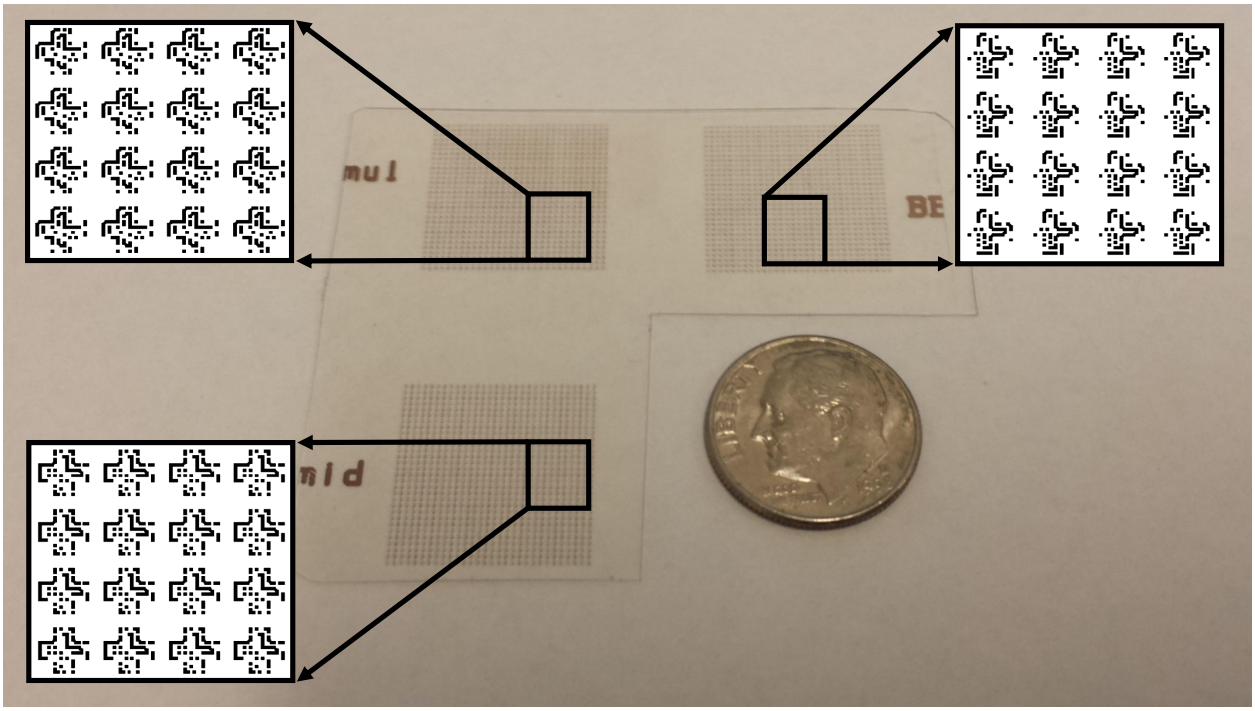

Figure 4.19 Fabricated filter samples.

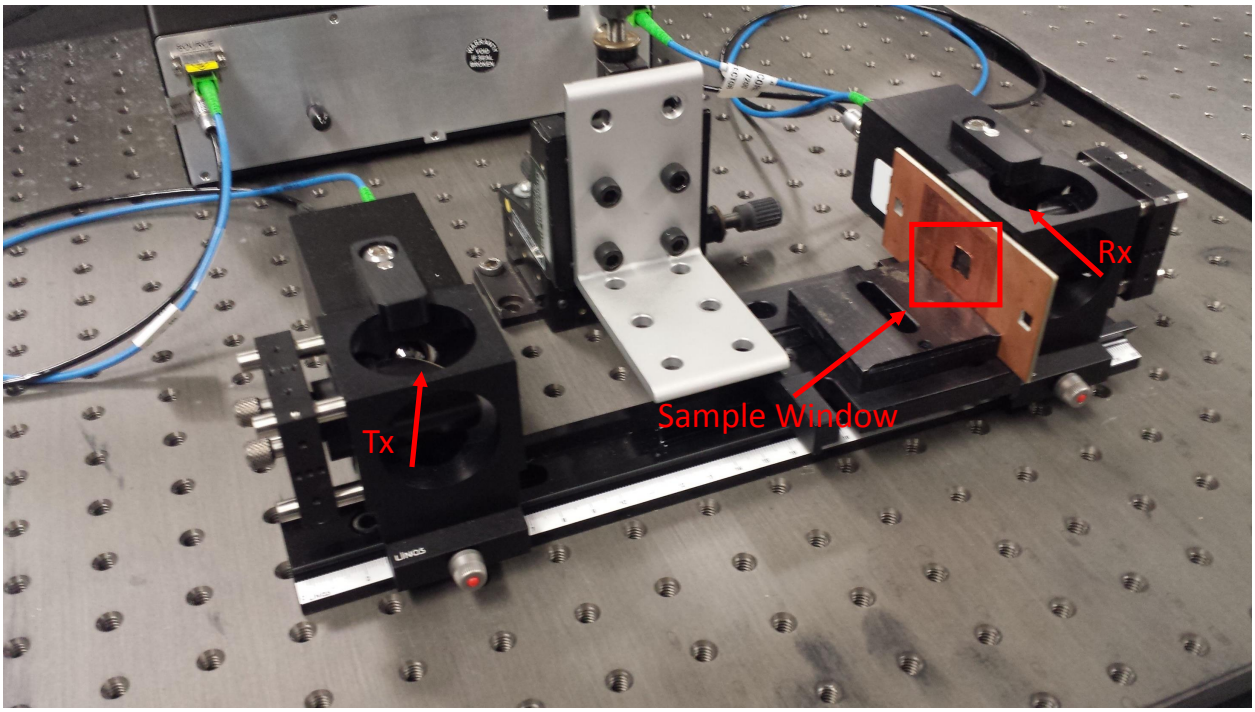

Figure 4.20 THz measurement setup used for the characterization of filters.

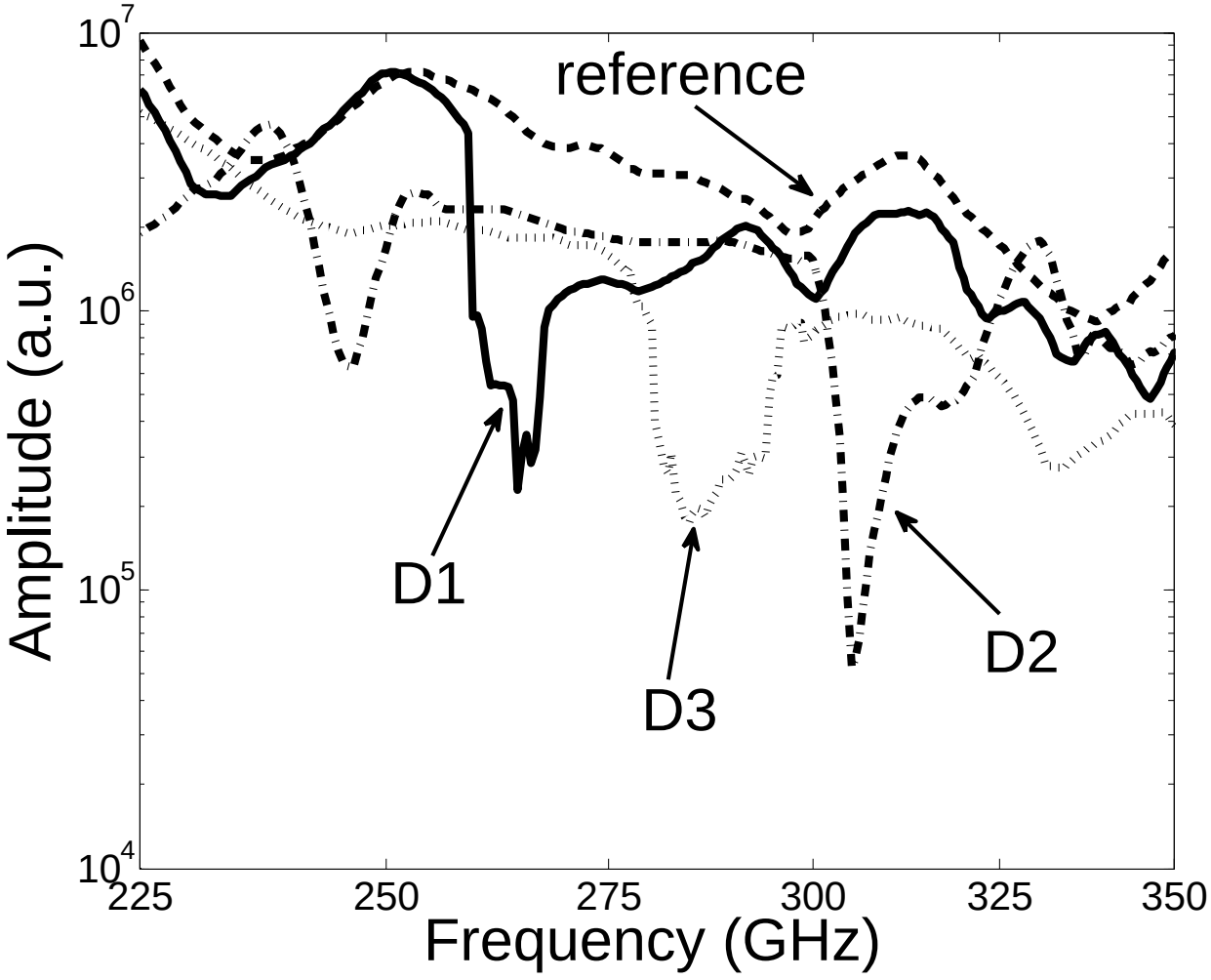

Figure 4.21 Measured filter results.

However, some of the filter designs match better with their simulated counterparts than others. This is most likely due to fabrication tolerances. To improve the fabrication, a thinner top layer metal that is compatible with lift-off techniques could be utilized to achieve precise patterning of the metal structure.

4.7 Error Analysis and Discussion

In this chapter, the errors obtained for the measurements of the filters are not as drastic as the previous chapters, as there is no coupling method necessary between the system and the measured filters. However, the same problems with the THz frequency domain system heating and cooling are relevant here. In addition, the exact alignment between the Tx and Rx heads and the sample is difficult to quantify. Another major contributing factor to the error is the resolution of the patterning. Also, the thickness of the metal is approximately μm and thus the losses are expected to be higher.

4.8 Conclusions and Discussion

In this chapter, multiple THz thin-film components are designed through the use of single and multi-objective evolutionary algorithms. THz band-stop filters are investigated by optimizing the bandwidth and transmission rejection, as well as the multi-resonant properties of the filters. Three filters were fabricated and measured, showing good agreement between the optimized results and measurements. Overall, the optimization process developed in this work is shown to yield efficient integration-compatible THz components with a variety of applications.

CHAPTER 5

Plasmonic-Inspired Periodic Waveguide Structures

5.1 Introduction and Proposed Structures

In this chapter, thin-film metal-backed periodic structures are investigated for the design of integration compatible THz circuit elements. These structures can be designed to have either absorbing properties, or support surface wave propagation, depending on the characteristics of the top-layer metal. If a highly conductive metal is used, the structures are usable in guided-wave applications, with potential to realize many passive THz elements.

5.2 Simulated Response of Several Periodic Structures

To begin, four 2D periodic metal-backed structures are examined in this section. Each resonant structure is modeled with copper, and built on a 50 μm thick dielectric substrate with $\epsilon_r = 3.5$and a dielectric loss tangent of $\delta = 0.01$. Each unti cell is also covered with a solid copper backing. The four periodic structures are shown in Figure 5.1, along with their dimensions in Table 5.1. The periodic structures introduced here can be sorted into two primary groups. The first group consists of two circle structures shown in Figure 5.1 (a) and

(b). This first structure is simply a circle of radius R, while the second is a combination of two circles, one of the same radius as the first along with another of radius R_S. The resonance spectrum for these structures is primarily characterized by multiple, narrow resonances. By including the second circle, the frequency spectrum is expanded from the additional resonances.

The second group consists of the resonant structures of Figure 5.1 (c) and (d), a cross type resonant structure, as well as a Minkowski fractal, which is the geometric compliment of the cross. The frequency spectrum of theses structures are very different from the first group of resonators. As opposed to multiple narrow resonances, these structures provide a single, but wideband frequency spectrum.

Each structure is simulated in a 3D FEM solver (Ansoft HFSS) as a 2D infinitely periodic unit cell with floquet boundary conditions and plane wave incidence. The plane wave is z-directed and TM polarized, and the structure is initially excited at normal incidence. The reflection coefficients are displayed for both types of resonant groups in Figures 5.2 and 5.3.

Due to the metal backing on each unit cell, it would generally be expected that each structure will have all of the incident power reflected. However, it is clear from the reflection coefficients that each structure has a resonance corresponding to a lack of reflection centered around a desired frequency.

Table 5.1 Unit Cell Dimensions

	R (μm)	L (μm)	$x_p(\mu m)$	$y_p(\mu m)$
(a) Circle	400	-	864	864
(b) Circle/Small	400/100	-	864	864
(c) Cross	-	400	354	354
(d) Minkowski	-	114	276	276

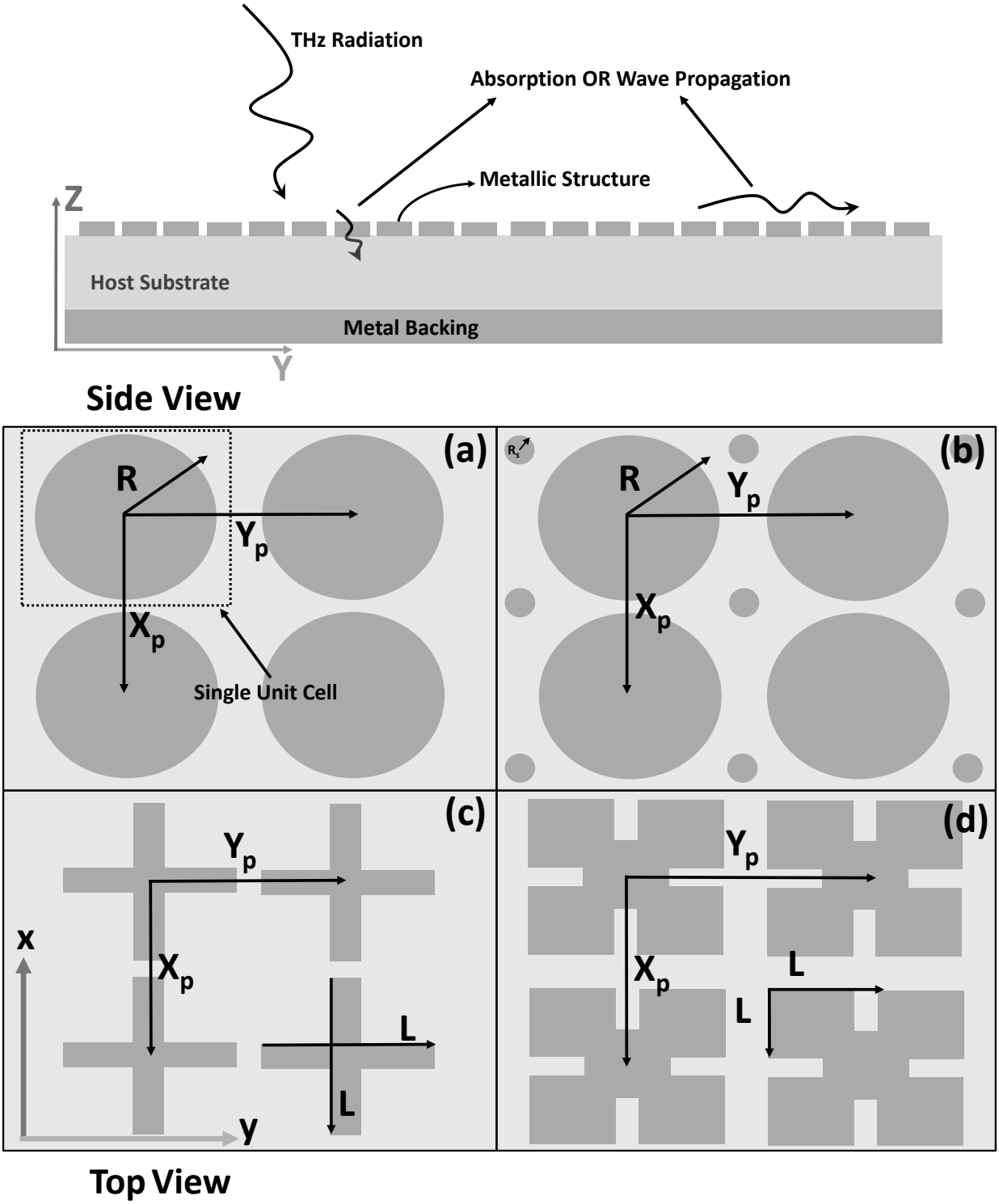

Figure 5.1 Resonant unit cell structures: a) circle structure, b) dual circle structure, c) cross structure, d) minkowski fractal.

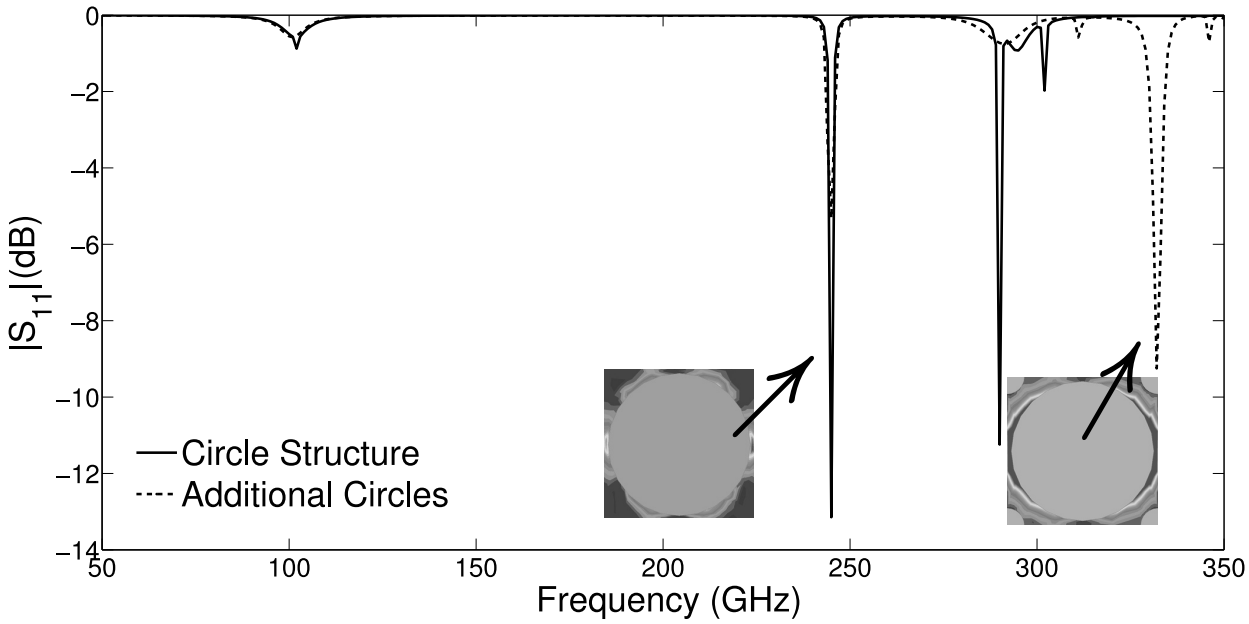

Figure 5.2 Reflection coefficients of circle-type resonant structures.

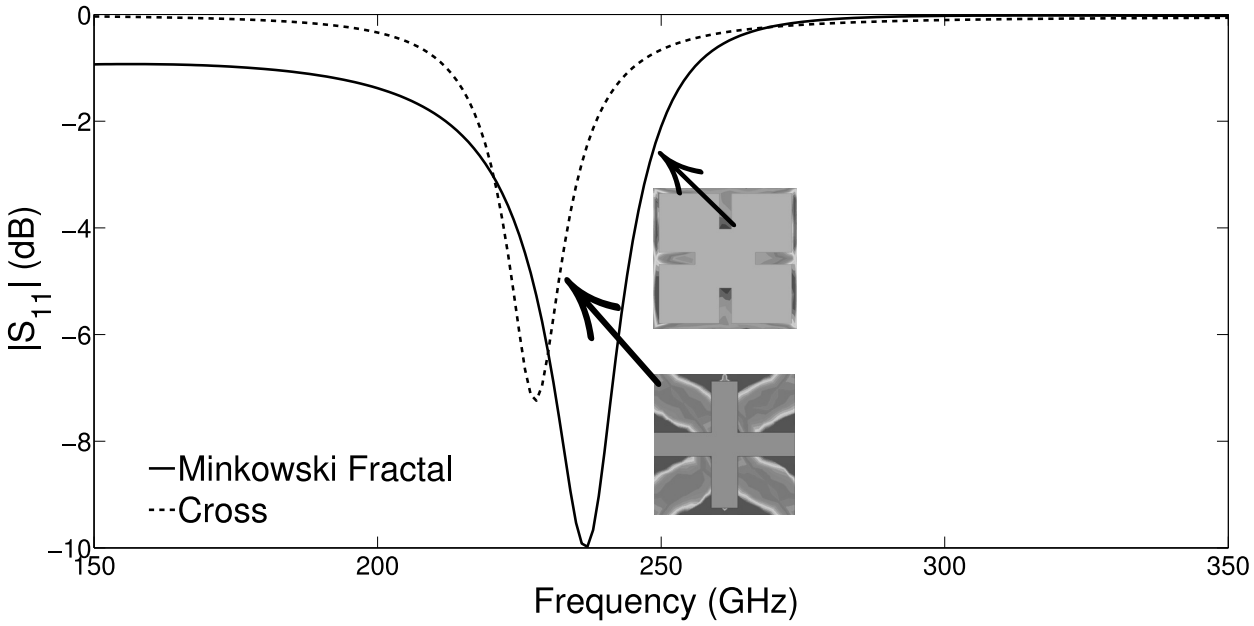

Figure 5.3 Reflection coefficients of cross-type resonant structures.

A number of factors could be assumed to contribute to this effect, such as dielectric loss, absorption, surface wave propagation, or higher order coupling into evanescent modes. While some of the power could be lost in dielectric or other types of losses, a linear loss which increases with frequency would be expected. In this case, it is clear that patterning of the top metal layer changes the characteristics of the reflection coefficient, ruling out traditional loss. In the next section, the characteristics of the floquet mode interaction are studied to determine if higher order evanescent modes are responsible for this phenomena.

5.3 Theoretical Floquet Mode Analysis

A theoretical floquet expansion can be applied to determine the overall characteristics of the coupling into the periodic structures at the frequencies where the reflection coefficients display a resonance. When a time harmonic plane wave is obliquely incident on a 2D periodic structure with periodicity x_p and y_p, the scattered electric field can be written as:

$$\vec{E}^s(x,y,z) = \vec{E}^s(x+x_p,y,z)e^{jk_x^i x_p}, \text{x-direction} \tag{5.1}$$

$$\vec{E}^s(x,y,z) = \vec{E}^s(x,y+y_p,z)e^{jk_y^i y_p}, \text{y-direction} \tag{5.2}$$

where the wavenumbers of the incident wave in each direction are

$$k_x^i = -k_0 \sin\theta_i \cos\phi_i, k_y^i = -k_0 \sin\theta_i \sin\phi_i \tag{5.3}$$

Commonly, a transformed field variables is then introduced [116] which is periodic in both x and y with periodicity x_p and y_p, respectively.

$$\vec{E}^s(x,y,z) = \vec{P}^s(x,y,z)e^{-j(k_x^i x + k_y^i y)} \tag{5.4}$$

substituting this into (5.1) yields

$$\vec{P}^s(x,y,z) = \vec{P}^s(x+x_p,y,z), \text{x-direction} \tag{5.5}$$

$$\vec{P}^s(x,y,z) = \vec{P}^s(x,y+y_p,z), \text{x-direction} \tag{5.6}$$

The transformed field variable can then be expanded as a summation of plane waves as a Fourier series.

$$\vec{P}^s(x,y,z) = \sum_{m=-\infty}^{\infty}\sum_{n=-\infty}^{\infty} \vec{A}_{mn}(w) e^{-j[(\frac{2\pi m}{x_p})x+(\frac{2\pi n}{y_p})y]} \tag{5.7}$$

where the modal expansion coefficients are given by equation 8.

$$\vec{A}_{mn}(\omega) = \frac{1}{x_p y_p}\int_0^{x_p}\int_0^{y_p} \vec{P}^s(x,y,z) e^{-j[(\frac{2\pi m}{x_p})x+(\frac{2\pi n}{y_p})y]} dxdy \tag{5.8}$$

The cutoff frequency, k_{zmn}, for a given mode is defined as the frequency at which mode began to propagate, where any frequency below the cutoff is evanescent. The cutoff frequency can be found from the wavenumbers in the x- and y-directions:

$$k_{xm} = (\frac{2\pi m}{x_p}) - k_0 \sin\theta_i \cos\phi_i \tag{5.9}$$

$$k_{yn} = (\frac{2\pi n}{y_p}) - k_0 \sin\theta_i \sin\phi_i \tag{5.10}$$

the cutoff frequency is then given by the following relation.

$$k_{zmn} = \begin{cases} \sqrt{k_0^2 - k_{xm}^2 - k_{yn}^2}, & \text{propagating waves} \\ \sqrt{k_{xm}^2 + k_{yn}^2 - k_0^2}, & \text{evanescent waves} \end{cases} \tag{5.11}$$

However, for the case of normal incidence, it can easily be shown that

Table 5.2 Cutoff Frequencies

k_{zmn}	01	10	11	02	20	21	12
Circle (GHz)	346	346	490	693	693	775	775
Dual Circle (GHz)	346	346	490	693	693	775	775
Cross (THz)	1.08	1.08	1.53	2.17	2.17	2.42	2.42
Minkowski (THz)	.846	.846	1.19	1.69	1.69	1.89	1.89

Table 5.3 Modal Coefficients ($\leq 1\%$ not shown)

	A_{mn}	00	01	10	11
Circle	104 GHz	96%			
	251 GHz	95%			
	297 GHz	73%	12%	6%	2%
Dual Circle	104 GHz	96%			
	251 GHz	95%			
	297 GHz	73%	12%	6%	2%
	325 GHz	86%	5%		
Cross	240 GHz	97%			
Minkowski	225 GHz	82%	7%		

$$\vec{P}^s(x,y,z) = \vec{E}^s(x,y,z) \tag{5.12}$$

and

$$\vec{A}_{mn}(\omega) = \frac{1}{x_p y_p} \int_0^{x_p} \int_0^{y_p} \vec{E}^s(x,y,z) e^{-j[(\frac{2\pi m}{x_p})x + (\frac{2\pi n}{y_p})y]} dxdy \tag{5.13}$$

where the wavenumbers also simplify to the following.

$$k_{xm} = (\frac{2\pi m}{x_p}), k_{yn} = (\frac{2\pi n}{y_p}) \tag{5.14}$$

It is interesting to note that the cutoff frequencies produced by a normally incident plane wave only depend on the periodicity of the unit cell, and none of the geometric properties of the structure contained within. The modal coefficients, however, depend on the scattered electric field, which is primarily produced by the geometry of the structure itself.

The cutoff frequencies are first calculated using the unit cell dimensions and equation 11, and are summarized in Table 5.2. The circle resonators have the same cutoff frequency for the fundamental mode at approximately 346 GHz. The cross and Minkowski fractal have much higher fundamental cutoff frequencies, at 1.08 and .846 THz, respectively. Any modes contributing below these frequencies outside of the fundamental mode will be evanescent modes.

The modal coefficients are found by sampling the scattered electric field on a plane approximately one wavelength from each infinitely periodic structure using equation 13. As they are frequency dependent, the modal coefficients are examined at each resonance in the frequency spectra of each structure. These coefficients are shown in Table 5.3, in terms of the percentage of total contribution to the plane wave coupling into the periodic structure. The behavior of the coupling at the frequencies of interest for each structure are shown to primarily be caused by fundamental floquet mode interactions. The frequencies of interest in all of the structures are significantly lower than the cutoff frequencies of any of the higher order modes, and the modal coefficients show little coupling into the higher order modes. Therefore, it is concluded that very little of the energy is lost in higher order evanescent floquet modes. This leaves the two primary explanations for this phenomena as absorption, or a surface wave phenomena. In the following sections, it will be shown that based on the conductive properties of the metal, these structures can be tailored to act as either absorbers, or surface wave interconnects, each with multiple applications in THz integrated circuits.

5.4 Linear Waveguide Analysis

While the previous analysis concerned only infinitely periodic structures, the real world waveguides and devices that will be constructed using the unit cells will of course be finite. The overall design methodology for the plasmonic THz waveguides is shown in Figure 5.4. First, as shown in the previous sections, a desired unit cell is chosen an analyzed with 2D

periodic boundary conditions. Now that the resonances of the individual unit cells are known, the unit cell is expanded into a finite array. A waveguide can then be made by reducing the periodicity in one direction, allowing for propagation along the other. The analysis and justification of a finite array and the transition to a variety of waveguides is presented in the following sections.

5.4.1 Array

First, the circle unit cell is expanded in both directions as a 5x5 array. A TM polarized plane wave is used to excite the array in HFSS with a transverse incident angle (along the y-axis). The power flow in each direction is calculated using Equation 5.16 over a vertical plane in the desired direction.

$$\vec{P}(\omega) = \int_0^{5xp} \int_0^{5yp} \vec{E}^s(x,y,z) \times \vec{H}^s(x,y,z) dxdy \tag{5.15}$$

Figure 5.5 shows the power flow in both the x- and y-directions. As expected,the frequency spectrum of the power flow in each direction matches well with the resonances of the individual unit cells. In addition, the power flow in both directions is very similar. However, if the array is reduced in one direction, then the power flow can be increased in the other. Figure 5.6 compares the power flow in the y-direction for the 5x5 array, and an array where the x-direction is reduced to two unit cells. The frequency spectrum for both arrays matches very well, while the power flow in the y-direction of the 5x2 array is approximately double

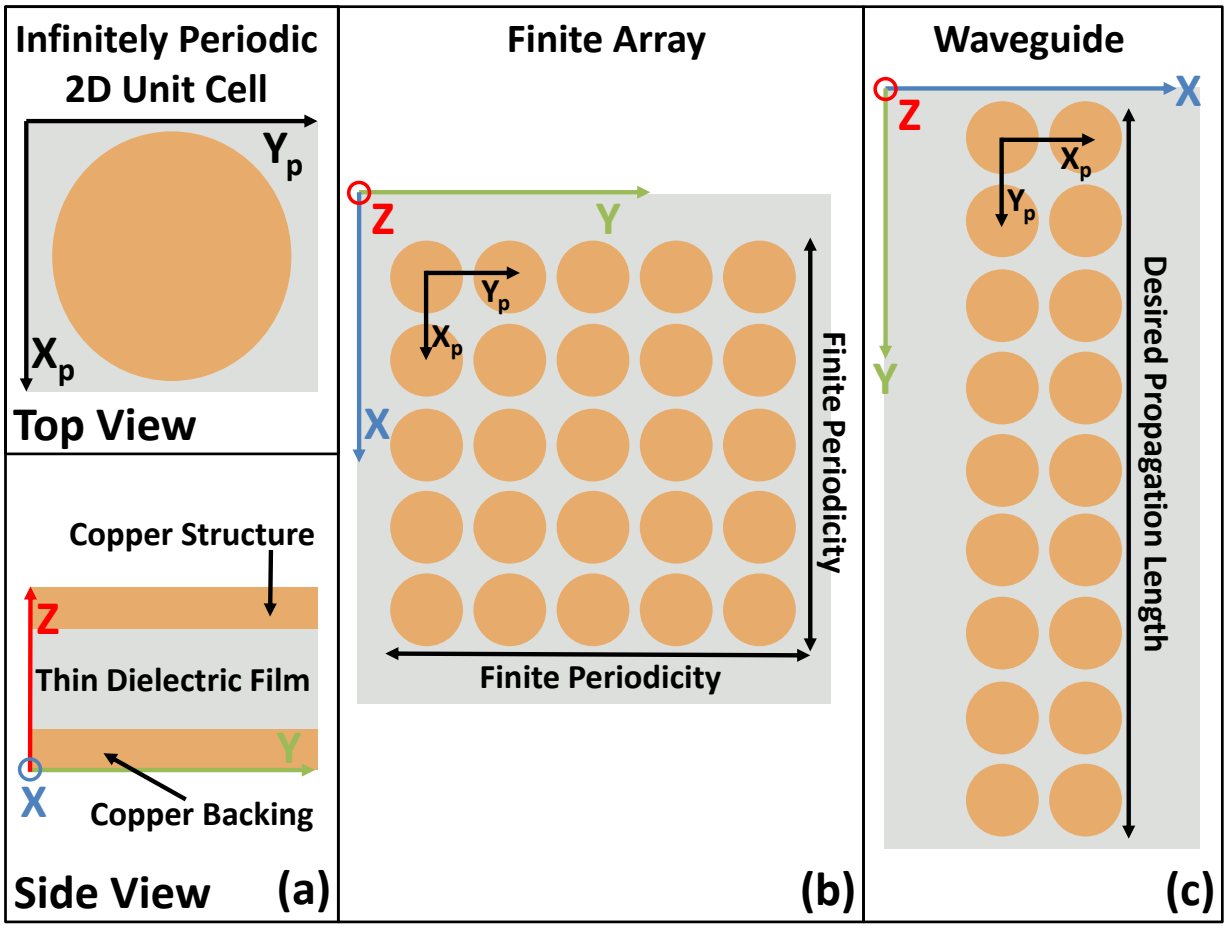

Figure 5.4 Design process of plasmonic waveguides, progressing through (a) periodic unit cell, (b) finite array, and finally (c) waveguide.

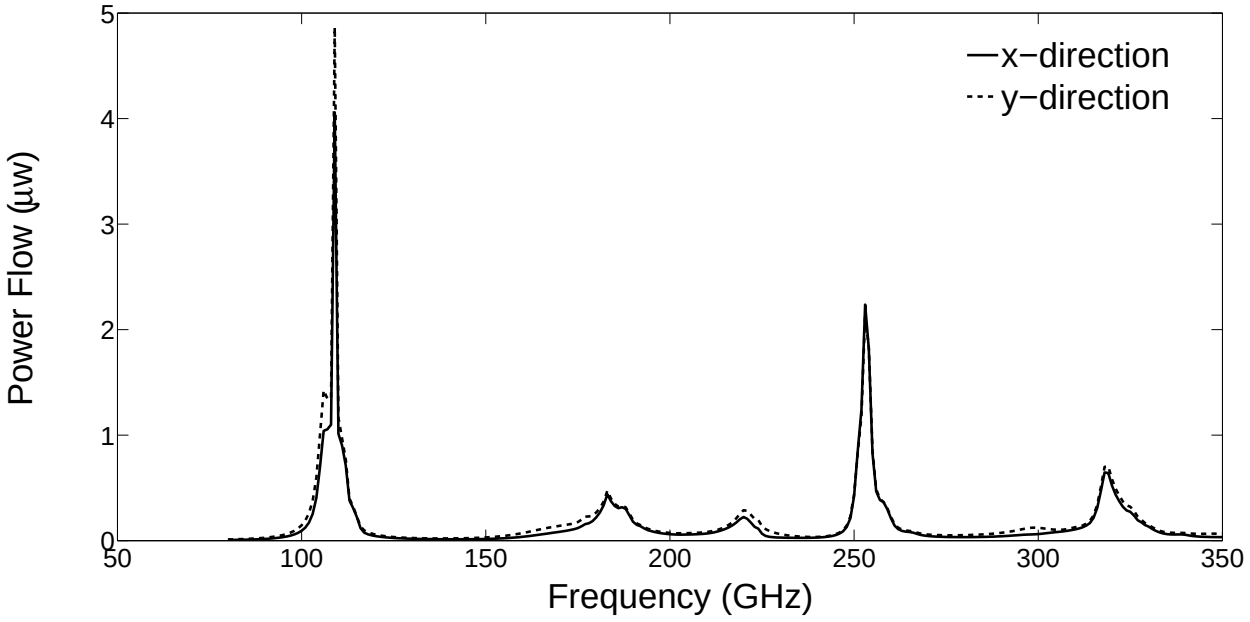

Figure 5.5 Power flow in both the x- and y-directions along the array.

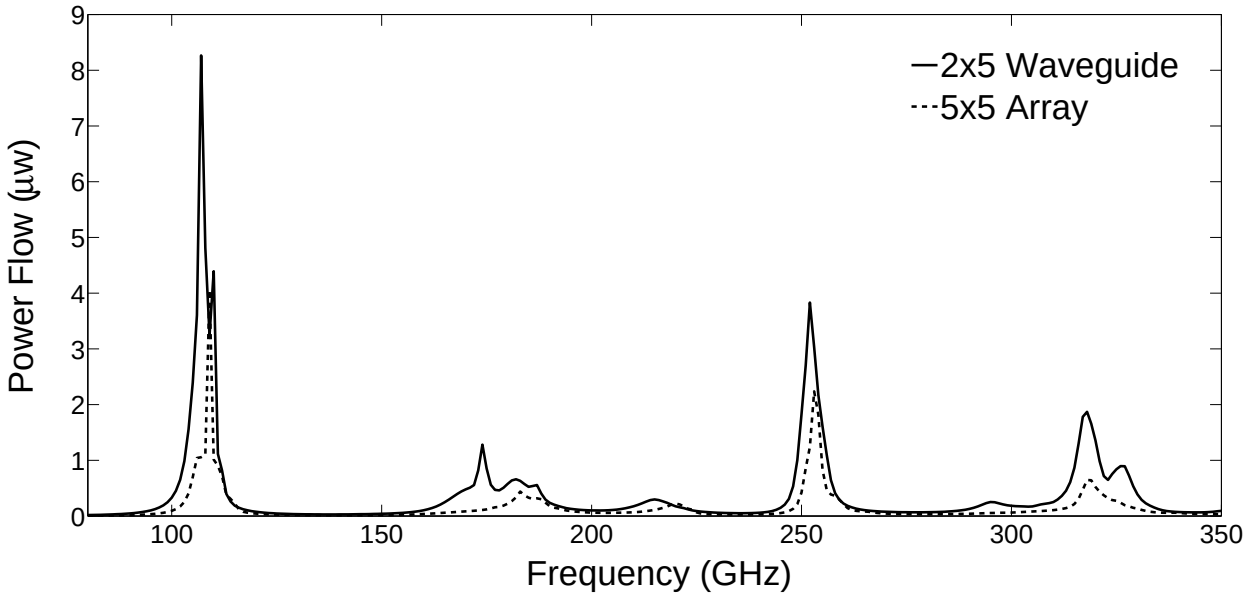

Figure 5.6 Comparison of power flow in the y-direction of 2x5 and 5x5 circle arrays.

that of the 5x5 array.

5.4.2 Terahertz Waveguides

While the previous analysis concerned only infinitely periodic structures, this section introduces finite structures based on highly conductive metals. These structures exhibit a surface wave phenomena that can be exploited for a number of THz applications. In this case, the wave propagation is only desired in one direction of the infinite array. Therefore, in the desired direction of wave propagation, the unit cells are expanded to a desired length, with the other direction is minimized to two unit cells in length. Waveguiding structures are made from the four unit cells introduced previously, including the circle, dual circle, minkowski fractal, and cross.

The waveguiding structures are modeled with HFSS, and excited using a TM polarized plane wave, traveling in the longitudinal direction. In this case, a plane wave is used as an excitation to ensure comparable results with the floquet excitations used in the infinitely periodic analysis. However, with plane wave excitation, traditional S-parameters are unavailable. Therefore, to determine the properties of the waveguiding structures, 2D cuts in both the XY and ZY planes are used to sample the power intensity along the surface, as well as the power flow through the waveguide. The power on these planes is calculated using the relationship

$$\vec{P}(\omega) = \int_0^{2xp} \int_0^{Nyp} \vec{E}^s(x,y,z) \times \vec{H}^s(x,y,z) dxdy \tag{5.16}$$

where x_p and y_p are the lengths of a single unit cell in each direction. Figure 5.7 shows the geometry of a sample waveguide, along with the simulation setup. The normalized power flow in the y-direction, as well as the power on the surface of each structures, is shown in Figures 5.8 and 5.9 for all four unit cell types. In this case, each are calculated using equation 15 over each sampling plane.

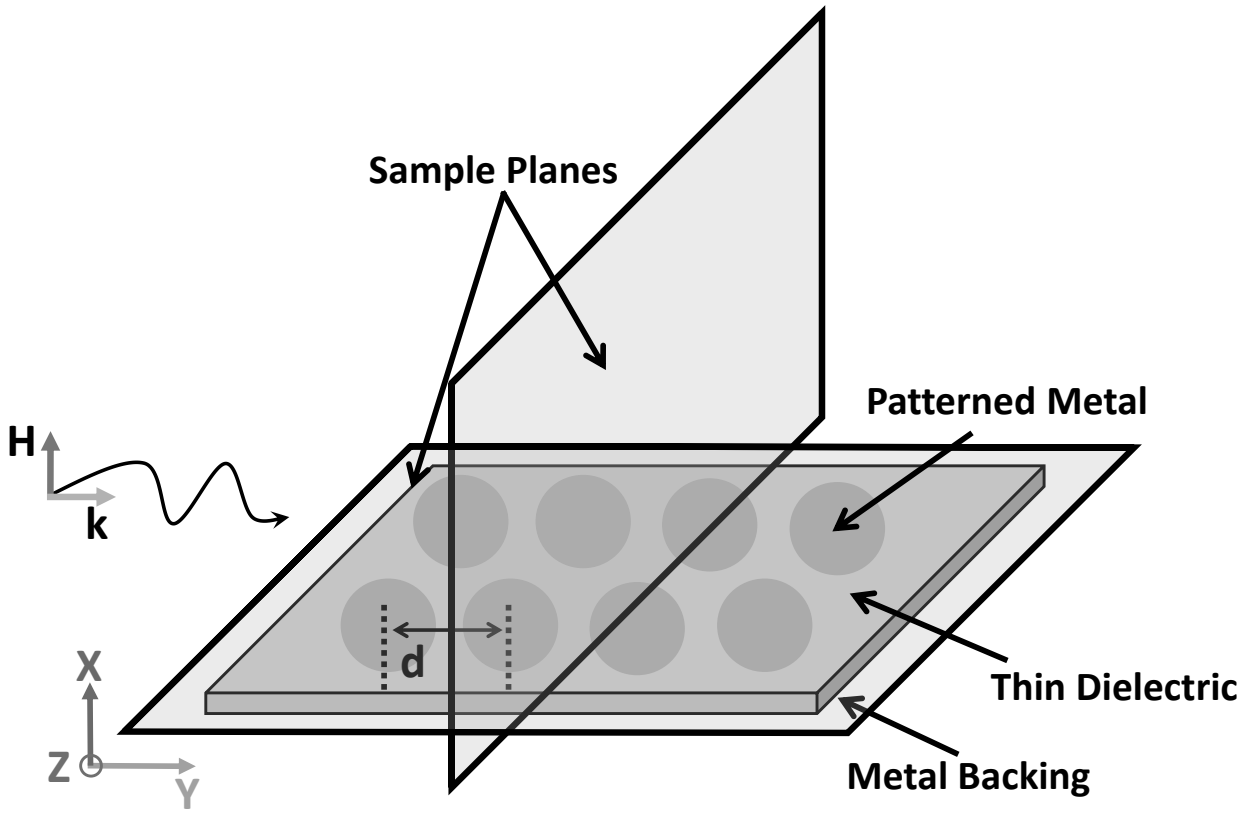

Figure 5.7 Simulation topology and design process of THz waveguides.

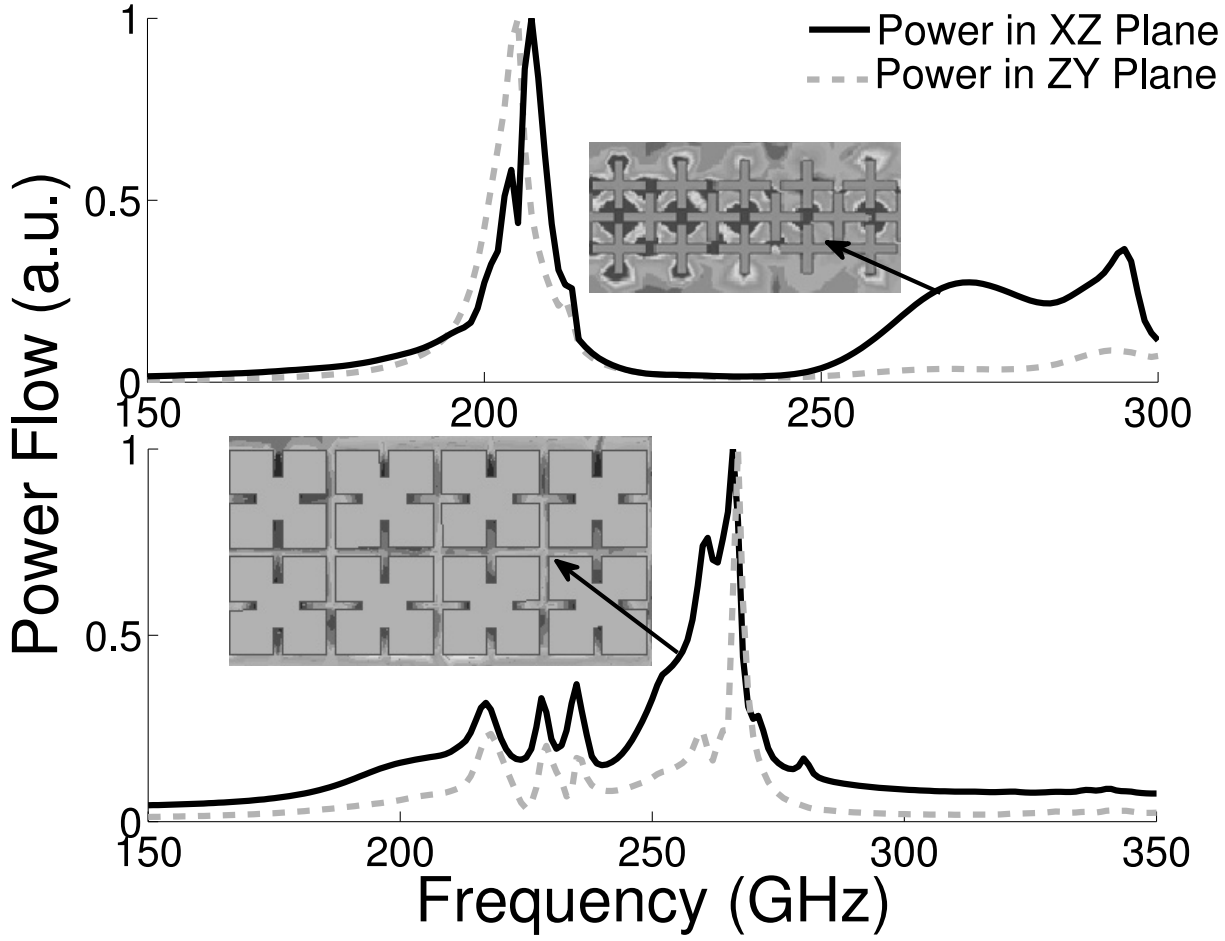

Figure 5.8 Power flow along the surface of the cross and minkowski type waveguides.

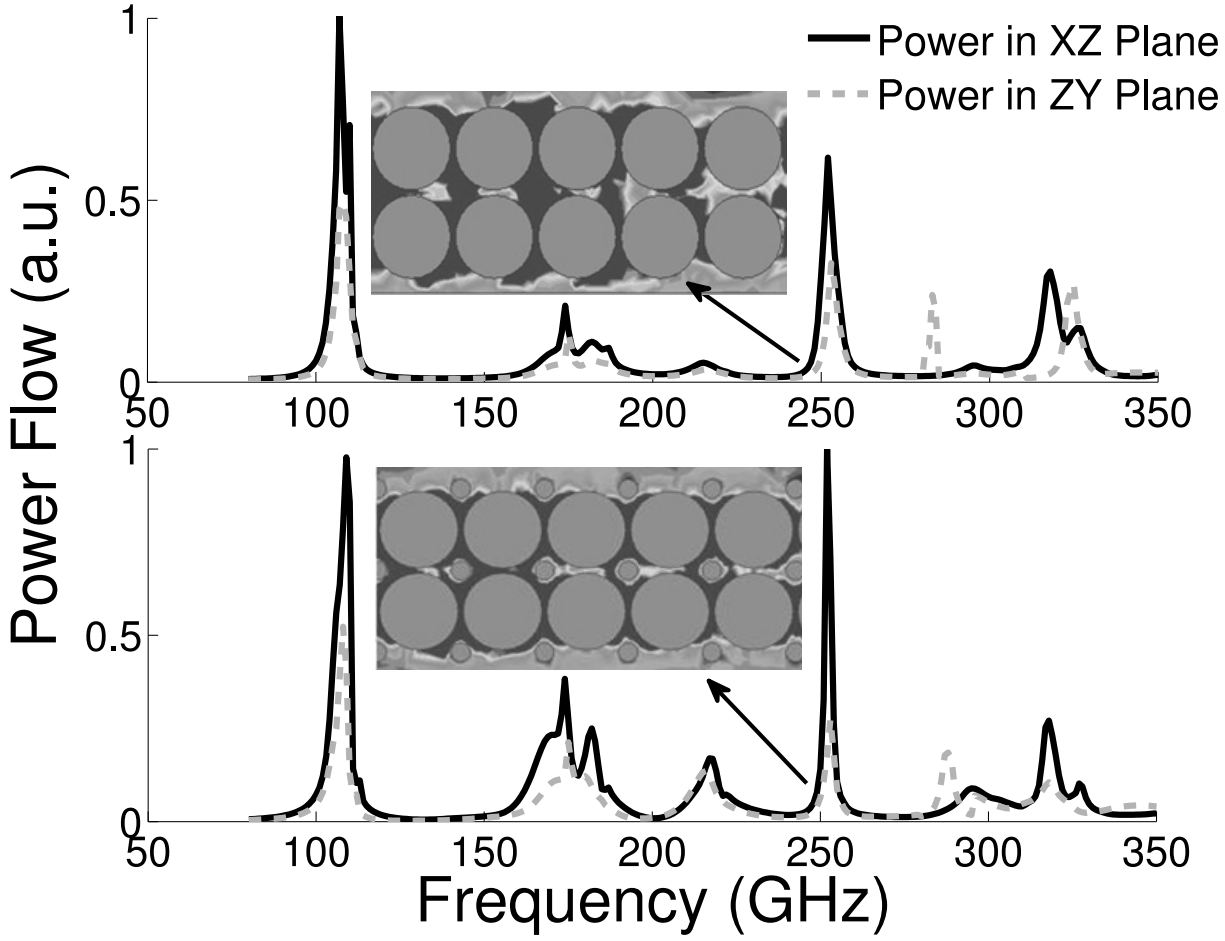

Figure 5.9 Power flow along the surface of the circle structure type waveguides.

For the circle and dual circle structures, the frequency spectrum is similar to what would be expected from the unit cell analysis, multiple narrow band resonant peaks of varying intensity. The cross and Minkowski fractal both display a single, well defined resonance peak, which also matches well with the periodic analysis. However, it is also important to note where the power traveling through the waveguide is primarily concentrated. As mentioned in the previous sections, the coupling of the incident wave into these periodic structures excites a primary propagating mode, which contributes to a surface wave plasmonic like effect if the conductivity of the metal is high enough to limit the absorption.

However, one of the primary characteristics of the plasmonic phenomenon is that the effect occurs at the dielectric and metal interface, while the propagation occurs at the surface of this interface. To investigate the propagation on the surface of these waveguides, the power is sampled along the surface of the metal. The frequency spectrum on the surface of each waveguide is very similar to the transmitted power spectrum through the XZ plane. This shows that nearly all the power is contained at the surface of the metal, as the maximum values of the power sampled are nearly the same.

While the frequency spectrums of the individual unit cells and the waveguides match relatively well, there are some differences in the location and magnitude of the transmitted waveguide resonances and the resonances reflected from the periodic structures. The difference between the infinitely periodic and finite periodic array changes the spectrum slightly, but the change in incident angle is the primary contributor. Figure 5.10 shows the angle dependance of the circle structure for a 2D infinitely periodic unit cell and a finite waveguide. The resonance in both the reflection and power transmission changes both in intensity and location, explaining some of the discrepancies in the results. In addition, at the higher incidence angles the transmission is maximized.

While these interconnects do not display typical waveguide characteristics, such as phase velocity, group velocity, or cutoff frequencies, they do display high levels of power confinement along their surface. Due to the high losses typically associated with metallic waveguides

at THz frequencies, such a phenomena is very desirable in many applications, even though the transmission spectra is relatively narrow band. While other types of THz waveguides may prove to be lower-loss in simple waveguide applications, the proposed structures have potential for many passive THz components that are not realizable with other THz waveguides.

5.5 Applications In Passive Element Design

As a result of the high power confinement along the surface of the waveguides, structures with sharper bends are easier to implement compared with other THz interconnects. Figure 5.11 compares a typical curved structure for a dielectric waveguide (a), traditional plasmonic waveguide (b), and the proposed plasmonic waveguide (c). In the case of the dielectric waveguide, most of the power is lost in the curved portion of the waveguide. However, in the plasmonic waveguide, high power confinement can be shown along the curve and maintained throughout the straight section thereafter. The waveguide made of the periodic circle structure shows similar confinement along the curved portion compared with the traditional THz plasmonic waveguide.

Another important passive THz structure aside from a waveguide is a power splitter. A power splitter contains a waveguide structure with two branches which split the power equally between each branch. The power splitter is made from the circle resonant structure, with the same periodicity and dimensions as the waveguide. Figure 5.11 also shows the electric field confinement for the power splitter at 245 GHz. High field confinement can be seen along the length of the straight portion, as well as in the two branches of the power splitter. Little loss is displayed in the curves that comprise the power splitter, which can be a common problem in conventional THz waveguides [35]. In addition, Figure 5.12 shows the normalized power flow through each section of the power splitter. The power density spectrum is very similar for section (a) and (b), showing that the power is confined evenly

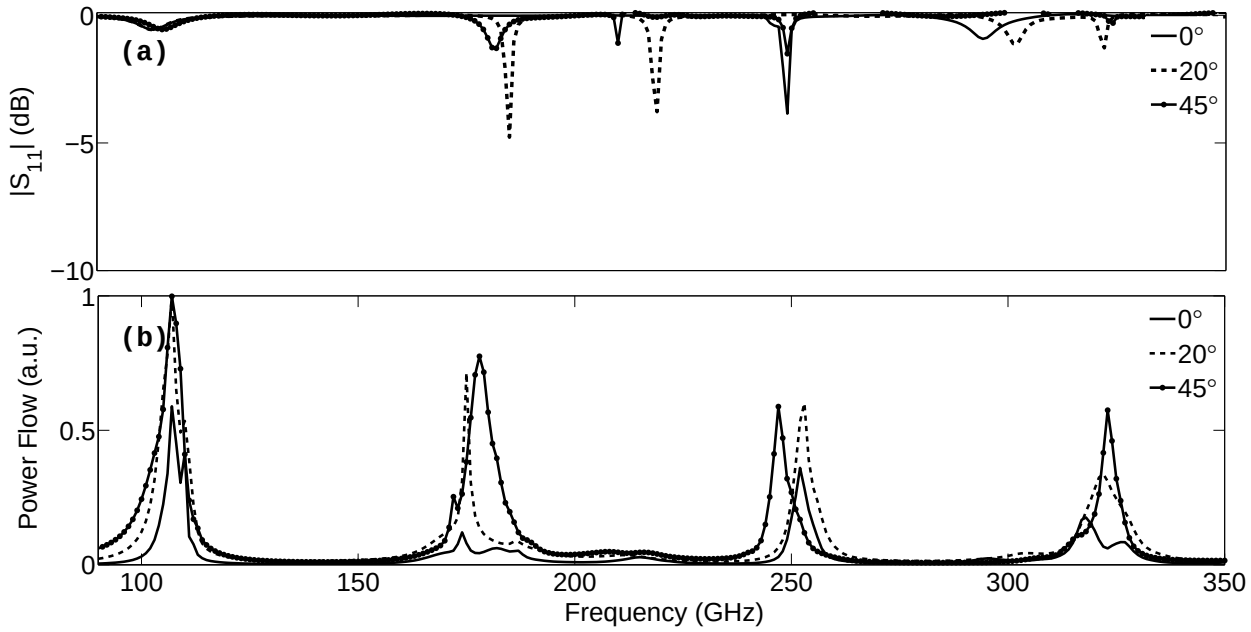

Figure 5.10 Angle dependance in both the (a) reflection coefficient and (b) power flow of the circle type structure.

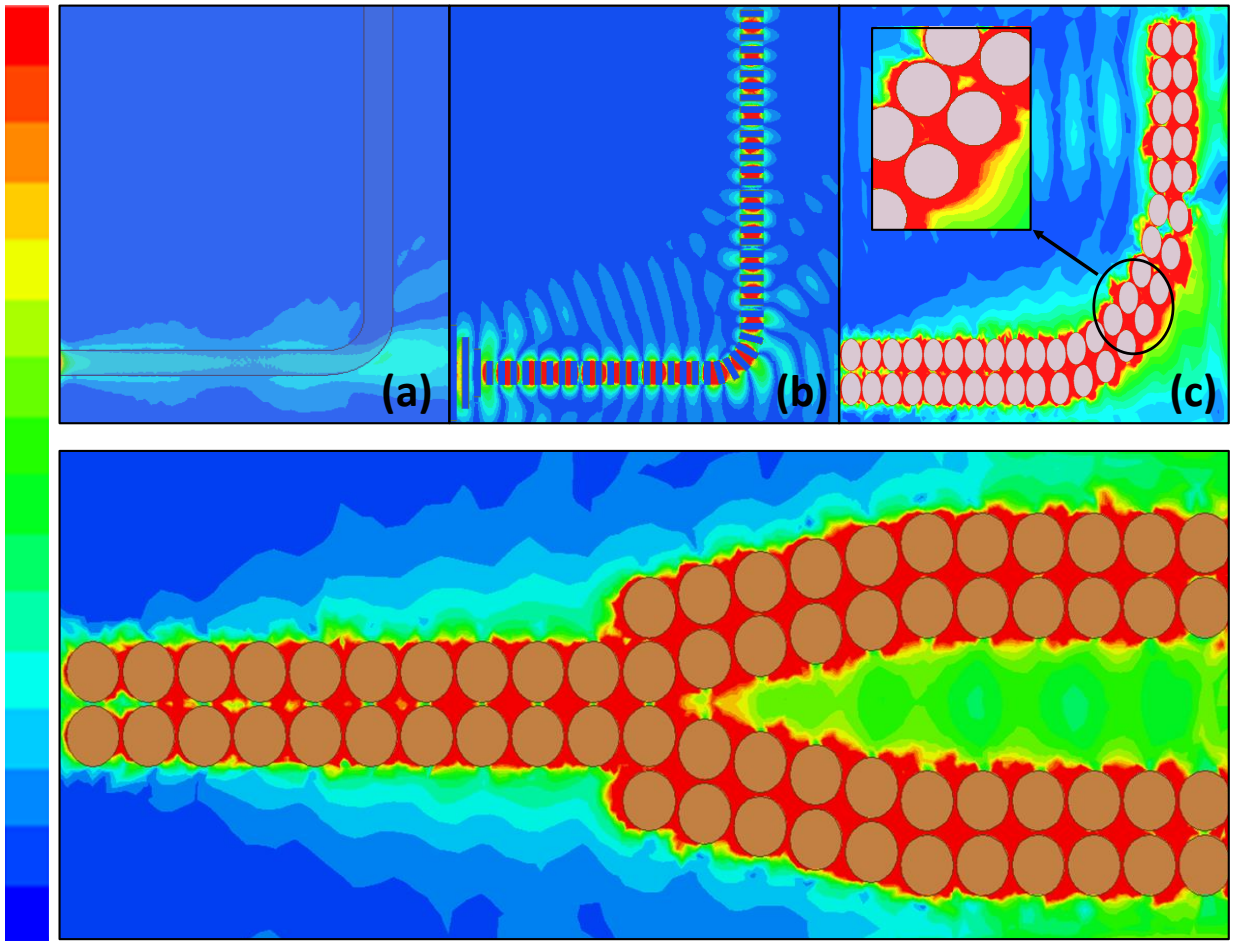

Figure 5.11 Bending in (a) dielectric waveguide at 300 GHz, (b) traditional plasmonic waveguide at 300 GHz, and (c) thin metal based plasmonic waveguide at 297 GHz. Field confinement of a power splitter is also shown.

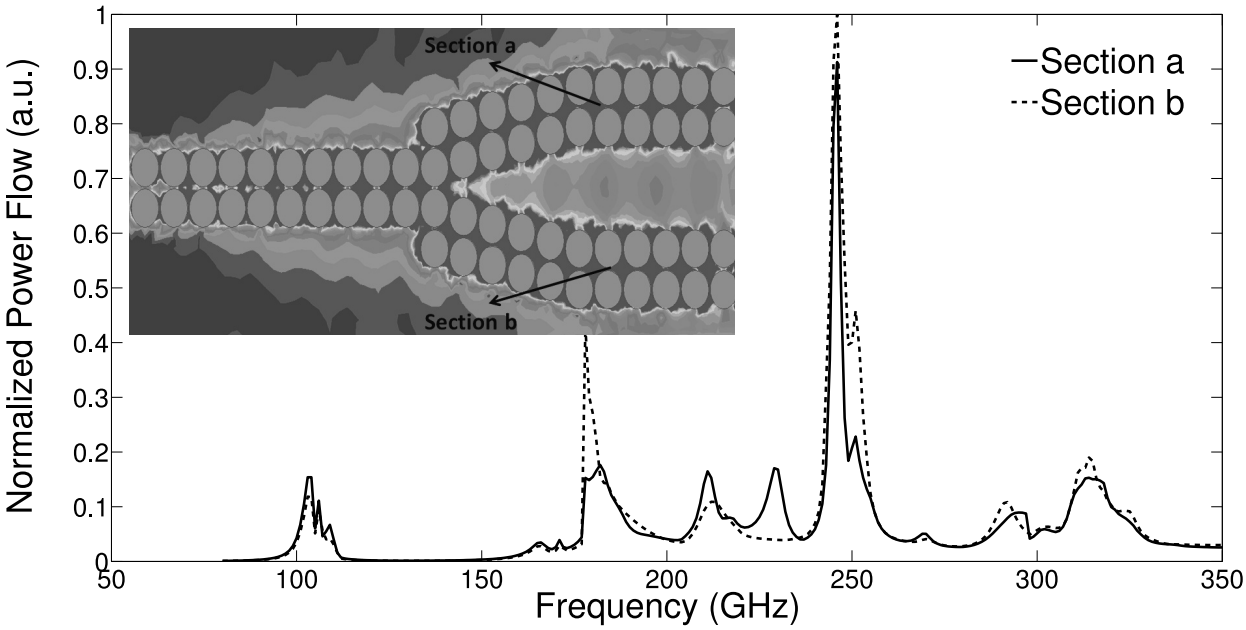

Figure 5.12 Normalized power flow through each section of the power splitter.

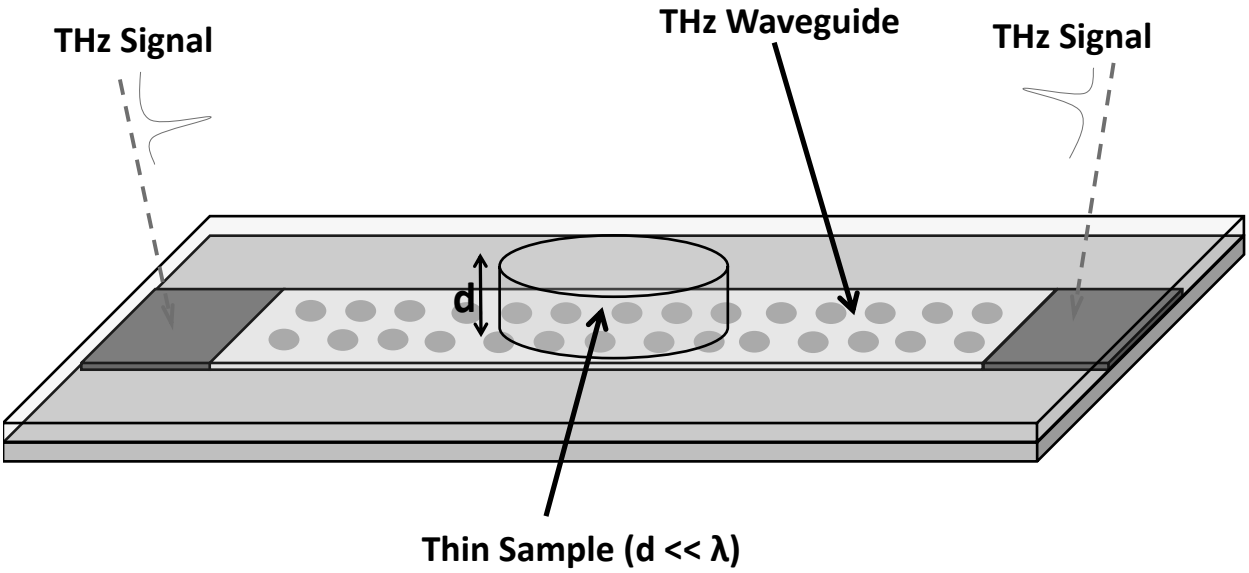

Figure 5.13 Proposed setup of thin-sample dielectric sensor.

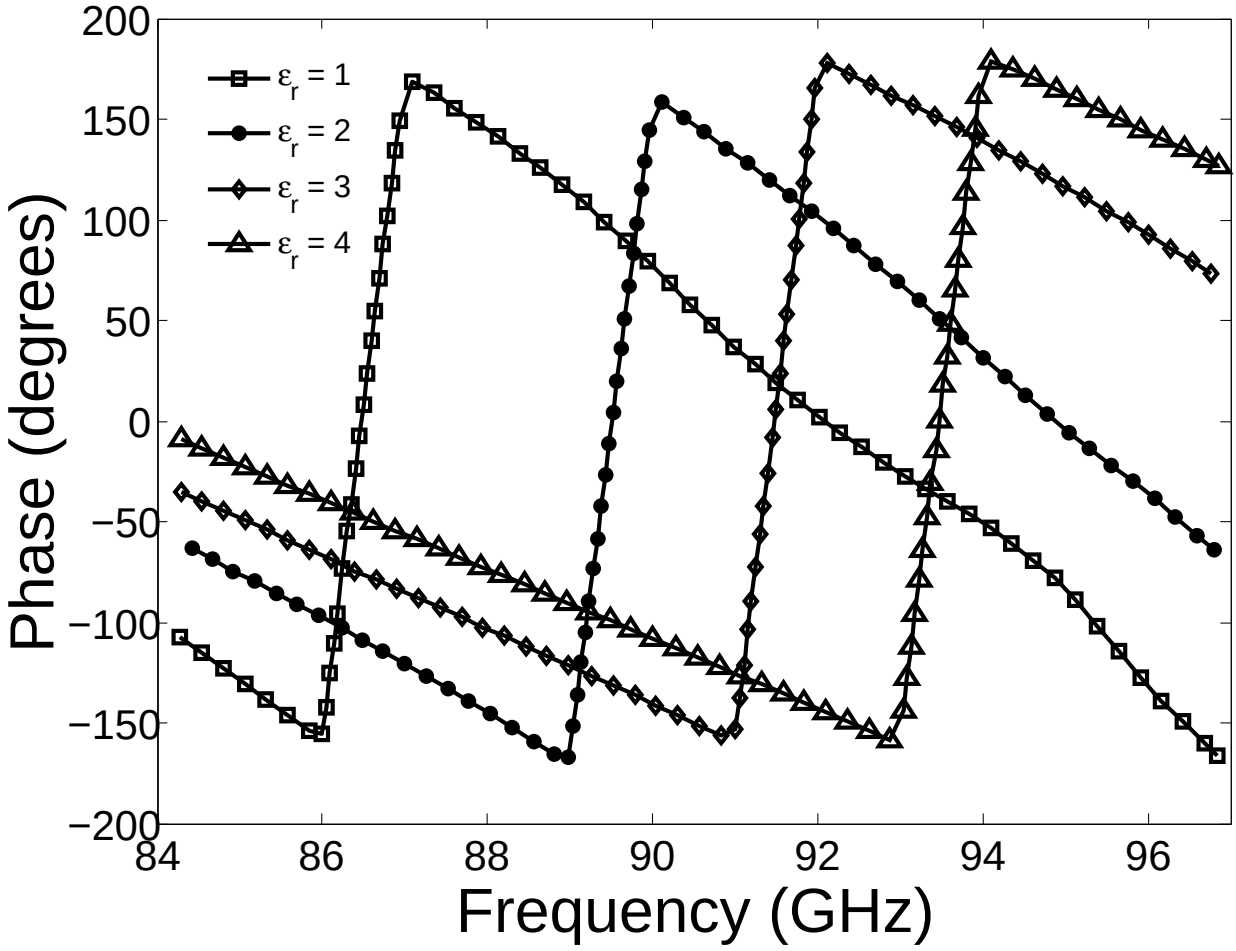

Figure 5.14 Simulated change in phase of transmission though a circle type waveguide with varying sample dielectric constant.

between both sections of the splitter.

Due to the high field confinement along the surface of these structures, they also can be used to develop highly accurate sensors. Figure 5.13 shows the proposed setup of the sensor. In this case, a thin sample that is much less than a wavelength is placed along the length of a waveguiding structure. As the fields are confined very close to the surface, small sample sizes can be easily detected. Figure 5.14 shows the simulated phase of the transmitted signal through the waveguide, with a dielectric sample approximately $\lambda_0/30$ is size placed in the center of the structure. Clearly, when the dielectric constant of the sample is varied, a noticeable change in the phase through the structure is observed.

5.6 Frequency Tailorable Structures

While the previous analysis has been primarily applied to simple FSS-based structures, more complex geometries can also be exploited to enhance the properties of the waveguides. Figure 5.15 shows a simple circle based resonant structure that is modified by cutting out pieces of the circle. The frequency response of each structure is shown in Figure 5.16. Clearly, as the structure is further divided, the number of resonances in the frequency spectrum is increased.

These results show that certain desired characteristics of the unit cells that can be used to create the waveguides and other devices. This is particularly useful in the case of the above designed waveguides, as their application is limited if the only operational band is small in bandwidth. In addition, only the copper structure is needed to be modified, as the unit cell size and materials are unchanged. A similar topology optimization approach that was presented in the previous chapter can therefore be applied to these structures as well.

Figure 5.17 shows a proposed topology for the optimization process. In this case, 5 concentric circles of 50 thickness are separated into 20 slices. In this case, the structures are made of the same PET material and fully backed with copper. The slices of each circle are

controlled with a simple binary GA, with 100 on/off states, and 2^{100} total combinations. The entire geometry of one unit cell is shown in Figure 5.18, with a sample topology found through the GA shown as well.

For an initial test of concept, the GA is used to simply optimize the location of resonances in the reflection coefficient of the structures. Two sample locations are selected, one at 120 GHz, and another at 275. Two separate GA optimization simulations are then performed to find the optimally lowest reflection coefficient at the desired frequencies.

Figure 5.19 shows two possible topologies found with the GA for optimal resonance in the reflection coefficient at 120 and 275 GHz. In this case, reflection coefficients of -17.9 dB and -15.8 dB are found for 120 and 275 GHz from each structure, left to right. The frequency response of the reflection coefficient for both structures is also shown in Figure 5.20.

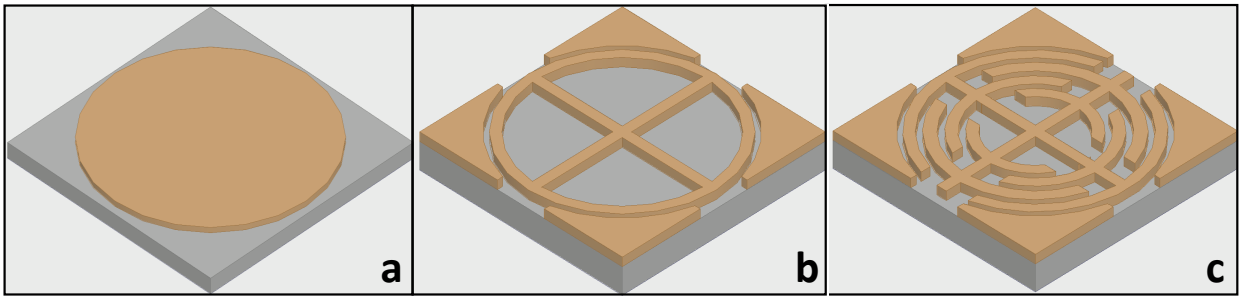

Figure 5.15 Geometry of (a) basic circle structure, (b) circle structure with holes (c) circle structure with more holes.

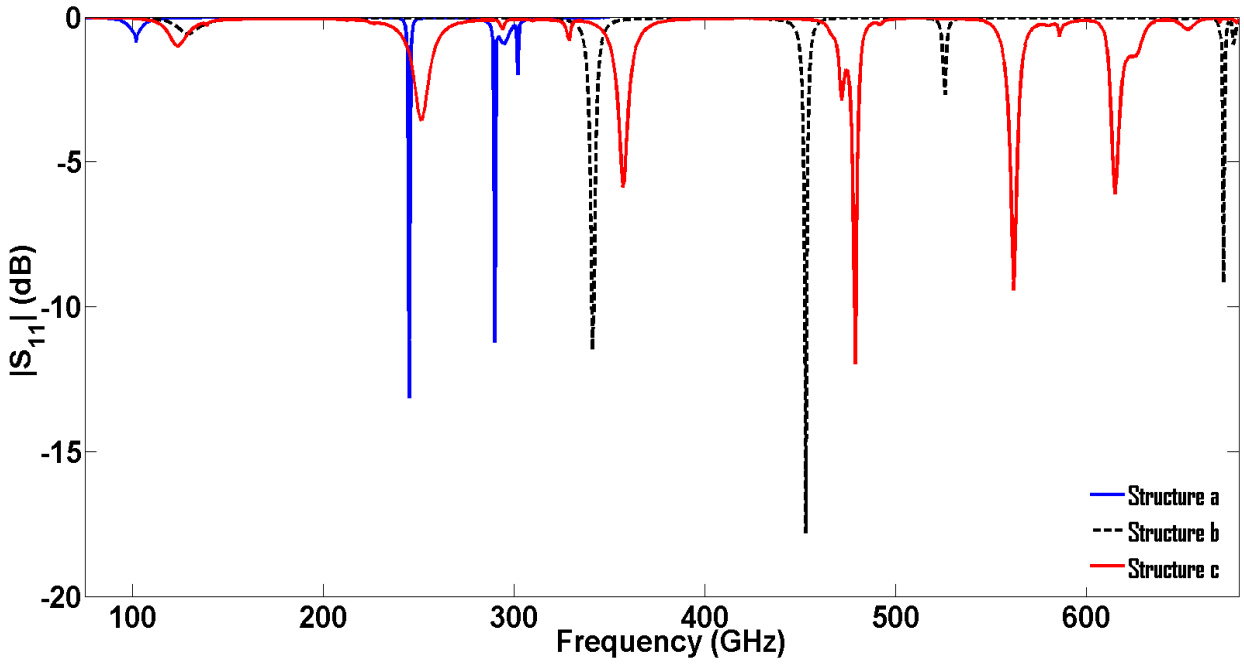

Figure 5.16 Reflection coefficients of the structures introduced in 5.15.

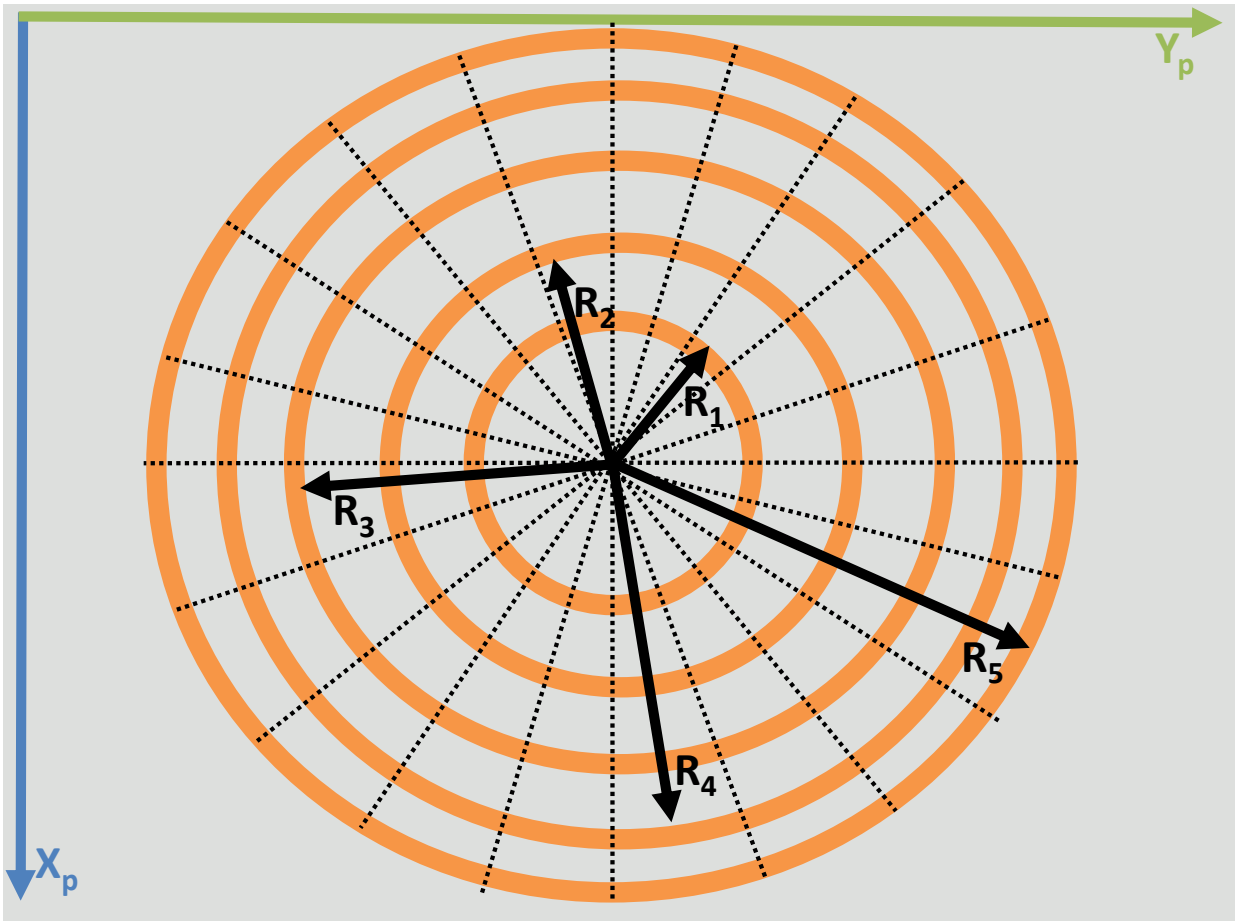

Figure 5.17 Proposed structure for optimization.

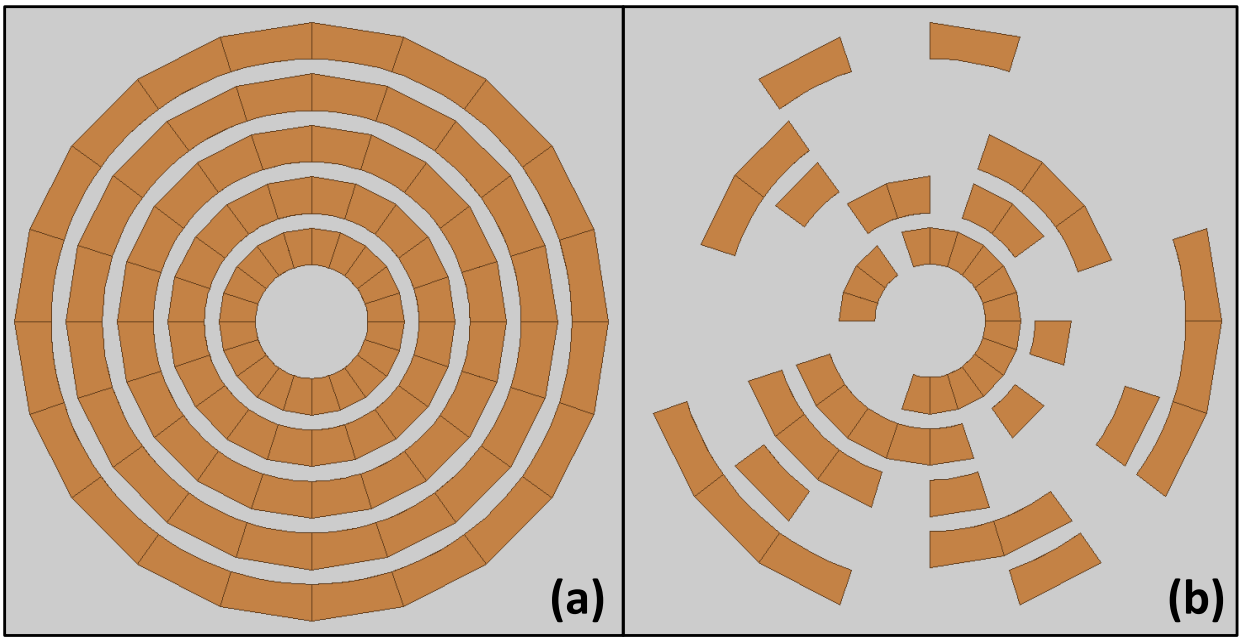

Figure 5.18 Simulated structure with (a) all pixels on and (b) a selected example of one topology after optimization

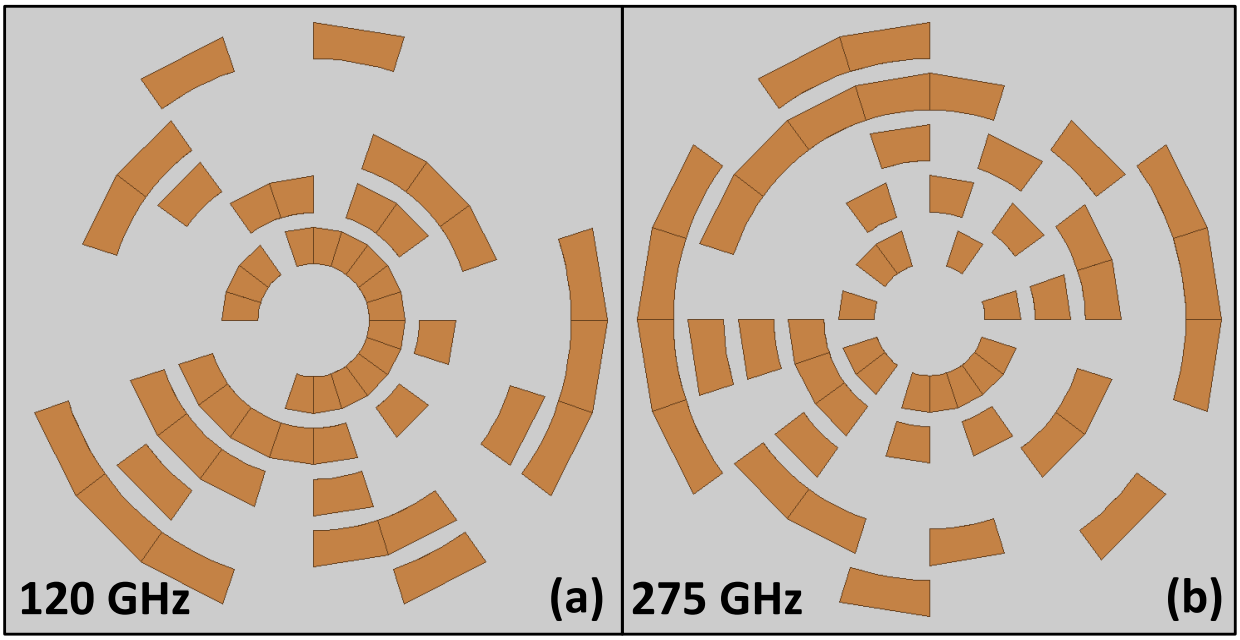

Figure 5.19 Two optimized structures with resonances at (a) 120 GHz, and (b) 275 GHz.

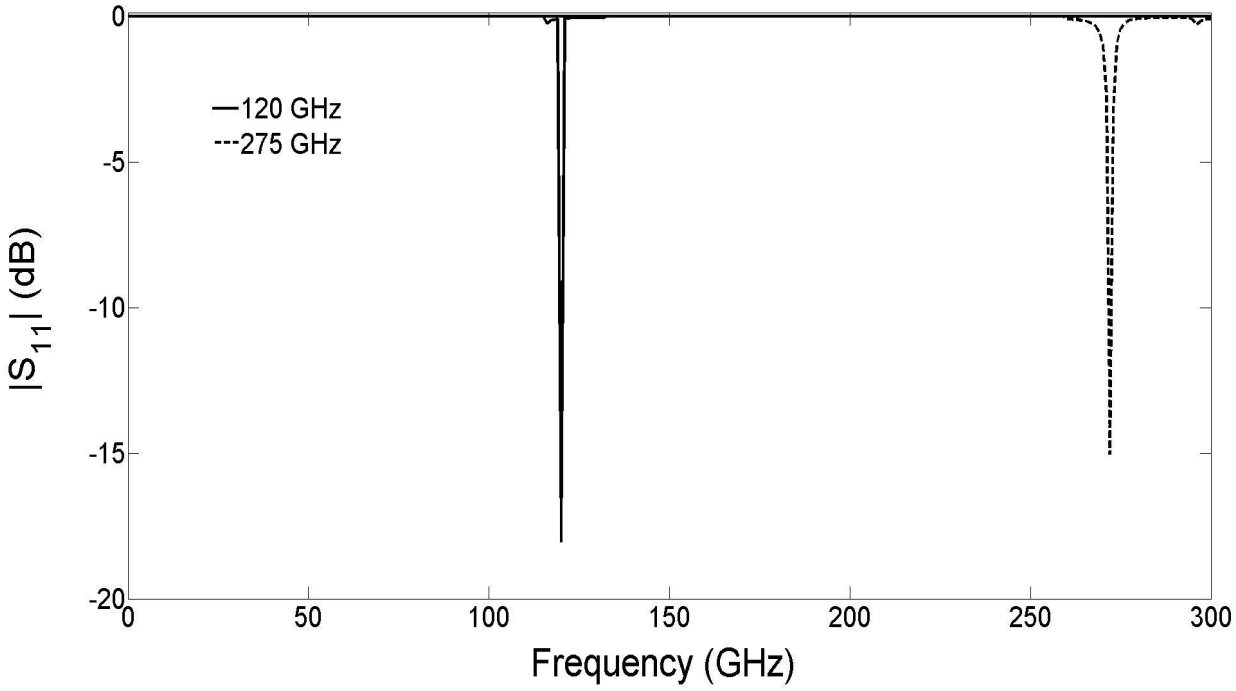

Figure 5.20 Reflection coefficient of structures presented in 5.19.

5.7 Fabrication and Measurement Results

5.7.1 Fabrication Method

Two circuits were fabricated, a straight guided-wave structure and a power splitter, both from the circle type resonant structures. These samples were fabricated on a 50μm thick piece of Rogers 3850 LCP film, both sides backed with copper. The substrate properties in the desired frequency range are as follows: $\epsilon_r = 3.5$, dielectric loss tangent $\delta = 0.01$, and Cu thickness of 17 μm [117]. The copper is retained on the backside, while the top side is patterned using conventional micro-fabrication processes. A simple photo-lithography and wet etching process is used to pattern the top-layer metal.

5.7.2 Measured Results

The fabricated structures are measured with two separate THz measurement systems to ensure repeatable results. First, the waveguide and power splitter are measured using a Picometrix T-Ray 2000 time-domain THz test setup. With this system, THz waves are generated using a photo conductive switch and a femtosecond laser. The system is coupled with THz optics to produce a linearly polarized and collimated beam, and has both a transmitter (Tx) and receiver (Rx) that can be easily adjusted. However, once the time-domain signal is transformed into the frequency domain, the maximum step resolution is approximately 12 GHz, making it difficult to measure narrow band devices. The other measurement system used is a Emcore PB-7200 frequency domain setup. The frequency domain system is capable of measuring very narrow band structures, with a frequency resolution as low as 10 MHz. This system also has both a transmitter (Tx) and receiver (Rx) coupled with fiber optics. Dielectric focusing probes are used to couple the THz radiation from the Tx and Rx heads to the structures, as proposed in chapter 2. The probes as well as the fabricated circuits are shown in Figure 5.21. The measurement setup of the waveguide with the probes is shown in

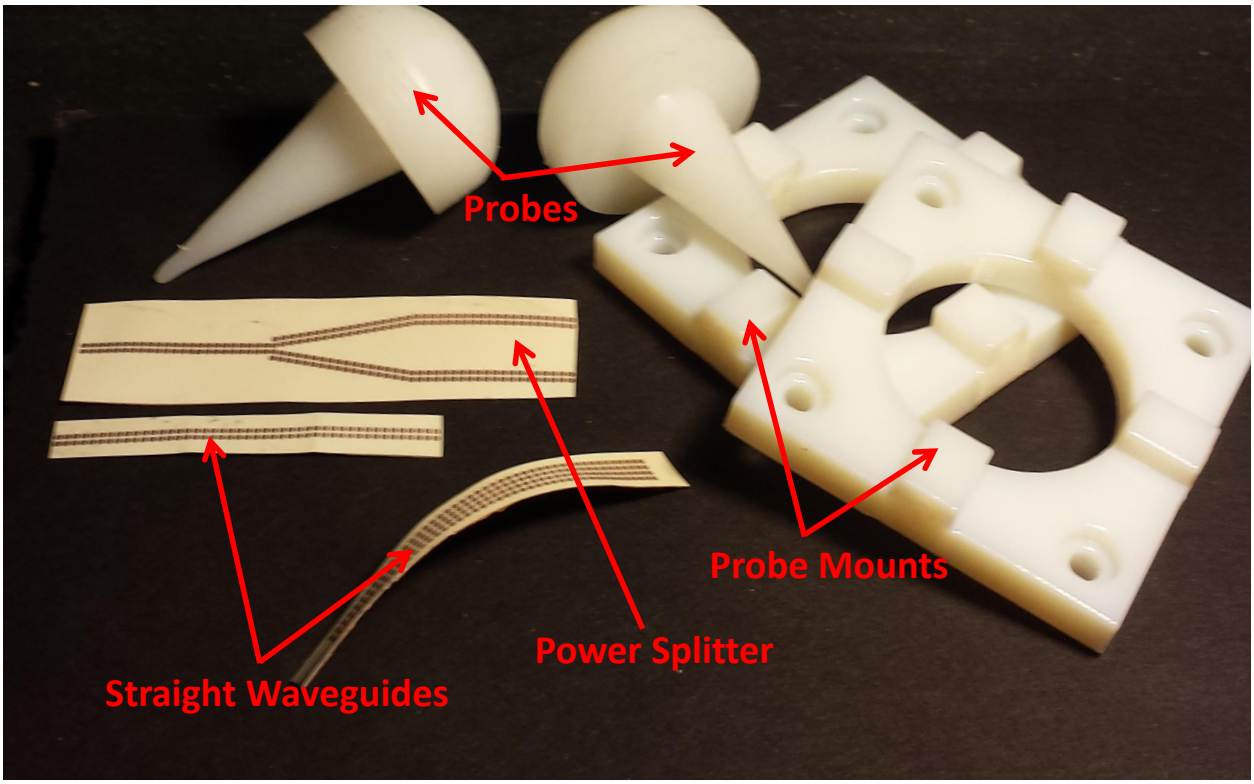

Figure 5.21 Fabricated waveguide, power splitter, and HDPE probes.

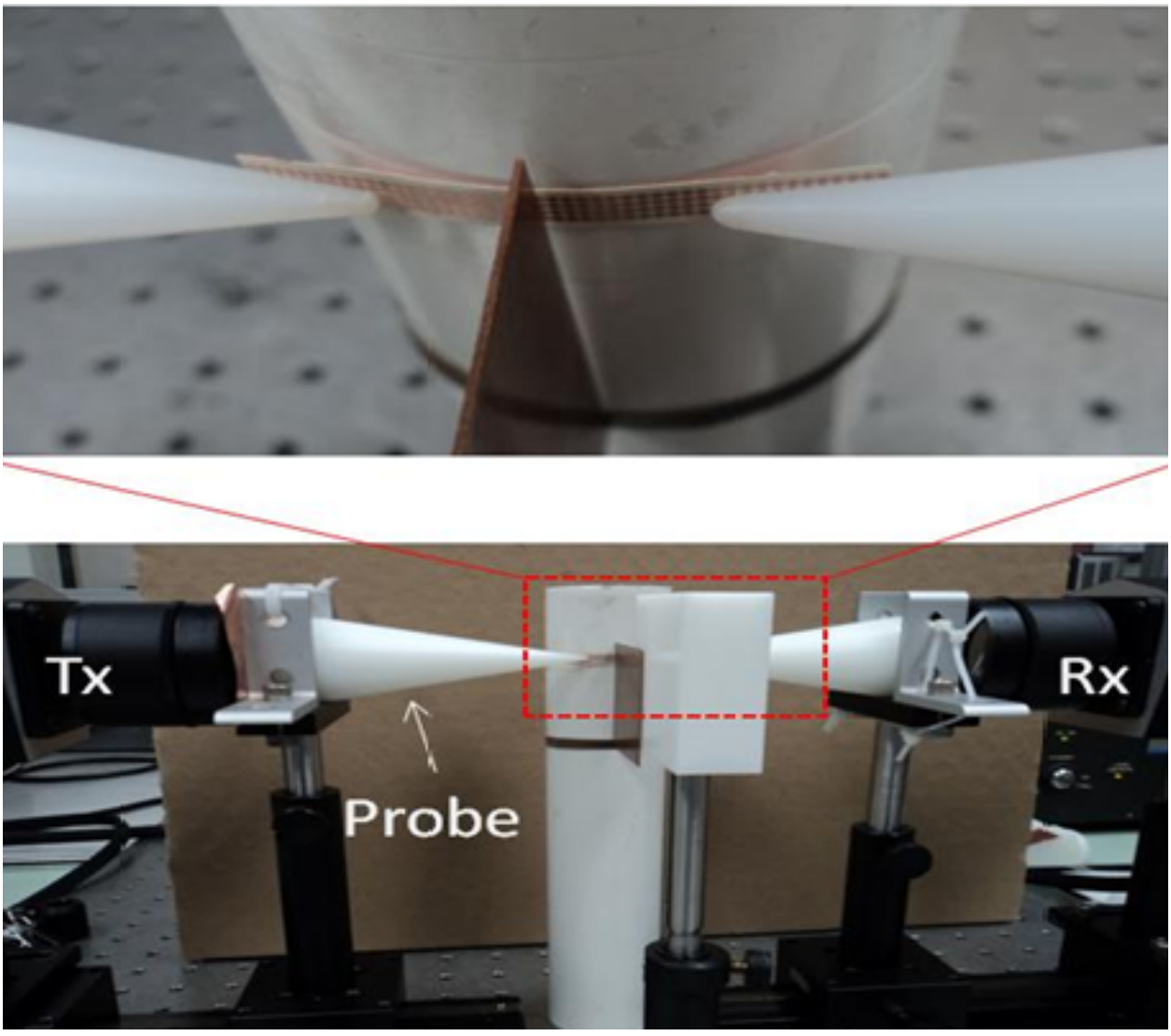

Figure 5.22 Waveguide measurement setup.

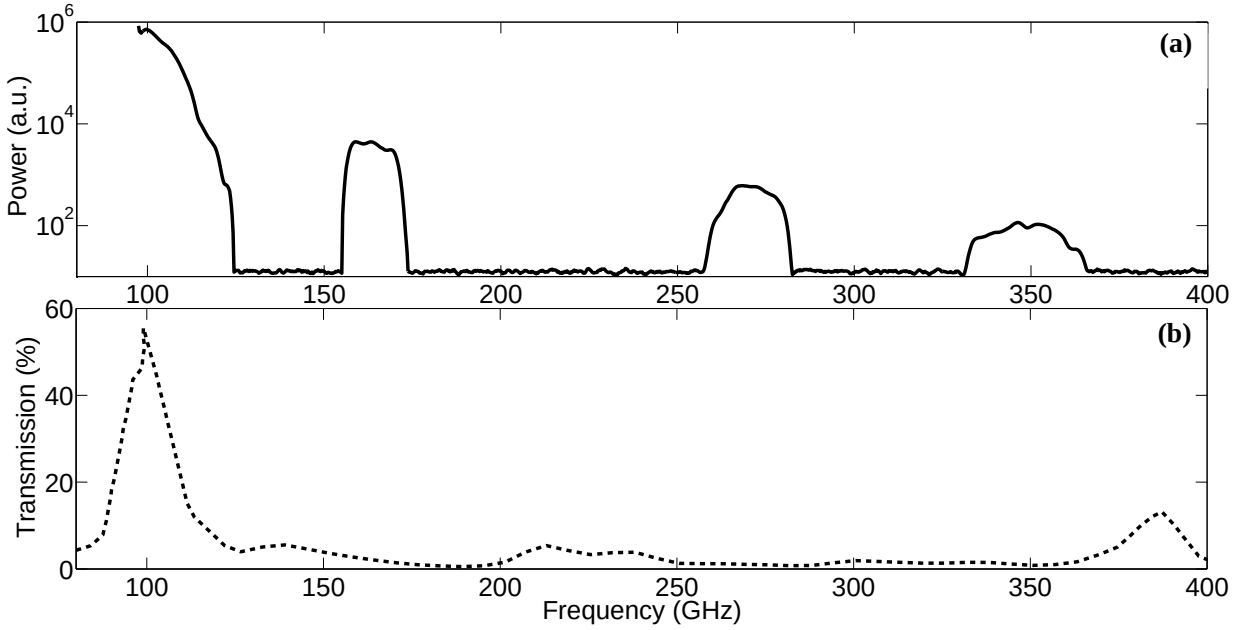

Figure 5.23 Measured transmission spectra for circle type waveguide with (a) frequency domain system, (b) time domain system.

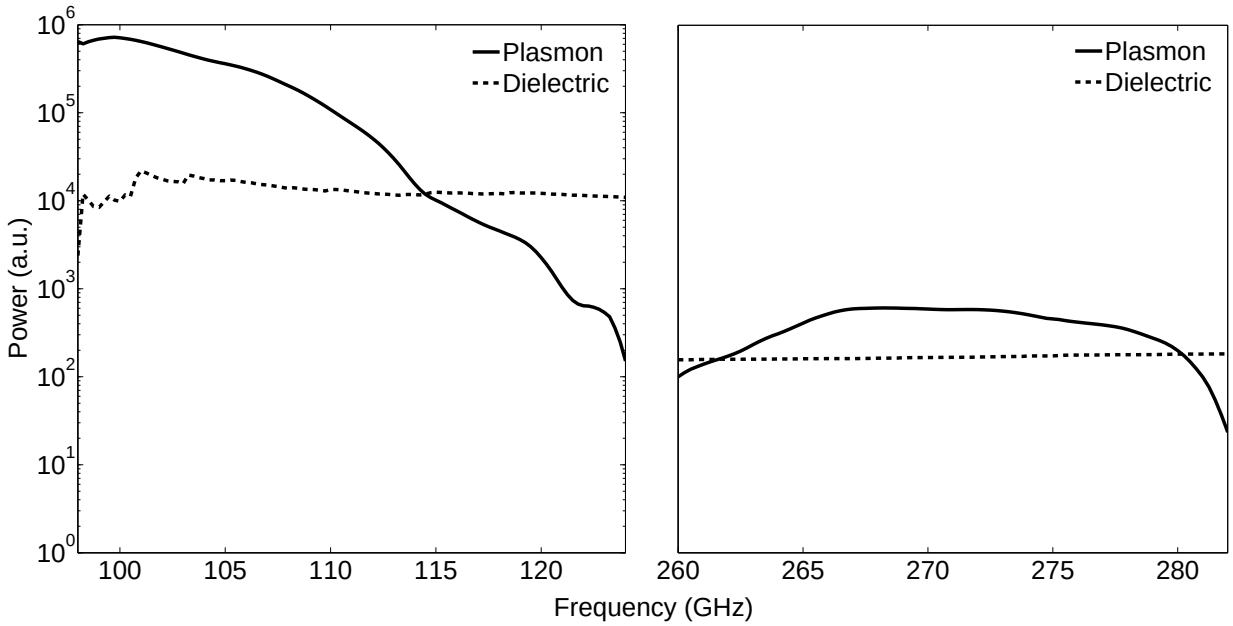

Figure 5.24 Measured transmission spectra for circle type waveguide compared with dielectric of same dimensions.

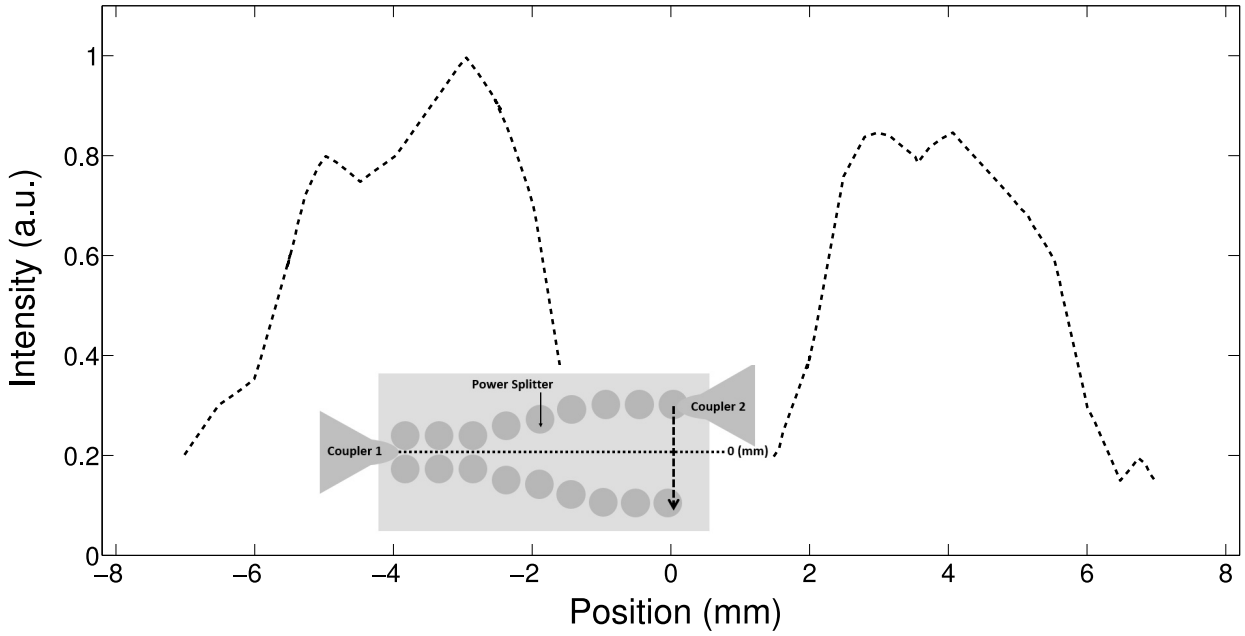

Figure 5.25 Transmission versus change in probe placement for the circle type power splitter at 100 GHz.

Figure 5.22.

Figure 5.23 shows the measured transmittance through the waveguide for both the time domain and frequency domain measurement. The transmission spectrum from the time domain measurement shows transmission peaks near 0.1, 0.22, and 0.38 THz. These resonance peaks are near the peaks expected for the circle structure. However, due to the resolution of the system and data averaging, some of the peaks are not present or shifted. In the case of the frequency domain measurement, four transmission peaks occur at approximately .1, .16, .26, and .35 THz. Only one half of the .1 THz peak is shown, as that is the minimum measurable frequency for the system. While the resonances do not match exactly as the predicted resonances, this discrepancy is believed to be caused by a few factors. The primary contributions are most likely due to misalignment between the probes and the waveguide, as well as the probe angle not being exactly transverse to the waveguide, similar to the change in resonance shown in Figure 5.10. Also, the initial resonances were simulated as infinitely periodic in both dimensions, while in reality this periodicity is finite. However, nearly 60 % of the power is transmitted through the waveguide at one of the possible resonance frequencies. Figure 5.24 shows the measured transmitted power over two frequency ranges corresponding to the strongest transmission peaks of the frequency domain measurement, compared with a dielectric strip made of the same dimensions as the thin-film waveguide. Clearly, a much larger transmission is detected over the frequency range where the resonant frequency of the top layer metal occurs.

The transmission properties of the power splitter are measured by fixing the probe position at the input to the power splitter, while varying the position of the second probe along both output branches. Here, the time domain system is used to measure the power splitter. The field intensity is measured at approximately 100 GHz, near the highest point of the transmission spectra. Figure 5.25 shows the measured field intensity as a function of position. Here, the zero position represents the middle point between the two branches. From the measured data, it is clearly shown that the wave propagates along the patterned

metal and is not concentrated in the dielectric.

5.8 Error Analysis and Discussion

In this chapter, the errors associated with the waveguide measurements are similar to that of chapter 3. Again, the most error occurs when the probes are not aligned well with the waveguide, but is again difficult to quantify. In the case of these waveguides, the incident angle also changes the frequency spectrum of the waveguides as shown in Figure 5.10, which compounds the error even further.

In the case of the THz systems used to measure the waveguides, the frequency-domain system suffers from the same issues discussed in Chapter 2. However, the time domain system also has its own errors associated with it. Primarily, this is caused by the small frequency resolution of approximately 12 GHz when the Fourier transform is used to convert the time-domain results into the frequency-domain. However, in comparison with other waveguide measurement techniques presented in the literature, the measured results presented here are well within a tolerable error.

5.9 Conclusions and Discussion

In this chapter, another approach to develop THz waveguide like devices is investigated. The design, fabricate, and measure THz planar plasmonic circuits based on thin metal resonant structures is presented. The resonance frequency at which the plasmonic-like mode can be launched can be predicted by simulating an infinite array of periodic structures. Each structure was then confirmed to display plasmonic like waveguiding by simulating both straight waveguides and a power splitter. These structures were created with simple clean room fabrication processes on a low-cost LCP flex substrate. A new approach to coupling the signal onto plasmonic structures with a dielectric focusing probe is also introduced. Measured results show that long range waveguiding can be achieved using planar plasmonic structures

at THz frequencies. Measurements of a straight waveguide and power splitter show strong field confinement along the length of the waveguide and along each branch of the power splitter, presenting the possibility for use in the design of novel THz planar circuits.

CHAPTER 6

Conclusions and Discussion

In this dissertation, efficient, integration compatible THz passive devices are developed. Three primary types of passive devices are considered: Thz waveguides, filters, and couplers.

The coupling of THz radiation between commercial THz systems and THz devices is realized with HDPE dielectric focusing probes. These probes are designed such that they can be excited via Tx and Rx heads available in commercial THz systems. The probes are studied with FEM modeling to determine the focal point and field confinement along a small section of the probe tip. The coupling characteristics of the probes when used in conjunction with a simple dielectric waveguide is studied, and the loss of the probes and coupling is presented.

Thin-film based filters are also introduced, which are integration compatible although still measured in a quasi-optical manner. The filter characteristics are optimized using a multi-objective genetic algorithm that is interfaced with the commercial FEM solver HFSS. Primarily, band-stop filters are investigated, and the bandwidth, rejection, and multi-band characteristics are optimized.

Two waveguide types are also introduced. First, a silicon based dielectric ridge waveguide which can be easily fabricated directly on-wafer is investigated. The transmission characteristics of the waveguide are studied first through a approximate 2-D theoretical so-

lution, and then through 3-D FEM modeling. The ridge waveguides show low attenuation especially when the ridge width and height is small, but a tradeoff between curvature and confinement properties with the height and width of the ridge is found. Secondly, a hybrid waveguide with built in filtering properties is introduced. The waveguides are inspired by traditional plasmonic waveguides, but created from thin-film type resonators. A theoretical floquet analysis is performed to ensure no higher order evanescent modes are coupled into. FEM analysis of the waveguide power confinement and field intensity is also performed to ensure a desired frequency response.

Both waveguides are then measured using commercial time and frequency-domain THz systems. In conjunction with the focusing probes introduced previously, the frequency response of both waveguide types is attained. Complex power-splitter measurements are also performed which show the potential for these waveguides to create other THz passive devices.

Overall, this dissertation introduces efficient, integration compatible THz passive devices. The realization of not only passive devices such as waveguides and filters, but also the introduction of a coupling method capable of bridging between the current quasi-optical systems with wafer-level integrated circuits provides a complete simulation to measurement correlation for the proposed THz devices. These results show promise for the future of integrated THz systems, and the improvement of current quasi-optical test systems.

BIBLIOGRAPHY

BIBLIOGRAPHY

[1] Siegel, Peter H. Terahertz technology. Microwave Theory and Tech- niques, IEEE Transactions on 50.3 (2002): 910-928.

[2] Shur, Michael. "Terahertz technology: devices and applications." Solid-State Circuits Conference, 2005. ESSCIRC 2005. Proceedings of the 31st European. IEEE, 2005.

[3] Tonouchi, Masayoshi. "Cutting-edge terahertz technology." Nature photonics 1.2 (2007): 97-105.

[4] Hosako, Iwao, et al. "At the dawn of a new era in terahertz technology." Proceedings of the IEEE 95.8 (2007): 1611-1623.

[5] Miles, Robert, Paul Harrison, and Didier Lippens. Terahertz sources and systems. Vol. 27. Springer Science Business Media, 2001.

[6] M. Hangyo, M. Tani, and T. Nagashima, Terahertz Time-Domain Spectroscopy of Solids: A Review, Intl. Jour. Of Infrared and Millimeter Waves, Vol. 26, No. 12, (2005), pp.1661-1690.

[7] Dexheimer, Susan L., ed. Terahertz spectroscopy: principles and applications. CRC press, 2007.

[8] OHara, John F., Withawat Withayachumnankul, and Ibraheem Al-Naib. "A review on thin-film sensing with terahertz waves." Journal of Infrared, Millimeter, and Terahertz Waves 33.3 (2012): 245-291.

[9] Siegel, Peter H. "Terahertz technology in biology and medicine." Microwave Symposium Digest, 2004 IEEE MTT-S International. Vol. 3. IEEE, 2004.

[10] Kleine-Ostmann, Thomas, and Tadao Nagatsuma. "A review on terahertz communications research." Journal of Infrared, Millimeter, and Terahertz Waves 32.2 (2011): 143-171.

[11] Wietzke, S., et al. "Terahertz imaging: a new non-destructive technique for the quality control of plastic weld joints." Journal of the European Optical Society-Rapid publications 2 (2007).

[12] Kemp, Michael C., et al. "Security applications of terahertz technology." AeroSense 2003. International Society for Optics and Photonics, 2003.

[13] Sun, Yiwen, et al. "A promising diagnostic method: Terahertz pulsed imaging and spectroscopy." World journal of radiology 3.3 (2011): 55.

[14] Kulesa, Craig. "Terahertz spectroscopy for astronomy: from comets to cosmology." Terahertz Science and Technology, IEEE Transactions on 1.1 (2011): 232-240.

[15] Markelz, A. G., A. Roitberg, and E. J. Heilweil. "Pulsed terahertz spectroscopy of DNA, bovine serum albumin and collagen between 0.1 and 2.0 THz." Chemical Physics Letters 320.1 (2000): 42-48.

[16] Ho, L., et al. "Analysis of sustained-release tablet film coats using terahertz pulsed imaging." Journal of Controlled release 119.3 (2007): 253-261.

[17] Strachan, Clare J., et al. "Using terahertz pulsed spectroscopy to study crystallinity of pharmaceutical materials." Chemical Physics Letters 390.1 (2004): 20-24.

[18] Zeitler, J. Axel, et al. "Temperature dependent terahertz pulsed spectroscopy of carbamazepine." Thermochimica Acta 436.1 (2005): 71-77.

[19] O'Hara, John F., et al. "Thin-film sensing with planar terahertz metamaterials: sensitivity and limitations." Optics Express 16.3 (2008): 1786-1795.

[20] Suen, Jonathan Y., et al. "Towards medical terahertz sensing of skin hydration." Stud. Health Technol. Inform 142 (2009): 364-368.

[21] Bennett, David B., et al. "Terahertz sensing in corneal tissues." Journal of biomedical optics 16.5 (2011): 057003-057003.

[22] Nagel, M., et al. "A functionalized THz sensor for marker-free DNA analysis." Physics in Medicine and Biology 48.22 (2003): 3625.

[23] Arnone, Don, Craig Ciesla, and Michael Pepper. "Terahertz imaging comes into view." Physics World 4 (2000): 35-40.

[24] Ashworth, Philip C., et al. "Terahertz pulsed spectroscopy of freshly excised human breast cancer." Optics express 17.15 (2009): 12444-12454.

[25] Woodward, Ruth M., et al. "Terahertz pulse imaging in reflection geometry of human skin cancer and skin tissue." Physics in medicine and biology 47.21 (2002): 3853.

[26] Crawley, David, et al. "Three-dimensional terahertz pulse imaging of dental tissue." Journal of Biomedical Optics 8.2 (2003): 303-307.

[27] Podzorov, Alexander, and Guilhem Gallot. "Low-loss polymers for terahertz applications." Applied optics 47.18 (2008): 3254-3257.

[28] Hejase, Jose, Edward J. Rothwell, and Premjeet Chahal. "A multiple angle method for THz time-domain material characterization." Terahertz Science and Technology, IEEE Transactions on 3.5 (2013): 656-665.

[29] Walther, M., et al. "Collective vibrational modes in biological molecules investigated by terahertz timedomain spectroscopy." Biopolymers 67.45 (2002): 310-313.

[30] Shen, Y. C., et al. "Detection and identification of explosives using terahertz pulsed spectroscopic imaging." Applied Physics Letters 86.24 (2005): 241116.

[31] Dickinson, Jason C., et al. "Terahertz imaging of subjects with concealed weapons." Proc. SPIE. Vol. 6212. 2006.

[32] Kawase, Kodo, et al. "Non-destructive terahertz imaging of illicit drugs using spectral fingerprints." Optics express 11.20 (2003): 2549-2554.

[33] Anastasi, Robert F., and Eric I. Madaras. "Terahertz NDE for metallic surface roughness evaluation." Nondestructive Evaulation for Health Monitoring and Diagnostics. International Society for Optics and Photonics, 2006.

[34] Anastasi, Robert F., and Eric I. Madaras. "Terahertz NDE for under paint corrosion detection and evaluation." Review of Progress in Quantitative Nondestructive Evaluation; Volume 25 A 25 (2006): 515-522.

[35] Yeh, Cavour, Fred Shimabukuro, and Peter H. Siegel. "Low-loss terahertz ribbon waveguides." Applied optics 44.28 (2005): 5937-5946.

[36] Deibel, Jason A., et al. "Enhanced coupling of terahertz radiation to cylindrical wire waveguides." Optics express 14.1 (2006): 279-290.

[37] Wang, Kanglin, and Daniel M. Mittleman. "Metal wires for terahertz wave guiding." Nature 432.7015 (2004): 376-379.

[38] Miyagi, Mitsunobu, and Shojiro Kawakami. "Design theory of dielectric-coated circular metallic waveguides for infrared transmission." Lightwave Technology, Journal of 2.2 (1984): 116-126.

[39] Mitrofanov, Oleg, and James A. Harrington. "Dielectric-lined cylindrical metallic THz waveguides: mode structure and dispersion." Opt. Express 18.3 (2010): 1898-1903.

[40] Zhao, Yuguang, and D. Grischkowsky. "Terahertz demonstrations of effectively two-dimensional photonic bandgap structures." Optics letters 31.10 (2006): 1534-1536.

[41] Bingham, A. L., and D. Grischkowsky. "High Q, one-dimensional terahertz photonic waveguides." Applied Physics Letters 90.9 (2007): 91105-91105.

[42] Bingham, Adam, Yuguang Zhao, and D. Grischkowsky. "THz parallel plate photonic waveguides." Applied Physics Letters 87.5 (2005): 051101-051101.

[43] Bingham, Adam L., and Daniel R. Grischkowsky. "Terahertz 2-D photonic crystal waveguides." Microwave and Wireless Components Letters, IEEE 18.7 (2008): 428-430.

[44] Llombart, Nuria, et al. "Design of a low loss metallo-dielectric EBG waveguide at submillimeter wavelengths." Microwave and Wireless Components Letters, IEEE 19.7 (2009): 437-439.

[45] Wu, Ziran, et al. "Hollow-core electromagnetic band gap (EBG) waveguide fabricated by rapid prototyping for low-loss Terahertz guiding." Microwave Symposium Digest (MTT), 2010 IEEE MTT-S International. IEEE, 2010.

[46] Gallot, G., et al. "Terahertz waveguides." JOSA B 17.5 (2000): 851-863.

[47] Ghaemi, H. F., et al. "Surface plasmons enhance optical transmission through subwavelength holes." Physical Review B 58.11 (1998): 6779.

[48] Brongersma, Mark L., and Pieter G. Kik. Surface plasmon nanophotonics. Vol. 131. Berlin: Springer, 2007.

[49] Yeh, Cavour, Fred Shimabukuro, and Peter H. Siegel. Low-loss terahertz ribbon waveguides. Applied optics 44.28 (2005): 5937-5946.

[50] Yang, Xianbo, and Premjeet Prem Chahal. "On-Wafer Terahertz Ribbon Waveguides Using PolymerCeramic Nanocomposites." Components, Packaging and Manufacturing Technology, IEEE Transactions on 5.2 (2015): 245-255.

[51] Ranjkesh, Nazy, et al. "Silicon-on-glass dielectric waveguidePart I: For millimeter-wave integrated circuits." Terahertz Science and Technology, IEEE Transactions on 5.2 (2015): 268-279.

[52] Ranjkesh, Nazy, et al. "Silicon-on-Glass Dielectric WaveguidePart II: For THz Applications." Terahertz Science and Technology, IEEE Transactions on 5.2 (2015): 280-287.

[53] Ma, Y. G., et al. "Experimental demonstration of subwavelength domino plasmon devices for compact high-frequency circuit." Optics Express 19.22 (2011): 21189-21198.

[54] Ghamsari, Behnood G., and A. Hamed Majedi. "Terahertz transmission lines based on surface waves in plasmonic waveguides." Journal of Applied Physics 104.8 (2008): 083108-083108.

[55] Williams, Christopher R., et al. "Highly confined guiding of terahertz surface plasmon polaritons on structured metal surfaces." Nature Photonics 2.3 (2008): 175-179.

[56] Zhu, Wenqi, Amit Agrawal, and Ajay Nahata. "Planar plasmonic terahertz guided-wave devices." Optics express 16.9 (2008): 6216-6226.

[57] Sambles, J. R., G. W. Bradbery, and Fuzi Yang. "Optical excitation of surface plasmons: an introduction." Contemporary physics 32.3 (1991): 173-183.

[58] Rusina, Anastasia, Maxim Durach, and Mark I. Stockman. "Theory of spoof plasmons in real metals." SPIE NanoScience+ Engineering. International Society for Optics and Photonics, 2010.

[59] Zhu, Wenqi, et al. "Engineering the propagation properties of planar plasmonic terahertz waveguides." Selected Topics in Quantum Electronics, IEEE Journal of 17.1 (2011): 146-153.

[60] Pendry, J. B., L. Martin-Moreno, and F. J. Garcia-Vidal. "Mimicking surface plasmons with structured surfaces." Science 305.5685 (2004): 847-848.

[61] Chahal, Premjeet, et al. "Planar surface plasmonic structures for terahertz circuits and sensors." Electronic Components and Technology Conference (ECTC), 2012 IEEE 62nd. IEEE, 2012.

[62] W. Zhu, A. Agrawal, and A. Nahata, Planar plasmonic terahertz guidedwave devices, Optics express 16, 62166226 (2008).

[63] X. Liu, Y. Feng, K. Chen, B. Zhu, J. Zhao, and T. Jiang, Planar surface plasmonic waveguide devices based on symmetric corrugated thin film structures, Optics express 22, 2010720116 (2014).

[64] X. Shen, T. J. Cui, D. Martin-Cano, and F. J. Garcia-Vidal, Conformal surface plasmons propagating on ultrathin and flexible films, Proceedings of the National Academy of Sciences 110, 4045 (2013)

[65] Macleod, H. Angus. Thin-film optical filters. CRC Press, 2010.

[66] Crystals, Photonic. "Molding the flow of Light." Princeton University (2008).

[67] Acosta Silveira, Laura Cecilia. Terahertz Photonic Crystal Microfluidic Sensors., 2014.

[68] Guo, Shen Hui, et al. "Terahertz filter based on a composite metal-dielectric-metal structure." Applied Superconductivity and Electromagnetic Devices (ASEMD), 2013 IEEE International Conference on. IEEE, 2013.

[69] Xu, JiaMing, et al. "Triple-channel terahertz filter based on mode coupling of cavities resonance system." Applied Physics Letters 103.16 (2013): 161116.

[70] Lee, J., et al. "Shape resonance omni-directional terahertz filters with near-unity transmittance." Optics express 14.3 (2006): 1253-1259.

[71] Tuniz, A., et al. "Drawn metamaterials with plasmonic response at terahertz frequencies." Applied Physics Letters 96.19 (2010): 191101.

[72] Tao, Jin, et al. "Tunable subwavelength terahertz plasmonic stub waveguide filters." Nanotechnology, IEEE Transactions on 12.6 (2013): 1191-1197.

[73] D. Wu, N. Fang, C. Sun, X. Zhang, W. J. Padilla, D. N. Basov, D. R. Smith, and S. Schultz, Terahertz plasmonic high pass filter, Applied Physics Letters, vol. 83, no. 2003, pp. 201203, 2003.

[74] M. a. Kaliteevski, S. Brand, J. Garvi -Cook, R. a. Abram, and J. M. Chamberlain, Terahertz filter based on refractive properties of metallic photonic crystal., Optics express, vol. 16, no. 10, pp. 73307335, 2008.

[75] L. Rao, D. Yang, L. Zhang, T. Li, and S. Xia, Design and experimental verification of terahertz wideband filter based on double-layered metal hole arrays, Applied Optics, vol. 51, p. 912, 2012.

[76] P. Chahal, J. Myers, K. Y. Park, C. Meierbachtol, and N. Nair, Planar surface plasmonic structures for terahertz circuits and sensors, in Proceedings -Electronic Components and Technology Conference, pp. 930935, 2012.

[77] A. Kaur, X. Yang, and P. Chahal, Study of Microwave Circuits Based on Metal-Insulator-Metal (MIM) Diodes on Flex Substrates, no. Mim, pp. 21682174, 2014.

[78] M. Z. Lu, W. Z. Li, and E. R. Brown, Second order bandpass terahertz filter achieved by multilayer com- plementary metamaterial structures, Optics Letters, vol. 36, pp. 10711073, 2011.

[79] Chen, Chao-Yuan, et al. "Liquid-crystal-based terahertz tunable Lyot filter." Applied physics letters 88.10 (2006).

[80] Mendis, Rajind, et al. "A tunable universal terahertz filter using artificial dielectrics based on parallel-plate waveguides." Applied physics letters 97.13 (2010): 131106.

[81] Libon, I. H, et al. "An optically controllable terahertz filter." Applied Physics Letters 76.20 (2000): 2821-2823.

[82] Nemec, H., et al. "Thermally tunable filter for terahertz range based on a one-dimensional photonic crystal with a defect." Journal of applied physics 96.8 (2004): 4072-4075.

[83] Salokatve, A., et al. "Continuous-wave, room temperature, ridge waveguide green-blue diode laser." Electronics Letters 29.25 (1993): 2192-2194. APA

[84] Tucker, Rodney S., and Ivan P. Kaminow. "High-frequency characteristics of directly modulated InGaAsP ridge waveguide and buried heterostructure lasers." Lightwave Technology, Journal of 2.4 (1984): 385-393.

[85] Kaminow, I. P., et al. "Lithium niobate ridge waveguide modulator." Applied Physics Letters 24.12 (1974): 622-624.

[86] Kawachi, Masao. "Silica waveguides on silicon and their application to integrated-optic components." Optical and Quantum Electronics 22.5 (1990): 391-416.

[87] Williams, Benjamin, et al. "Operation of terahertz quantum-cascade lasers at 164 K in pulsed mode and at 117 K in continuous-wave mode." Optics Express 13.9 (2005): 3331-3339.

[88] Kohen, Stephen, Benjamin S. Williams, and Qing Hu. "Electromagnetic modeling of terahertz quantum cascade laser waveguides and resonators." Journal of applied physics 97.5 (2005): 053106.

[89] Kumar, Sushil, et al. "Surface-emitting distributed feedback terahertz quantum-cascade lasers in metal-metal waveguides." Optics Express 15.1 (2007): 113-128.

[90] Goell, J. E. "A circularharmonic computer analysis of rectangular dielectric waveguides." Bell System Technical Journal 48.7 (1969): 2133-2160.

[91] Marcatili, Enrique AJ. "Dielectric rectangular waveguide and directional coupler for integrated optics." Bell System Technical Journal 48.7 (1969): 2071-2102.

[92] Myers, Joshua C., et al. "Investigation of modulation-capable silicon waveguides for efficient on-wafer terahertz interconnects." Electronic Components and Technology Conference (ECTC), 2015 IEEE 65th. IEEE, 2015.

[93] Hejase, Jose Ale. Terahertz Time Domain Methods for Material Characterization of Layered Dielectric Media., 2012.

[94] Haupt, Randy L., and Sue Ellen Haupt. Practical genetic algorithms. John Wiley Sons, 2004.

[95] Goldberg, David Edward. Genetic algorithms in search, optimization, and machine learning. Vol. 412. Reading Menlo Park: Addison-wesley, 1989.

[96] Johnson, J. Michael, and V. Rahmat-Samii. "Genetic algorithms in engineering electromagnetics." Antennas and Propagation Magazine, IEEE 39.4 (1997): 7-21.

[97] J. Schaffer and J. Grefenstette, Multi-Objective Learning via Genetic Algorithms., Ijcai, pp. 13, 1985.

[98] E. Zitzler, M. Laumanns, and L. Thiele, SPEA2: Improving the Strength Pareto Evolutionary Algorithm, Evolutionary Methods for Design Optimization and Control with Applications to Industrial Problems, pp. 95100, 2001.

[99] T. Murata and H. Ishibuchi, MOGA: multi-objective genetic algorithms, Evolutionary Computation,1995., IEEE International Conference on, vol. 1, p. 289, 1995.

[100] K. Deb, A. Pratap, S. Agarwal, and T. Meyarivan, A fast and elitist multiobjective genetic algorithm: NSGA-II, IEEE Transactions on Evolutionary Computation, vol. 6, no. 2, pp. 182197, 2002.

[101] K. Deb, Multi-objective optimization using evolutionary algorithms, vol. 16. John Wiley Sons, 2001.

[102] E. Michielssen, J. Sajer, S. Ranjithan, and R. Mittra, Design of Lightweight, Broad-Band Microwave Absorbers Using Genetic Algorithms, IEEE Transactions on Microwave Theory and Techniques, MTT-41,6/7, June/July 1993, pp. 1024-1031.

[103] Michielssen, Eric, J. M. Sajer, and Raj Mittra. "Design of multilayered FSS and waveguide filters using genetic algorithms." Antennas and Propagation Society International Symposium, 1993. AP-S. Digest. IEEE, 1993.

[104] Haupt, Randy L. "Thinned arrays using genetic algorithms." Antennas and Propagation, IEEE Transactions on 42.7 (1994): 993-999.

[105] Johnson, J. Michael, and Yahya Rahmat-Samii. "Genetic algorithm optimization and its application to antenna design." Antennas and Propagation Society International Symposium, 1994. AP-S. Digest. Vol. 1. IEEE, 1994.

[106] Johnson, J. Michael, and Yahya Rahmat-Samii. "Genetic algorithms and method of moments (GA/MOM) for the design of integrated antennas." Antennas and Propagation, IEEE Transactions on 47.10 (1999): 1606-1614.

[107] Ouedraogo, R.O.; Rothwell, E.J.; Diaz, A.; Shih-Yuan Chen; Temme, A.; Fuchi, K., "In Situ Optimization of Metamaterial-Inspired Loop Antennas", Antennas and Wireless Propagation Letters, IEEE , vol.9, no., pp.75,78, 2010

[108] R. O. Ouedraogo and E. J. Rothwell, Metamaterial inspired patch antenna miniaturization technique, IEEE International Symposium on Antennas and Propagation and URSI Radio Science Meeting Digest, pp. 1-4, 2010.

[109] R. O. Ouedraogo, E. J. Rothwell, A. R. Diaz, K. Fuchi, and A. Temme, Miniaturization of patch antennas using a metamaterial-inspired technique, IEEE Antennas Wireless Propag. Lett., vol. 9, pp. 75-78, 2010.

[110] R. O. Ouedraogo, E. J. Rothwell, Prem Chahal, A. R. Diaz, and K. Fuchi Design and Optimization of Metamaterial Inspired On-chip Antennas for Wireless Applications. Presented at 2011 IEEE AP-S/URSI conference.

[111] K. Deb. Multi-objective genetic algorithms: Problem difficulties and construction of test problems. Evolutionary Computation Journal, 7(3):205230, 1999.

[112] C. M. Fonesca and P. J. Fleming. On the performance assessment and comparison of stochastic multiobjective optimizers. In Proceedings of Parallel Problem Solving from Nature IV (PPSN-IV), pages 584593, 1996

[113] K. Deb. Multi-objective optimization using evolutionary algorithms. Chichester, UK: Wiley, 2001.

[114] Deb, Kalyanmoy, Ankur Sinha, and Saku Kukkonen. "Multi-objective test problems, linkages, and evolutionary methodologies." Proceedings of the 8th annual conference on Genetic and evolutionary computation. ACM, 2006.

[115] Zitzler, Eckart, Kalyanmoy Deb, and Lothar Thiele. "Comparison of multiobjective evolutionary algorithms: Empirical results." Evolutionary computation 8.2 (2000): 173-195.

[116] Petersson, LE Rickard, and Jian-Ming Jin. "A three-dimensional time-domain finite-element formulation for periodic structures." Antennas and Propagation, IEEE Transactions on 54.1 (2006): 12-19.

[117] Hejase, Jose, Pavel R. Paladhi, and Premjeet Prem Chahal. "Terahertz characterization of dielectric substrates for component design and nondestructive evaluation of packages." Components, Packaging and Manufacturing Technology, IEEE Transactions on 1.11 (2011): 1685-1694.